

**Solid-State NMR Characterisation of  
Transition-Metal Bearing Nuclear Waste Glasses**

by

Brandon James Greer

A Thesis submitted to the Faculty of Graduate Studies of  
The University of Manitoba  
in partial fulfilment of the requirements of the degree of

Master of Science

Department of Chemistry  
University of Manitoba  
Winnipeg, MB, Canada

# Abstract

Alkali borosilicate glass is used to immobilise high-level radioactive waste generated from the reprocessing of spent nuclear fuel. However, poorly soluble waste products such as molybdenum present issues for long-term storage of the material, whereby phase separation of water-soluble crystalline aggregates truncate the glass network and offer leaching opportunities for the escape of radionuclides into the environment. Solid-state NMR is an effective technique for studying the phase separation in nuclear waste glasses, as it is able to distinguish glassy and crystalline environments using nuclei-specific probes. The presence of paramagnetic transition metal cations within the waste glass compromises the efficacy of NMR, as unpaired electrons can cause broadening and chemical shift effects. This work engages in a multinuclear magnetic resonance characterisation of paramagnetically-doped (by  $\text{Cr}_2\text{O}_3$ ,  $\text{MnO}_2$ ,  $\text{Fe}_2\text{O}_3$ ,  $\text{NiO}$ , or  $\text{Nd}_2\text{O}_3$ ) model nuclear waste glasses and explores the partitioning of transition-metal components. Characterisation of the separated heterogeneous crystalline phase was accomplished principally by  $^{133}\text{Cs}$ ,  $^{23}\text{Na}$ , and  $^{95}\text{Mo}$  NMR, where it was determined that Cr substitutes into mixed-alkali molybdates. Furthermore, paramagnetic broadening and relaxation effects were observed and quantified by  $^{11}\text{B}$  and  $^{29}\text{Si}$  NMR.

# Acknowledgements

The completion of this work was made possible with the continual support and assistance of many individuals. First and foremost, I am grateful for the guidance provided by my supervisor Dr. Scott Kroeker, whose keen attention to detail and thorough evaluations of research milestones have provided a tangible evolution of my research and communication abilities throughout the course of this program. I extend special thanks to former-group-member Dr. Vladimir Michaelis, who taught me the essentials of nuclear magnetic resonance experimentation and provided extensive guidance on how to conduct and present research. I would also like to thank fellow graduate student John Wren for technical assistance and many useful discussions of NMR theory. I thank the undergraduate members of the group (current and former) for their great company in the lab: Heather Cavers, Kimberley Craigen, Stan Giesbrecht, Carolyn Higman, Palak Kachhadia, Kirill Levin, Lawson Miller, Alex Paterson, and Rhys Sharkey.

I would like to acknowledge the internal and external members of my examining committee, Dr. Georg Schreckenbach (Dept. of Chemistry) and Dr. Doug Buchanan (Dept. of Electrical and Computer Engineering), for their evaluations of this thesis.

Finally, I would like to recognise all others who have contributed to my research and/or personal experiences during my time at the University of Manitoba: Dr. Mario Bieringer (XRD, Dept. of Chemistry), Dr. Peter Budzelaar, Dr. Horace Luong, Dr. Ravinder Sidhu (EMPA, Dept. of Geology), Dr. Elena Smirnova, Dr. Gro Thorne-Tjomsland, Dr. James Xidos, Dr. Panseak Yang (LA-ICP-MS, Dept. of Geology), NMR staff (Dr. Kirk Marat and Terry Wolowiec), departmental office staff (Tricia Lewis, Sharon Mullen, and Keith Travis), and family & friends (you know who you are!). The University of Manitoba is also acknowledged for a Faculty of Science Graduate Scholarship, yearly graduate awards, and travel assistance.

# Table of Contents

<b>Abstract</b>	i
<b>Acknowledgements</b>	ii
<b>List of Tables</b>	vii
<b>List of Figures</b>	viii
 <b>Chapter 1: Disposal of Nuclear Waste</b>	
1.1 The Nuclear Fuel Cycle	1
1.2 Immobilisation of High-Level Nuclear Waste	4
1.3 Phase Separation in HLW Glass	5
1.4 Experimental Techniques for Studying HLW Glasses	6
 <b>Chapter 2: Chemical Description of Glasses</b>	
2.1 Thermodynamics of Glass Formation	9
2.2 Classification of the Glass Network	
2.2.1 Network Formers	11
2.2.2 Network Modifiers	12
2.2.3 Intermediate Formers	12
2.3 Waste Glass Compositions	12
 <b>Chapter 3: Solid-State NMR Spectroscopy</b>	
3.1 Nuclear Magnetic Resonance Theory	16

3.2 Isotopic Properties	17
3.2.1 Natural Abundance	20
3.2.2 Resonance Frequency	20
3.2.3 Spin Number	21
3.3 NMR of Solids	
3.3.1 Chemical Shift Anisotropy	21
3.3.2 The Quadrupolar Interaction	23
3.3.3 Spin-Spin Coupling	25
3.3.4 Dipolar Coupling	25
3.3.5 The Paramagnetic Interaction	27
3.4 Magic-Angle Spinning	28
 <b>Chapter 4: NMR Nuclides of Model HLW Glass</b>	
4.1 Cesium-133 NMR	31
4.2 Sodium-23 NMR	32
4.3 Molybdenum-95 NMR	33
4.4 Boron-11 NMR	34
4.5 Silicon-29 NMR	34
 <b>Chapter 5: Addition of Transition Metals to Model HLW Glass</b>	
5.1 Glass Series Design	36
5.2 Experimental	
5.2.1 Glass Synthesis	37
5.2.2 Nuclear Magnetic Resonance Spectroscopy	40

5.3 Results and Discussion	
5.3.1 $^{133}\text{Cs}$ MAS NMR . . . . .	41
5.3.2 $^{23}\text{Na}$ MAS NMR . . . . .	46
5.3.3 $^{11}\text{B}$ MAS NMR . . . . .	50
5.3.4 NMR of a Complex Model HLW Glass . . . . .	56
5.4 Summary . . . . .	59
 <b>Chapter 6: Chromium-Bearing Model HLW Glasses</b>	
6.1 Chromium in HLW Glasses . . . . .	60
6.2 Experimental	
6.2.1 Glass Synthesis . . . . .	61
6.2.2 Elemental Analysis . . . . .	63
6.2.3 Nuclear Magnetic Resonance Spectroscopy . . . . .	64
6.3 Results and Discussion . . . . .	65
6.3.1 Compositional Analyses of the Bulk Material . . . . .	66
6.3.2 NMR of the Bulk Material . . . . .	69
6.3.3 NMR of the Model Yellow Phase . . . . .	85
6.3.4 Compositional Analyses of the Model Yellow Phases . . . . .	102
6.4 Summary . . . . .	109
 <b>Chapter 7: Iron-Bearing Model HLW Glasses</b>	
7.1 Iron in HLW Glasses . . . . .	111
7.2 Experimental	
7.2.1 Glass Synthesis . . . . .	112

7.2.2 Electron Microprobe Analysis . . . . .	112
7.2.3 Nuclear Magnetic Resonance Spectroscopy . . . . .	114
7.3 Results and Discussion . . . . .	114
7.3.1 Compositional Analyses of the Bulk Material . . . . .	115
7.3.2 NMR of the Bulk Material . . . . .	115
7.3.3 NMR of the Crystalline Phase . . . . .	126
7.4 Summary . . . . .	131
 <b>Chapter 8: Conclusions and Future Outlook</b>	
8.1 Identification and Quantification of Crystalline Components . . . . .	133
8.2 Paramagnetic Effect of Transition Metal Oxides	
8.2.1 NMR of Network Modifiers . . . . .	135
8.2.2 NMR of Network Formers . . . . .	136
8.3 Chromium as a Phase-Separation Product . . . . .	137
8.4 Hydration of Cesium-Sodium Molybdate . . . . .	138
8.5 Future Studies of Model HLW Glasses	
8.5.1 Glass Series of Individual Paramagnetic Additives . . . . .	139
8.5.2 Glass Series of Multiple Paramagnetic Additives . . . . .	139
8.5.3 Compositional Complexity in Model HLW Glasses . . . . .	140
 <b>Appendix: Binomial Distribution Models . . . . .</b>	 141
 <b>References . . . . .</b>	 143

# List of Tables

<b>1.1.</b> Selected HLW compositions . . . . .	3
<b>2.1.</b> Composition of the reference HLW glass SON68 . . . . .	15
<b>5.1.</b> Target compositions of six-component glasses . . . . .	38
<b>5.2.</b> Batch (‘weighed’) compositions of six-component glasses . . . . .	38
<b>5.3.</b> Target and batch (‘weighed’) compositions of glass <b>9</b> (all additives) . . . . .	39
<b>5.4.</b> Integrated intensities for $^{133}\text{Cs}$ MAS NMR of glasses <b>1-8</b> . . . . .	45
<b>5.5.</b> $^{23}\text{Na}$ MAS NMR parameters of relevant sodium-bearing compounds . . . . .	49
<b>5.6.</b> Integrated intensities for $^{23}\text{Na}$ MAS NMR of selected glasses . . . . .	49
<b>5.7.</b> FWHM values and integrated intensities for $^{11}\text{B}$ MAS NMR of glasses <b>1-8</b> . . . . .	54
<b>6.1.</b> Compositions of chromium series glasses . . . . .	62
<b>6.2.</b> Integrated intensities for $^{133}\text{Cs}$ MAS NMR of Cr series glasses . . . . .	71
<b>6.3.</b> Integrated intensities of unknown $^{133}\text{Cs}$ MAS NMR sites of Cr-5 and Cr-6 glasses . . . . .	71
<b>6.4.</b> Integrated intensities for $^{23}\text{Na}$ MAS NMR of Cr series glasses . . . . .	74
<b>6.5.</b> $^{95}\text{Mo}$ NMR parameters of relevant molybdenum-bearing compounds . . . . .	77
<b>6.6.</b> Integrated intensities for $^{133}\text{Cs}$ MAS NMR of model <i>yellow phase</i> samples . . . . .	87
<b>6.7.</b> Relative intensities for $^{133}\text{Cs}$ MAS NMR of the $\text{Cs}_3\text{Na}(\text{Mo}_{1-x}\text{Cr}_x\text{O}_4)_2$ sites . . . . .	91
<b>6.8.</b> Integrated intensities for $^{23}\text{Na}$ MAS NMR of model <i>yellow phase</i> samples . . . . .	99
<b>6.9.</b> Compositional determination of YP4 by EMPA . . . . .	104
<b>6.10.</b> Example of YP4 “composition by difference” from parent glass Cr-4 . . . . .	105
<b>6.11.</b> Compositional determinations of model <i>yellow phase</i> samples . . . . .	107
<b>6.12.</b> Quantification of phase separation and volatilisation in Cr-4 glass . . . . .	108
<b>7.1.</b> Compositions of iron series samples . . . . .	113
<b>7.2.</b> Integrated intensities for $^{133}\text{Cs}$ MAS NMR of Fe series glasses . . . . .	117
<b>7.3.</b> Integrated intensities for $^{23}\text{Na}$ MAS NMR of Fe series glasses . . . . .	121



# List of Figures

<b>2.1.</b>	Thermodynamic plot of glass and crystal formation	10
<b>2.2.</b>	Two-dimensional representation of a glass network	13
<b>3.1.</b>	Relationship between Zeeman splitting and magnetic field strength	18
<b>3.2.</b>	Spin description of an NMR experiment	19
<b>3.3.</b>	Energy level diagram and NMR spectrum of a quadrupolar nucleus	22
<b>3.4.</b>	Chemical shift anisotropy in solid-state NMR	24
<b>3.5.</b>	Effect of the quadrupolar asymmetry parameter on the NMR central transition	26
<b>3.6.</b>	Description of Magic-Angle Spinning	29
<b>5.1.</b>	$^{133}\text{Cs}$ MAS NMR spectrum of the five-component base glass	42
<b>5.2.</b>	$^{133}\text{Cs}$ MAS NMR spectra of glasses <b>1-8</b>	44
<b>5.3.</b>	$^{23}\text{Na}$ MAS NMR spectrum of the five-component base glass	47
<b>5.4.</b>	$^{23}\text{Na}$ MAS NMR spectra of selected paramagnetic glasses	48
<b>5.5.</b>	$^{11}\text{B}$ MAS NMR spectrum of the five-component base glass	52
<b>5.6.</b>	$^{11}\text{B}$ MAS NMR spectra of glasses <b>1-8</b>	53
<b>5.7.</b>	$^{13}\text{B}$ and $^{14}\text{B}$ FWHM values as a function of glass paramagnetic content	55
<b>5.8.</b>	$^{133}\text{Cs}$ MAS NMR spectra of glass <b>9</b> (all paramagnetic additives)	57
<b>5.9.</b>	$^{23}\text{Na}$ MAS NMR spectrum of glass <b>9</b> (all paramagnetic additives)	58
<b>5.10.</b>	$^{11}\text{B}$ MAS NMR spectrum of glass <b>9</b> (all paramagnetic additives)	58
<b>6.1.</b>	LA-ICP-MS line profile of a phase-separated Cr-containing glass	68
<b>6.2.</b>	$^{133}\text{Cs}$ MAS NMR spectra of chromium series glasses	70
<b>6.3.</b>	$^{23}\text{Na}$ MAS NMR spectra of chromium series glasses	73
<b>6.4.</b>	$^{23}\text{Na}$ MAS NMR spectrum of glass Cr-6.	75

6.5. $^{95}\text{Mo}$ MAS NMR spectra of glass Cr-2 at 14.1 and 21.1 T	76
6.6. $^{11}\text{B}$ MAS NMR spectra of chromium series glasses	79
6.7. $^{[3]}\text{B}$ and $^{[4]}\text{B}$ FWHM values as a function of glass $\text{Cr}^{3+}$ content	80
6.8. <i>Saturation Recovery</i> pulse sequence	82
6.9. $^{29}\text{Si}$ MAS NMR spectra and $T_1$ measurement of the five-component base glass	83
6.10. $^{29}\text{Si}$ MAS NMR spectra and $T_1$ measurement of selected Cr glasses	84
6.11. $^{133}\text{Cs}$ MAS NMR spectra of Cr-containing model <i>yellow phase</i> samples	86
6.12. Theoretical three- and four-cation models for $\text{Cs}_3\text{Na}(\text{Mo}_{1-x}\text{Cr}_x\text{O}_4)_2$	89
6.13. Interpretation of experimental $^{133}\text{Cs}$ MAS NMR signals for $\text{Cs}_3\text{Na}(\text{Mo}_{1-x}\text{Cr}_x\text{O}_4)_2$	90
6.14. $^{133}\text{Cs}$ MAS NMR spectra of YP3 and YP4 at 14.1 T and 21.1 T	93
6.15. $^{23}\text{Na}$ MAS NMR spectra of Cr-containing model <i>yellow phase</i> samples	96
6.16. $^{23}\text{Na}$ MAS NMR spectra of YP3 and YP4 at 14.1 T and 21.1 T	97
6.17. $^{23}\text{Na}$ MAS NMR spectrum of $\text{Na}_2\text{Mo}_2\text{O}_7$ at 14.1 T	98
6.18. $^{23}\text{Na}$ MQMAS NMR of YP4 at 21.1 T	101
6.19. $^{95}\text{Mo}$ MAS NMR spectra of Cr-containing model <i>yellow phase</i> samples	103
7.1. $^{133}\text{Cs}$ MAS NMR spectra of iron series glasses	116
7.2. $^{23}\text{Na}$ MAS NMR spectra of iron series glasses	119
7.3. Experimental and simulated $^{23}\text{Na}$ MAS NMR spectrum of glass Fe-3	120
7.4. $^{11}\text{B}$ MAS NMR spectra of iron series glasses	122
7.5. $^{[3]}\text{B}$ and $^{[4]}\text{B}$ FWHM values as a function of glass paramagnetic content (all data)	123
7.6. Broadening factors for $^{[3]}\text{B}$ and $^{[4]}\text{B}$ as a function of glass paramagnetic content	125
7.7. $^{133}\text{Cs}$ MAS NMR spectrum of $\text{YP}_{\text{Fe}}$	127
7.8. Deconvolution of $^{133}\text{Cs}$ MAS NMR profiles for $\text{YP}_{\text{Fe}}$	128
7.9. $^{23}\text{Na}$ MAS NMR spectrum of $\text{YP}_{\text{Fe}}$	129
7.10. $^{23}\text{Na}$ MQMAS NMR of $\text{YP}_{\text{Fe}}$ at 14.1 T	130

## Chapter 1

# Disposal of Nuclear Waste

*Nuclear power plays an important role in the global energy supply and is an environmentally-friendly renewable resource with exceptionally low carbon emissions. However, the implementation of nuclear power requires vigilant consideration regarding the disposal of radioactive waste products from the nuclear fuel cycle. High-level waste products generated by the reprocessing of spent nuclear fuel are primarily disposed of by vitrification, where the waste components are immobilised in a glassy matrix and then cooled to create a solid wasteform. Host glass compositions must be capable of accommodating a broad range of components and have other stringent requirements to be considered for long-term storage. Poor solubility of certain waste products leads to phase separation of crystalline species, which may act as vehicles for the escape of radioactive nuclides.*

### 1.1 The Nuclear Fuel Cycle

Forecasted increases in the global energy demand require implementation of many alternative and renewable energy sources. Nuclear power is an established global commodity, and development of nuclear power plants continues worldwide. The basis for nuclear power lies in the *nuclear fission* reaction, where fuel rods containing fissile nuclides, predominantly uranium ( $^{235}\text{U}$ , as  $\text{UO}_2$ ) and plutonium ( $^{239}\text{Pu}$ , as  $\text{PuO}_2$ ), undergo neutron bombardment and split to produce two lighter nuclides (centered around mass numbers 95 and 135) and additional neutron particles. The energy released upon fission, including the kinetically-active products, gamma

radiation, and subsequent chain reactions contribute to bulk heat generation. This heat is absorbed by a nuclear reactor coolant (typically water) to produce steam that can be pressurised and directed to turbines for power generation [1,2].

Beyond the fundamentals of nuclear fission, there are variants in the handling of waste products generated by the process. When the efficiency of the fission chain reaction diminishes, the reacted material is considered *spent fuel*, which contains depleted uranium (i.e., lower  $^{235}\text{U}$  content), various fission products, and transuranic elements such as plutonium, neptunium, americium, and curium [3]. An *open nuclear fuel cycle*, employed by nuclear power plants in North America, involves disposal of the spent fuel in secure containers in geological repositories. The *closed nuclear fuel cycle* approach, employed by most European and Asian nuclear power plants, aims to reprocess the spent fuel by a series of chemical extraction processes in order to salvage unreacted fissile  $^{235}\text{U}$  and  $^{239}\text{Pu}$  that can be assimilated into new fuel rods. This process succeeds in producing a lower volume of waste, as the majority of the fuel rod can be salvaged. Nitric acid is used to dissolve the spent fuel rod, a chemical extraction solvent is applied to gather the  $^{235}\text{U}$  and  $^{239}\text{Pu}$ , and the remainder may be neutralised by the addition of alkali and concentrated by evaporation. Consequently, the waste solution (high-level liquid waste, HLW) contains a variety of nuclides (can be upwards of 50 different oxides), including various fission products (e.g.,  $^{90}\text{Sr}$ ,  $^{99}\text{Tc}$ ,  $^{129}\text{I}$ , and  $^{137}\text{Cs}$ , among others), transition metal corrosion products (e.g., Fe, Ni, and Cr), minor actinides (transuranic elements), and residual components from the extraction process (e.g. salts and organic compounds) [2]. Compositional variations exist by region, resulting from differing specifications of the nuclear reactor, but the waste components are generally consistent across multiple HLW streams (Table 1.1) [1]. With such a complex and dynamic waste mixture, selection of an appropriate material for disposal becomes an important and complicated issue.

**Table 1.1.** Selected HLW compositions <sup>a</sup> (in g/L)

	<b>Hanford (USA)</b>	<b>Savannah River (USA)</b>	<b>Sicral 1 (France)</b>	<b>Magnox (UK)</b>	<b>HEWC (Belgium)</b>	<b>Tokai (Japan)</b>
<b>Al</b>	1.5	7.7	32.5	26.0	44.0	-
<b>Na</b>	4.1	5.9	20.5	-	1.9	44.5
<b>K</b>	-	0.3	-	-	-	-
<b>Mg</b>	-	0.2	4.0	30.0	-	-
<b>Fe</b>	6.1	29.7	16.0	13.0	1.3	8.4
<b>Ni</b>	0.6	2.8	1.5	1.4	-	2.2
<b>Cr</b>	0.1	0.3	1.5	1.6	0.1	2.2
<b>Mo</b>	0.2	0.2	-	10.8	-	-
<b>Zr</b>	3.4	0.6	-	11.8	-	-
<b>Hg</b>	-	1.8	-	-	2.8	-
<b>Cl</b>	0.1	0.9	-	-	-	-
<b>SO<sub>4</sub></b>	0.2	0.8	-	-	3.2	-
<b>NO<sub>3</sub></b>	2.8	4.2	-	11.0 M	-	-
<b>FP</b>	< 2.5	< 3.0	24.5	-	0.5	49.0
<b>TRU</b>	< 0.1	< 0.2	3.0	2.0	0.1	12.6

<sup>a</sup> Data from [4]

HEWC: Highly-Enriched Waste Concentrate

FP: Fission Products

TRU: Transuranic Elements

M: mol/L

## **1.2 Immobilisation of High-Level Nuclear Waste**

In addition to the standard health and safety risks associated with many of the waste components, the radioactivity of the fission products needs to be considered when addressing disposal of HLW. Proper selection of a storage facility is crucial to the overall disposal strategy, where waste canisters are stored in geological environments with low seismic activity and a low propensity to the migration of groundwater. In the short term (e.g., up to 50 years), disposal of the waste in liquid form is adequate, but long-term storage requires that the material be immobilized as a solid, offering greater stability and durability over the necessary timescale (i.e., over 1000 years). Development and utilisation of a particular solid wasteform depends on several factors, such as the ease of its fabrication and processing, waste-loading capabilities (and flexibility to house radionuclides), bulk radiation stability, and long-term durability [5, 6]. Various families of solid wasteforms exist, including (but not limited to) glasses (borosilicate and phosphate), ceramics (mineral analogues), and glass composite materials (glass-ceramics) [1]. Ceramic-based wasteforms are advantageous for storage of refractory (i.e., high melting point) and volatile (e.g., halogen) compounds, however glasses show superior properties in other categories (i.e., preparation, waste loading, etc.) and are the dominant wasteform used for HLW immobilisation, so further discussion will focus exclusively on the advantages of vitrification.

The high-temperature melts of glasses provide exceptional solvation for incorporating a wide variety of waste products, and upon vitrification, form a homogenous solid that offers superior handling. Finely tuned compositions of borosilicate (B-Si) glass have become the leading wasteform for the storage of HLW and are currently utilised in operations in the United Kingdom, France, Germany, Belgium, and the United States (for the storage of defence wastes). Due to its moderate processing temperature and high chemical durability, B-Si glass represents a judicious balance between manufacturing concerns and long-term storage necessities [2,6]. The

start-up and operational costs of the vitrification process are relatively high, but become economically feasible provided that a large volume of waste is processed. A typical storage canister contains 163 litres of HLW glass and weighs 400 kg; collectively, vitrification plants in Europe produce around 2500 canisters per year. Disposal of the canisters involves a two-stage process. The canisters are first placed in specially designed retention pools of water for around 40-50 years to lose the majority of their radioactivity, then are transported and stored underground in a geological setting (typically natural clay, rock, or salt environments). Protection by corrosion-resistant stainless steel and clay overpack material ensures the glass remains safe from penetration by groundwater [7].

### 1.3 Phase Separation in HLW Glasses

The molten glass-forming components are capable of incorporating a large number of waste constituents as a homogenous matrix upon vitrification. In actuality, the presumed homogeneity is broken up by gas bubbles and immiscible fission products, including molybdates, sulfates, and halides. For example, the high field-strength ( $z/r^2$ , where  $z$  is valence and  $r$  is the metal-oxygen bond length) of the  $\text{Mo}^{6+}$  cation exerts strong influence on the bonding of its surrounding oxide environment, and molybdenum favours existence as  $[\text{MoO}_4]^{2-}$  species that charge-balance by crystallisation with univalent and divalent cations (including  $\text{Na}^+$ ,  $\text{Cs}^+$ , and  $\text{Ca}^{2+}$ ). These crystalline products isolate from the glass as a multi-component phase assemblage, coined “*yellow phase*” due to its coloured appearance. The term *yellow phase* is somewhat general, as it does not define an exact crystalline composition, and is applied to the phase assemblage as a whole, which may contain any number of molybdate phases among other phase-separated crystalline components [8,9].

Several issues arise with the occurrence of phase separation in borosilicate waste glasses. Most importantly, the poorly durable crystalline phases may contain radioactive atoms (e.g.,  $^{135}\text{Cs}$ ,  $t_{1/2} = 2.3$  million years), and contact with groundwater would release these radioactive compounds into the environment. Furthermore, degradation of the glass network by phase separation causes a larger surface area to become accessible for penetration by water. To counter this effect, waste loadings with components such as Mo are generally restricted to below particular solubility limits (1-2 wt%  $\text{MoO}_3$ ), but the cooling rates of such a large volume of HLW glass are sufficiently low that the possibility of crystallisation remains [10,11]. Therefore, glass compositions must fulfill the aforementioned chemical/mechanical requirements and have a high loading capacity for insoluble components. The discrete compositional differences of various waste glasses are explored in Chapter 2.

#### 1.4 Experimental Techniques for Studying HLW Glasses

The diverse and multiphasic nature of phase-separated HLW glass presents unique challenges for routine characterisation techniques, and their inherent radioactivity adds another layer of complexity that must be addressed. The *Commissariat à l'énergie atomique et aux énergies alternatives* (CEA, Atomic Energy and Alternative Energies Commission) is dedicated to the development of the nuclear power program in France and houses facilities that explore multiple aspects of nuclear waste disposal through vitrification, including radiation damage to glasses. Experimental approaches for modelling radiation effects involve doping model waste glasses using short-lived actinides ( $^{242}\text{Cm}$ ,  $^{244}\text{Cm}$ ,  $^{238}\text{Pu}$ ) that provide levels of radiation equivalent to those observed over several thousands of years in actual HLW glasses. A series of glasses prepared with increasing mol%  $^{244}\text{Cm}$  showed, for example, that alteration rates (propensity to leaching upon contact with water) are not affected by higher radionuclide concentration or



cumulative alpha-radiation dosage. Improved mechanical properties, including decreased hardness and a greater fracture resistance, indicated a less brittle glass resulting from slight swelling (decreased density) upon irradiation. Nevertheless, irradiation of borosilicate glass is principally unfavourable because of the structural depolymerisation that occurs from the ballistic recoil events of alpha decay [12].

The majority of HLW glass studies, however, are conducted on inactive model systems, which serve as analogues for investigating trends in glass structure, mechanical properties, aqueous performance, and crystallisation products. Routine methodologies, including x-ray diffraction (XRD) and transmission electron microscopy (TEM), are frequently applied to examine crystallisation products and visualise phase-separated regions within glass, respectively [9]. The occurrence of phase-separated crystalline molybdates has been detected using extended x-ray absorption fine structure spectroscopy (EXAFS), revealing the tetrahedral coordination of Mo in  $[\text{MoO}_4]^{2-}$  and elucidating the Mo-O bond length [9,13]. Similarly, Raman spectroscopy detects the stretching and vibrational modes of Mo-O bonds in  $[\text{MoO}_4]^{2-}$  species, and shows sensitivity to the particular charge-compensating counter-cation [10]. A related technique, Fourier-transform infrared (FTIR) spectroscopy, has been used to investigate alteration rates through quantification of  $\text{H}_2\text{O}$  and  $\text{SiOH}$  vibration signals of HLW glass prepared in a leachant solution [14]. Compositional analyses, including electron microprobe analysis (EMPA) and inductively coupled plasma (ICP) spectrometry/spectroscopy, are commonly used to verify model compositions after vitrification and account for any changes from the nominal amounts [15,16].

While many characterisation techniques contribute unique perspectives to the analysis of HLW glasses, there are particular limitations that hinder their ability to examine phase separation. One issue is that glasses lack long-range periodicity, which can affect the

detectability of phase-separated products. For example, XRD patterns of HLW glass samples are greatly obscured by the contribution of a broad amorphous pattern, which makes it difficult to detect and identify peaks of low-concentration crystalline components [17a]. Another issue when characterising HLW glasses is related to the sampling ability of a technique. For example, X-ray Photoelectron Spectroscopy (XPS) uses characteristic electron binding energies to identify and quantify the elemental composition of a sample, however it is best applied for surface analysis rather than bulk analysis [17b].

The heterogeneity of a phase-separated HLW glass necessitates the use of techniques that can readily distinguish and quantify multiple atomic structural environments of the bulk material. Solid-state nuclear magnetic resonance (NMR) is capable of detecting isotope-specific signals from both glassy and crystalline environments, and has been making significant contributions to the understanding of structural modifications and phase-separation in HLW glasses [6,10,15,16,18-21]. By offering isotope selectivity, NMR is capable of individually probing the structural environments of nuclides of interest, and a comprehensive structural characterisation can be obtained through a multinuclear approach. However, the presence of transition metal oxides in the waste composition (see Table 1.1) challenges the utility of solid-state NMR, as the unpaired electrons in paramagnetic cations interact with NMR-active nuclei and create (generally) unfavourable broadening and relaxation effects (see Chapter 3, section 3.3.5). In working towards understanding NMR analyses of industrial glass compositions, it is important to study individual transition metal oxides in model HLW glasses. The work in this thesis demonstrates a systematic approach for the addition of paramagnetic and diamagnetic oxides to simplified model HLW glass systems and their characterisation through solid-state multinuclear magnetic resonance.

## Chapter 2

# Chemical Description of Glasses

*Glasses are an extremely diverse class of material and offer many commercial applications. The suitability of glasses to house high-level nuclear waste is attributed to their unique structural characteristics at the atomic level. Glass components can be broadly defined as network formers or modifiers, and their precise ratios allow for extensive tuning of bulk properties. For HLW glass compositions, such tuning is essential to arrive at compositions that accommodate a particular distribution of waste components.*

### 2.1 Thermodynamics of Glass Formation

*Glasses* are amorphous solids that lack long-range periodicity and form during cooling of a high-temperature melt, displaying characteristic thermodynamic behaviour distinguished from crystalline solids with the onset of their formation (Figure 2.1). In the case of crystalline solids, a high-temperature melt cooled through the melting point ( $T_m$ ) will show spontaneous atomic ordering as it packs into an organised solid, marked by a sharp discontinuity in its thermodynamic properties (e.g., enthalpy or molar volume). Smaller changes in enthalpy or volume on either side of  $T_m$  reflect the heat capacity of the material. Glasses, on the other hand, begin to form when the melt is cooled below  $T_m$  without crystallisation, generating a *super-cooled liquid* that displays small structural and enthalpic changes as the temperature is decreased. Upon cooling, the viscosity of the super-cooled liquid gradually increases and eventually reaches a point where the structural units cannot appreciably rearrange any further, generating a kinetically arrested solid, the thermodynamic properties of which are controlled linearly by the

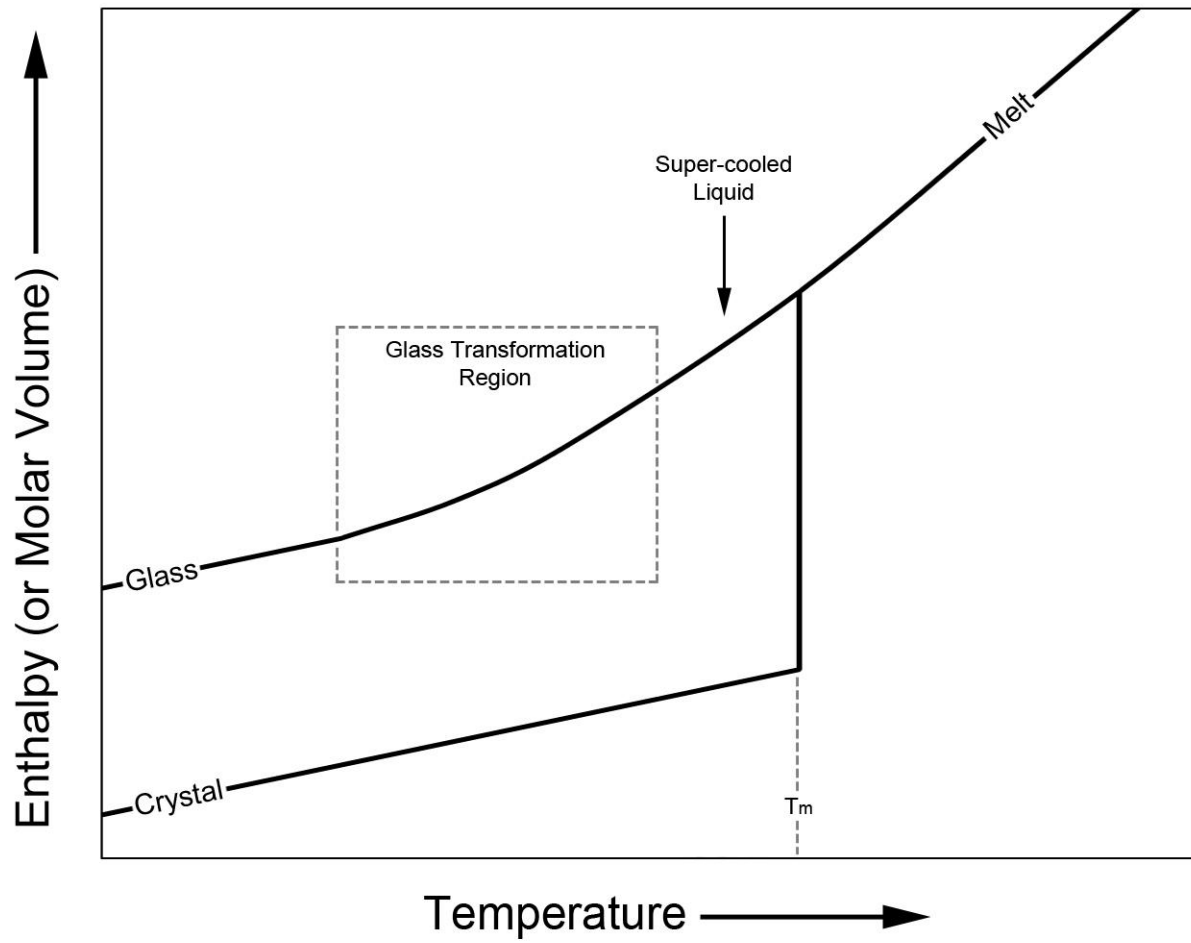


**Figure 2.1.** Thermodynamic plot showing the different paths of glass and crystal formation upon cooling of a high-temperature melt below its melting point ( $T_m$ ).

heat capacity. The *glass transformation* is defined as the region where the thermodynamic properties deviate from the linearity of the heat capacity and can be quoted as either a range or single value ( $T_g$ ) [22].

## 2.2 Classification of the Glass Network

The basic principles governing the atomic structure of glasses were established by Zachariasen in 1932 [23]. The model proposed that the formation of a glassy structure can be attributed to materials that contain cations with trigonal and/or tetrahedral coordination to oxygen<sup>1</sup>, corner-sharing polyhedral connectivity, and oxygen atoms that are bound to strictly only two cations. Indeed, the aforementioned characteristics describe excellent glass structure; however, glasses have been found to exist with higher-coordinate environments [24] and singly-bound, positively charged oxygen atoms (i.e., *non-bridging oxygens*) [25]. Appropriately, a classification scheme exists to distinguish the behaviour and effects of specific ionic components within a glass.

### 2.2.1 Network Formers

The term *network former* is applied to cations that exhibit the capacity to establish a vitreous network, displaying the bulk thermodynamic and atomic structural properties outlined above. The bond character between the cation and anion (typically oxygen) establishes glass-forming ability. Examples of good glass formers include  $\text{SiO}_2$ ,  $\text{B}_2\text{O}_3$ , and  $\text{P}_2\text{O}_5$ , whose network-forming cations ( $\text{Si}^{4+}$ ,  $\text{B}^{3+}$ , and  $\text{P}^{5+}$ ) have ideal fractional ionic character that displays a fortuitous balance between electronegativity and polarisability differences to oxygen ( $\text{O}^{2-}$ ) [22,26].

---

<sup>1</sup> Zachariasen also considered the glass-forming ability of  $\text{BeF}_2$  [23].

### 2.2.2 Network Modifiers

The term *network modifier* is applied to ions with highly ionic character that create positive charge within the glass. The structural units of network formers become modified to provide charge-balancing mechanisms to maintain bulk neutrality (Figure 2.2). Common network modifiers include alkali and alkaline-earth oxides (e.g.,  $\text{Li}_2\text{O}$  ( $\text{Li}^+$ ),  $\text{Na}_2\text{O}$  ( $\text{Na}^+$ ),  $\text{CaO}$  ( $\text{Ca}^{2+}$ )), and heavy metals (e.g.,  $\text{PbO}$  ( $\text{Pb}^{2+}$ )) that are added to tune bulk properties such as melting temperature and viscosity [22,26].

### 2.2.3 Intermediate Formers

The term *intermediate formers* refers to ions that do not display glass-forming ability alone, but can augment an established glass network to provide tuning of bulk properties while maintaining network connectivity. Examples of intermediate formers include  $\text{Al}_2\text{O}_3$  ( $\text{Al}^{3+}$ ),  $\text{Ga}_2\text{O}_3$  ( $\text{Ga}^{3+}$ ), and  $\text{TiO}_2$  ( $\text{Ti}^{4+}$ ), which display greater ionic character (than *network formers*) with higher-coordinate environments, and generally strengthen glass when added in small amounts [22,26].

## 2.3 Waste Glass Compositions

Vitrification of nuclear waste requires host glass compositions that provide good solubility of waste constituents, a low propensity to phase separation (crystallisation), a high degree of chemical durability, and a low processing temperature [2]. In actuality, no single glass composition can fulfill all required properties, so HLW glass design resides in compositional tuning as a means to appropriately balance these considerations. Vitrification of HLW with pure silicate ( $\text{SiO}_2$ ) glass would provide the best long-term durability, however the melting temperature (around  $1700^\circ\text{C}$ ) is too high for scaling to the required industrial volumes. Furthermore, processing temperatures should stay below  $1200^\circ\text{C}$  to minimise volatilisation of Ru

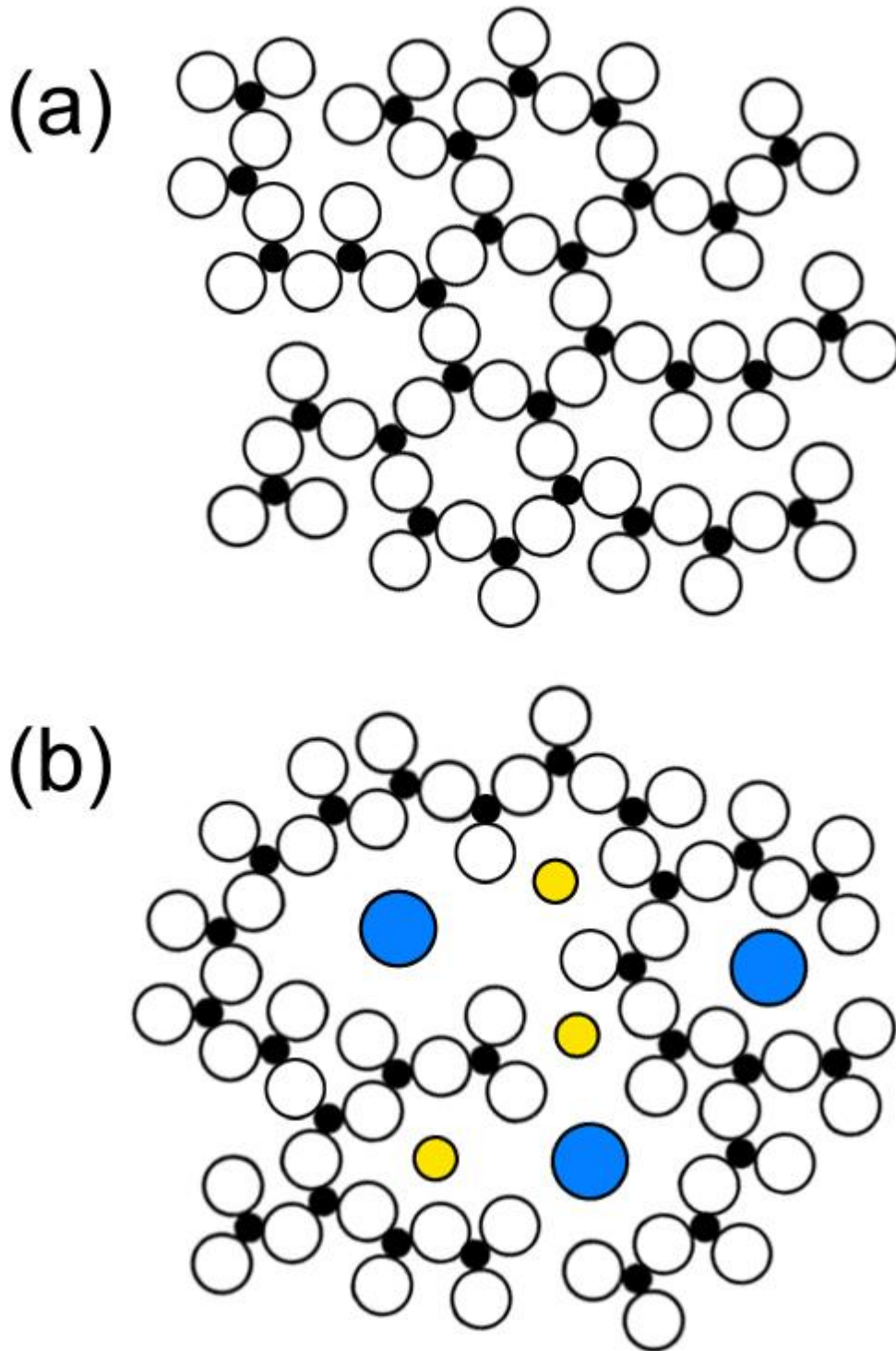


**Figure 2.2.** Two-dimensional representation of a glass network for (a) pure  $\text{SiO}_2$  glass (Si=black, O=white) and (b)  $\text{SiO}_2$  with  $\text{Na}^+$  (yellow) and  $\text{Cs}^+$  (blue) network modifier cations. Silicon polyhedra contain another oxygen atom out of the plane of the page.

and Cs radionuclides. Boron ( $B_2O_3$ ) and sodium ( $Na_2O$ ) oxides are added to silicate as fluxing agents, which lend their low melting temperatures to produce a sodium-borosilicate (Na-B-Si) glass with moderate processing temperature ( $\sim 1200^\circ C$  or lower, depending on additional components) whilst maintaining the strength, chemical durability, and waste loading capability ( $\sim 30$  wt%) required for housing HLW. Other commonly added network modifiers in Na-B-Si waste glasses include  $Al_2O_3$ ,  $CaO$ ,  $MgO$ ,  $TiO_2$ , and  $ZrO_2$  [1,2].

The immiscibility of several waste constituents in Na-B-Si glass, including molybdenum and sulfur, has led to the consideration of alternative glass compositions, namely in the form of aluminophosphate ( $Al_2O_3$ - $P_2O_5$ ) glasses. Primarily used by Russia,  $Al_2O_3$ - $P_2O_5$  glasses possess low processing temperatures and a high solubility for sulfates and metal oxides. However, they have markedly lower chemical durability and thermal stability than borosilicates and are highly corrosive, so their applications are limited to low loadings ( $\sim 10$  wt%) of suitable waste compositions [1,2].

The composition of the French reference waste glass “SON68” is described in Table 2.1. Solid-state NMR analysis of the 28-component SON68 described in Table 2 would be difficult to interpret without an understanding of the contributions of each individual component. Therefore, the composition can be simplified to yield model compositions by using only the essential vitreous network components ( $SiO_2$ ,  $B_2O_3$ , and  $Na_2O$ ) together with waste components of interest ( $MoO_3$  and  $Cs_2O$ ) as a means of observing the fundamental phenomena of interest (e.g. phase separation of crystalline species) [16,20]. The model compositions for the work of this thesis, which explore transition metal additives in a simplified HLW glass composition, are detailed in Chapter 5 (array of transition metal additives), Chapter 6 (chromium-containing HLW glasses), and Chapter 7 (iron-containing HLW glasses) accordingly.



**Table 2.1.** Composition of the reference HLW glass SON68<sup>a</sup>

Oxide	mol%
SiO <sub>2</sub>	52.57
B <sub>2</sub> O <sub>3</sub>	13.99
Na <sub>2</sub> O	11.05
CaO	5.00
Li <sub>2</sub> O	4.60
Al <sub>2</sub> O <sub>3</sub>	3.34
ZnO	2.13
ZrO <sub>2</sub>	1.49
Fe <sub>2</sub> O <sub>3</sub>	1.27
MoO <sub>3</sub>	0.82
NiO	0.69
MnO <sub>2</sub>	0.58
Cs <sub>2</sub> O	0.35
Nd <sub>2</sub> O <sub>3</sub>	0.33
BaO	0.27
Cr <sub>2</sub> O <sub>3</sub>	0.23
Pr <sub>2</sub> O <sub>3</sub>	0.23
SrO	0.22
Ce <sub>2</sub> O <sub>3</sub>	0.20
La <sub>2</sub> O <sub>3</sub>	0.19
P <sub>2</sub> O <sub>5</sub>	0.14
CoO	0.11
TeO <sub>2</sub>	0.10
Y <sub>2</sub> O <sub>3</sub>	0.06
CdO	0.02
Ag <sub>2</sub> O	0.01
SnO <sub>2</sub>	0.01
Sb <sub>2</sub> O <sub>3</sub>	< 0.01

<sup>a</sup> Data from [6]

## Chapter 3

# Solid-State NMR Spectroscopy

*Nuclear magnetic resonance spectroscopy involves the manipulation and observation of nuclear spins within a magnetic field as a means to obtain useful structural and coupling information. As an isotope-selective probe, NMR spectroscopy is a powerful tool for distinguishing atomic environments, and is therefore suitable for the characterisation of heterogeneous HLW materials. The efficacy of a particular NMR-active isotope is governed by several intrinsic properties - including natural abundance, spin number, and resonance frequency. Due to several interactions and coupling effects (including those presented by paramagnetic cations) NMR spectroscopy of solids requires special considerations and instrumentation to overcome various experimental challenges.*

### 3.1 Nuclear Magnetic Resonance Theory

The properties *nuclear magnetism* and *nuclear spin* allow a nucleus to interact with a magnetic field. Nuclear spin is defined by the *spin quantum number* ( $I$ ) and must be a non-zero integer or half-integer value for a particular isotope to be “NMR-active”. When placed in a magnetic field, the degeneracy of a spin-active nucleus is split into  $2I+1$  spin states (the *Zeeman interaction*), allowing energetic transitions between them in the radiofrequency (rf) range. The excitation energy is determined by the gyromagnetic ratio ( $\gamma$ ) of the nucleus, an intrinsic isotopic property that relates resonance frequency and magnetic field strength ( $B_0$ ), given by the following:

$$\Delta E = \gamma \hbar B_0 \quad (3-1)$$

Separation between spin states increases linearly with magnetic field strength, generating more favourable population distributions according to the Boltzmann equation (Figure 3.1).

From a physical standpoint, nuclear spins placed in a magnetic field precess in a conical path about the  $B_0$  axis at its *Larmor frequency* ( $\gamma B_0/2\pi$ ), generating a bulk magnetisation along the  $z$  axis (collinear with  $B_0$ ) (Figure 3.2a). A coil surrounding the sample is used to apply an rf pulse at the Larmor frequency, generating a magnetic field ( $B_1$ ) along an orthogonal axis that causes the nuclear spins to tip and precess about  $B_1$ , thus transferring the bulk magnetisation to the observable  $x$ - $y$  plane (Figure 3.2b). Magnetisation in the  $x$ - $y$  plane induces voltage in the coil, and is recorded as a decaying time-dependent signal as the spins relax (free induction decay, FID). The NMR spectrum is obtained through *Fourier transformation* of the time-domain FID signal to the frequency domain and is expressed as a *chemical shift*, or the difference in frequency (expressed in ppm) from a defined reference compound [27].

Signal decay is attributed to relaxation of the nuclear spins, and is controlled by two mechanisms. The first is known as the *spin-lattice relaxation time* ( $T_1$ ), which designates the time taken for the bulk magnetisation to re-establish along the  $z$  axis (Figure 3.2c), after which another pulse can be applied. The second is the *spin-spin relaxation time* ( $T_2$ ), which describes the coherence lifetime of nuclear spins in the  $x$ - $y$  plane (Figure 3.2d), and thus contributes to FID length [28].

### 3.2 Isotopic Properties

There are several intrinsic properties that contribute to the ease with which NMR experiments may be conducted on a specific nuclear isotope. Among others, the most significant properties

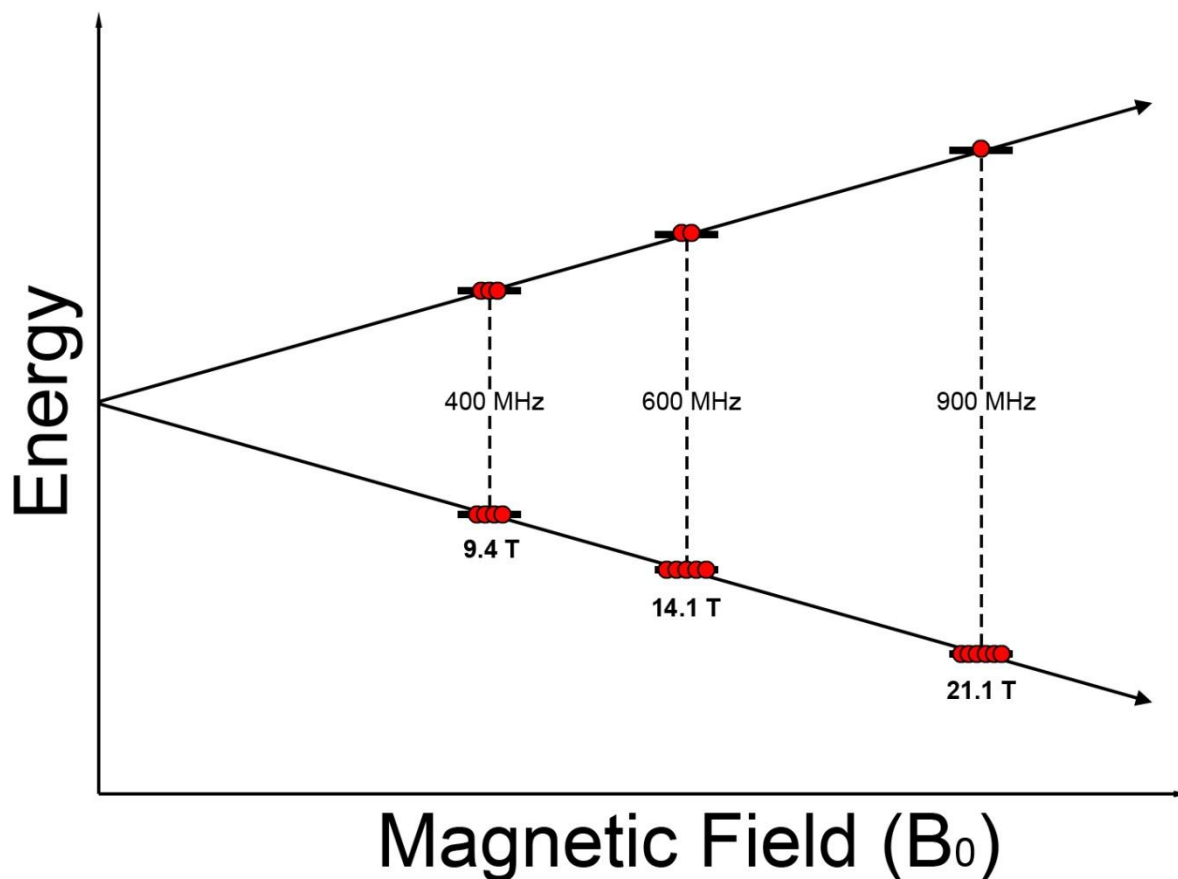


**Figure 3.1.** Relationship between Zeeman splitting and magnetic field strength, using  $^1\text{H}$  (spin- $1/2$ ) as an example. As the magnetic field strength ( $B_0$ ) increases, the separation between spin states increases linearly, reflecting the different rf frequencies required for excitation. The red circles denote the change to more favourable Boltzmann population differences with increased field strength (note: they are purely conceptual and do not reflect actual numerical populations).

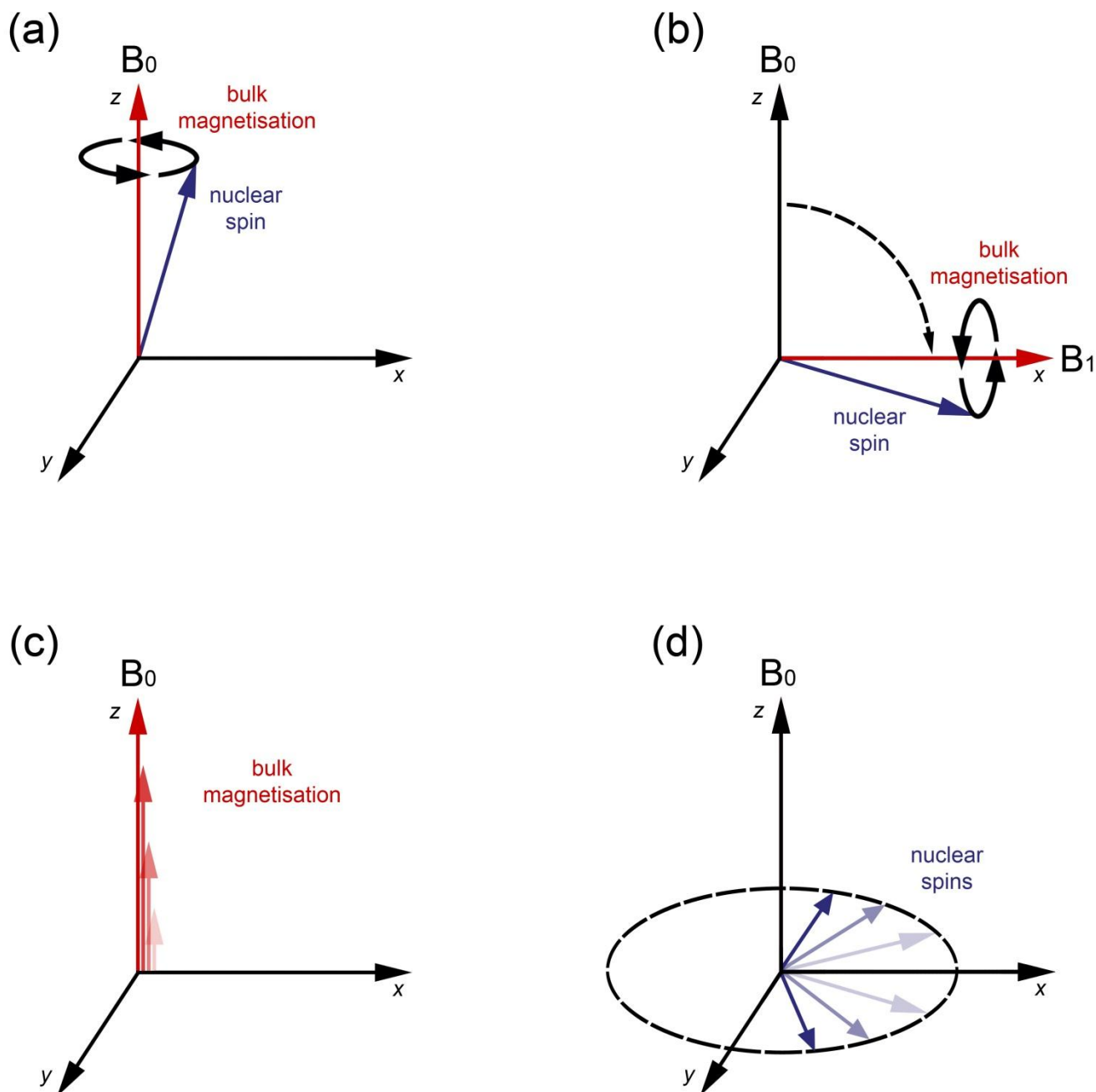


**Figure 3.2.** Spin description of an NMR experiment: **(a)** Precession of a nuclear spin about  $B_0$ , generating bulk magnetisation along the  $z$  axis. **(b)** Application of an rf pulse tips the magnetisation into the observable  $x$ - $y$  plane. Relaxation of the spins occurs by **(c)**  $T_1$  (spin-lattice) relaxation and **(d)**  $T_2$  (spin-spin) relaxation. (Note: the bulk magnetisation vectors in (c) are staggered for clarity only.)

include natural abundance, resonance frequency, and spin number. The practicalities of the NMR-active nuclides relevant for this study are explored in Chapter 4.

### 3.2.1 Natural Abundance

The occurrence of multiple isotopes makes it possible to find an NMR-active nucleus for nearly every element, and the natural abundance will impact the inherent strength of the NMR signal that is produced (see equation (3-2), below). Experiments on nuclei with low natural abundance generally require long collection times, although isotopic enrichment can be employed to enhance sensitivity. Examples of NMR-active isotopes with exceptionally low natural abundance include  $^{17}\text{O}$  (0.038%),  $^{33}\text{S}$  (0.75%), and  $^{43}\text{Ca}$  (0.135%) [28].

### 3.2.2 Resonance Frequency

The resonance properties of a particular nucleus are governed by  $\gamma$  and correspond to the energy separation (as in Figure 3.1) and precession frequency, where signal strength will continually increase with frequency (when all other properties are equal). Experiments on nuclei with low resonance frequency are often fraught with effects from low-frequency acoustic ringing of the instrument (ultrasonic waves in metallic components), but these may be overcome with the use of stronger magnetic fields to provide higher resonance frequencies. Natural abundance and resonance frequency together provide a means of scaling the *absolute receptivity* of NMR-active isotopes by the following relationship:

$$\gamma^3 C(I(I+1)) \quad (3-2)$$

where  $C$  is the natural abundance. It is clear that resonance frequency makes the largest contribution to receptivity. It is important to note that nuclei with high spin-number exhibit multiple transitions, which impacts their *relative receptivity* [29].

### 3.2.3 Spin Number

Nuclear isotopes are classified according to their spin quantum number: *spin- $1/2$  nuclei* ( $I = 1/2$ ) and *quadrupolar nuclei* ( $I > 1/2$ ), where the latter constitute the majority of NMR-active nuclei. With  $2I+1$  spin states generated in a magnetic field, the Boltzmann distributions for quadrupolar nuclei are sparser than spin- $1/2$  nuclei. Furthermore, quadrupolar nuclei exhibit multiple transitions, leading to unique spectral characteristics (Figure 3.3). The transitions are classified as the *central transition* ( $1/2 \rightarrow -1/2$  spin states) and a total of  $2I-1$  *satellite transitions* ( $\pm m \rightarrow \pm(m-1)$  for half-integer nuclei, where  $m = 3/2, 5/2, 7/2$ , and  $9/2$  for a spin- $9/2$  nucleus, and accordingly fewer for spin- $3/2$ , spin- $5/2$ , and spin- $7/2$  nuclei). The satellite transitions exhibit a breadth that extends to either side of the central transition and are characteristic of the strength and symmetry of the quadrupolar interaction (see below) [30].

## 3.3 NMR of Solids

A number of the interactions experienced by nuclear spins in a magnetic field are orientation-dependent, generating broad spectra that force unique demands on spectrometers designed to conduct NMR of solid samples. Molecular tumbling in solutions averages many of these interactions, and collection of solid-state NMR spectra is often more challenging than solution-state. However, it is possible to obtain a wealth of information through interpretation and quantification of the interaction parameters of a solid-state NMR spectrum.

### 3.3.1 Chemical Shift Anisotropy

The magnetic field experienced by an NMR-active nucleus is determined by its *chemical shielding*, which is a consequence of its molecular environment. *Isotropic* molecules with perfect spherical symmetry (e.g., tetrahedral) will exhibit identical shielding in every orientation, and a

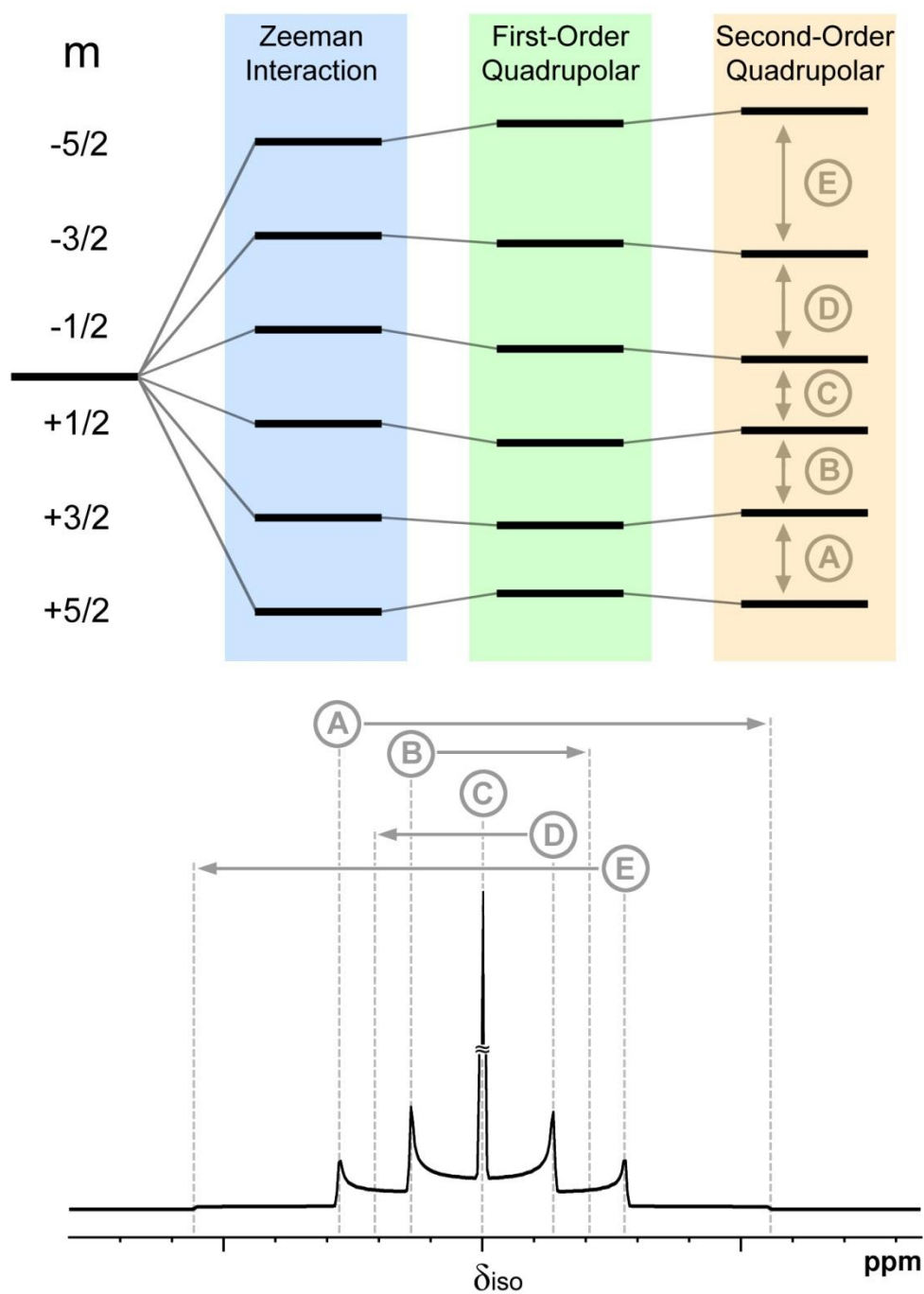


**Figure 3.3.** Energy level diagram of a quadrupolar nucleus (e.g., spin-5/2, with an arbitrary orientation of the *electric field gradient* (EFG) with respect to  $B_0$ ) (upper), showing the effect of the Zeeman interaction ( $B_0$ ) and first- and second-order perturbations to the spin states, generating the characteristic quadrupolar powder spectrum (lower) composed of the central transition (C) and  $2I-1$  satellite transitions (A,B,D,E). The corresponding breadth of each satellite transition is indicated by an arrow.



single sharp resonance will be observed. For *anisotropic* molecules, chemical shielding is dependent on the orientation of the molecule with respect to the magnetic field, and therefore the chemical shift changes as a molecule is rotated through different alignments (Figure 3.4a). A powdered solid sample exists as a statistical distribution of all possible molecular orientations, so the ‘chemical shift’ of anisotropic solids manifests as a continuous envelope that corresponds to each possible alignment (Figure 3.4b). The chemical shift is described by a second-rank tensor with three principal components ( $\delta_{11} \leq \delta_{22} \leq \delta_{33}$ ) and their average ( $\delta_{iso}$ ), conventionally described using the terms span ( $\Omega$ ) and skew ( $\kappa$ ):

$$\Omega = \delta_{11} - \delta_{33} \quad (3-3)$$

$$\kappa = \frac{3(\delta_{22} - \delta_{iso})}{\Omega} \quad (3-4)$$

The values of  $\Omega$  and  $\kappa$  reflect the local atomic structure, and elucidation of these parameters by peak-fitting provides useful insight on site symmetry [28].

### 3.3.2 The Quadrupolar Interaction

Quadrupolar nuclei exhibit a non-spherical distribution of charge about the nucleus. The *electric quadrupole moment* arising from this distribution couples with the surrounding *electric field gradient* with a strength that is characteristic of the atomic environment. The quadrupolar interaction is expressed by the quadrupolar coupling constant ( $C_Q$ ) and asymmetry parameter ( $\eta$ ):

$$C_Q = \frac{(eQ)(eq)}{h} \quad (3-5)$$

$$\eta = \frac{V_{YY} - V_{XX}}{V_{ZZ}} \quad (3-6)$$

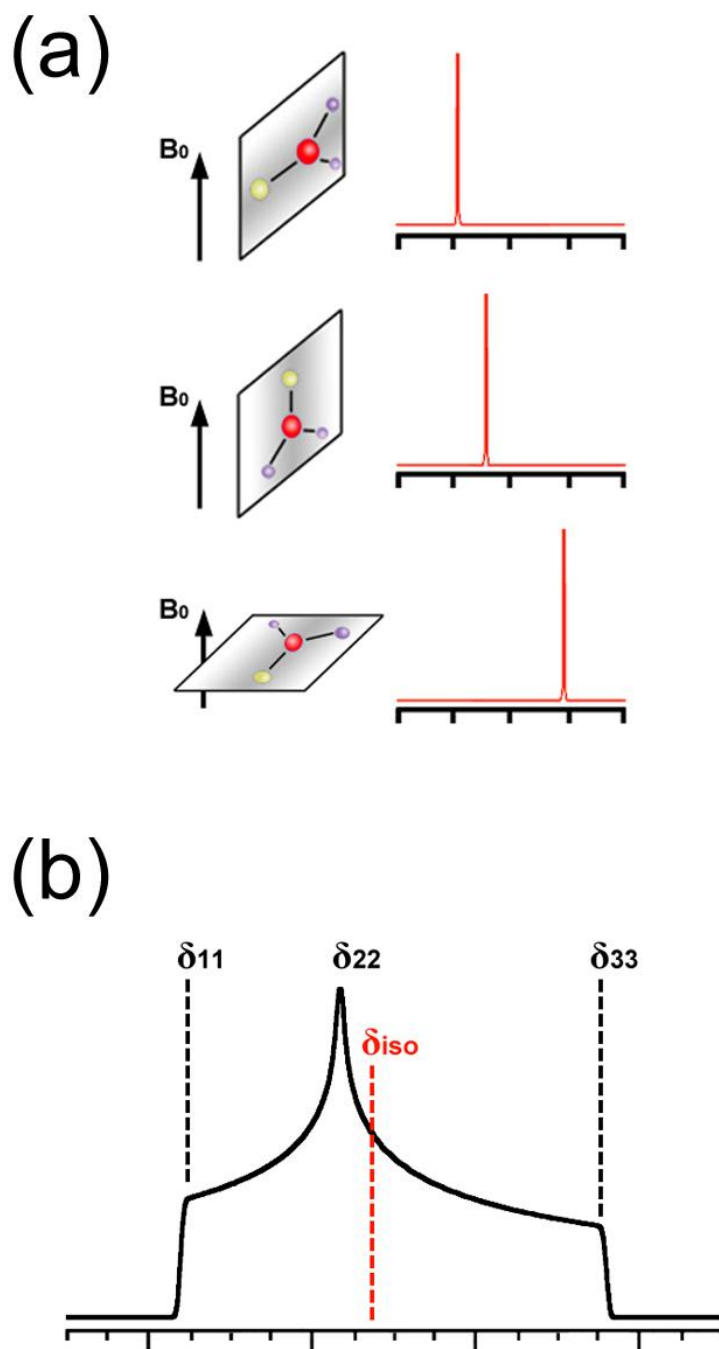


**Figure 3.4.** (a) *Chemical shift anisotropy* of a molecule; a unique chemical shift is obtained depending on the orientation of the molecule with respect to the magnetic field ( $B_0$ ). (b) Solid-state NMR spectrum of a powdered sample exhibiting a distribution of molecular orientations, yielding a broad site which is defined by the principal components ( $\delta_{11}$ ,  $\delta_{22}$ , and  $\delta_{33}$ ) and their average ( $\delta_{iso}$ ).

where  $eQ$  is the intrinsic nuclear quadrupole moment and  $eq$  is the largest component of the electric field gradient tensor ( $V_{zz}$ ). NMR peak shapes vary greatly with different  $C_Q$  and  $\eta$  combinations (Figure 3.5), providing additional discriminating characteristics to chemical shifts [30].

### 3.3.3 Spin-Spin Coupling

*Indirect spin-spin (J) coupling* is the interaction of nuclear magnetic moments through the electrons of adjacent chemical bonds.  $J$ -coupling is independent of magnetic field strength and is controlled by the  $I$  value of the coupling nucleus and the coupling constant ( $J_{12}$ ), which varies depending on the bonding system. When coupled, the NMR spectrum of the observed nucleus is split into  $2(nI)+1$  peaks, separated by  $J_{12}$ , where  $n$  is the number of coupled nuclei [28].

### 3.3.4 Dipolar Coupling

*Direct dipole-dipole coupling* describes the interaction between the magnetic fields generated from two nuclear spins. The dipolar interaction acts through space, meaning the adjacent nuclear spins need not be connected by a chemical bond. As a number of spin-active nuclei exist in a system, dipolar coupling is classified as *homonuclear (I-I)* or *heteronuclear (I-S)* according to the coupled nucleus. The dipolar interaction strength increases with the gyromagnetic ratio of the coupled nucleus and/or a decreased separation between them, as shown by equation (3-7):

$$H_D^{sec} = \frac{\mu_o}{4\pi} \frac{\gamma_1 \gamma_2 \hbar^2}{r_{12}^3} (A+B) \quad (3-7)$$

$$A = I_{1z} I_{2z} (3 \cos^2 \theta - 1) \quad (3-8)$$

$$B = -\frac{1}{4} [I_{1+} I_{2-} + I_{1-} I_{2+}] (3 \cos^2 \theta - 1) \quad (3-9)$$

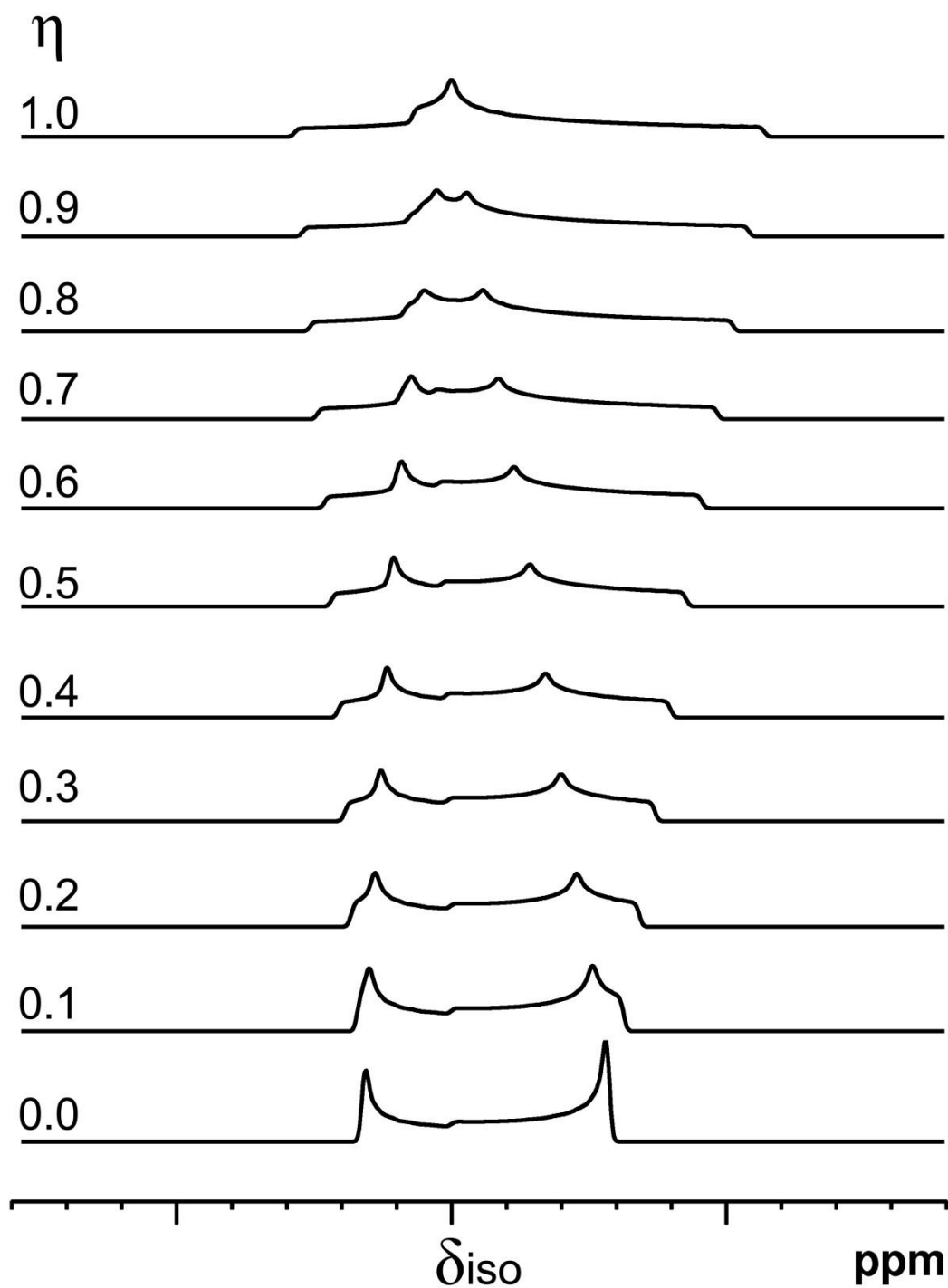


**Figure 3.5.** Effect of the quadrupolar asymmetry parameter ( $\eta$ ) on the solid-state NMR central transition of a quadrupolar nucleus. The above example uses the same  $C_Q$  for each  $\eta$  value; larger  $C_Q$  values would make the patterns broader while retaining their shape for a particular value of  $\eta$ .

where  $\gamma_1$  and  $\gamma_2$  are the gyromagnetic ratios of two coupled spins,  $r_{12}$  is the distance between the spins,  $\mu_o$  is the vacuum permeability constant, and  $\theta$  is the angle between the internuclear vector ( $I_1$ - $I_2$ ) and the magnetic field. Equation (3-7) describes only the secular (time-independent) portion of the dipolar interaction, with secular terms  $A$  and  $B$  as defined by equations (3-8) and (3-9), respectively. The non-secular (time-dependent) contribution (variables  $C$ - $F$ , not shown) is essentially averaged to zero due to the high frequency of the non-secular time dependency, and is therefore excluded in this treatment [28].

### 3.3.5 The Paramagnetic Interaction

The unpaired electrons of paramagnetic centres generate local magnetic fields that interact with nuclear spins and alter their spectral behaviour, most notably through chemical shift, peak broadening, and relaxation effects. A *paramagnetic centre* is defined as a nucleus containing unpaired electrons that shows a response to a magnetic field. From an NMR standpoint, the paramagnetic forms of *d*-block metals (e.g.,  $\text{Cr}^{3+}$ ,  $\text{Mn}^{4+}$ ,  $\text{Fe}^{3+}$ ,  $\text{Co}^{2+}$ ,  $\text{Ni}^{2+}$ ) exhibit the greatest effect on NMR experiments due to the highly localised electron density of *d* orbitals.

The paramagnetic interaction is manifested by two complementary mechanisms. The first is known as the *Fermi contact interaction*, which defines the interaction of a nuclear spin and an electron experienced through bonded orbitals. The observed isotropic chemical shift is displaced according to the *Fermi contact shift* ( $\delta_{\text{FC}}$ ), where the magnitude is controlled by the electron spin number ( $S$ ),  $\gamma$  of the nucleus, and temperature. Additionally, the *spin transfer mechanism* defines in which direction the peak will shift, with *spin-delocalised* systems (symmetry-compatible orbital overlap of electron and observed nucleus) displaying shifts to higher frequency with a negative temperature-dependence, and *spin-polarised* systems (polarisation from the unpaired

electron to an orbital adjacent to the observed nucleus) displaying shifts to lower frequency with a positive temperature-dependence [31].

The second mechanism by which the unpaired spin interacts with a nucleus is the *pseudo-contact interaction*, which defines the through-space magnetic interaction of an electron and nuclear spin. The mechanism is, in principle, identical to that of dipolar coupling (see above), however the strong magnetic moment of an electron spin leads to stronger couplings. As in Fermi contact, the chemical shift receives a contribution in the form of the pseudo-contact shift ( $\delta_{PC}$ ), although this is generally less significant than the Fermi contact shift [31].

In addition to the displacement of isotropic chemical shifts and broadening of the signal, strong relaxation effects are observed for nuclei in the presence of paramagnetic centres. The extent to which relaxation effects are observed is controlled by the Fermi- and pseudo-contact terms, thus faster relaxation is realised for high- $\gamma$  nuclei, closer proximity to unpaired electrons, electron relaxation rate, and coupling to centres with a higher  $S$  value. The relaxation effects of coupled electrons are often exploited to provide efficient collection times of nuclei with exceptionally long relaxation (e.g.  $^{29}\text{Si}$ , see Chapter 4), termed *paramagnetic relaxation enhancement*, by the addition of a small quantity of paramagnetic oxide [28].

### 3.4 Magic-Angle Spinning

As noted, the anisotropic nature of the interactions observed in NMR spectra of solids occurs due to their rigid structure, unlike the motional averaging provided by the solution state. Consequently, experimental methodologies have been developed that assist in eliminating or reducing various anisotropic, quadrupolar, and coupling effects. By far the most widely used hardware supplements for solid-state NMR spectroscopy are *magic-angle spinning* (MAS) probes (Figure 3.6a), which orient and rapidly rotate a sample container at an angle of  $54.74^\circ$

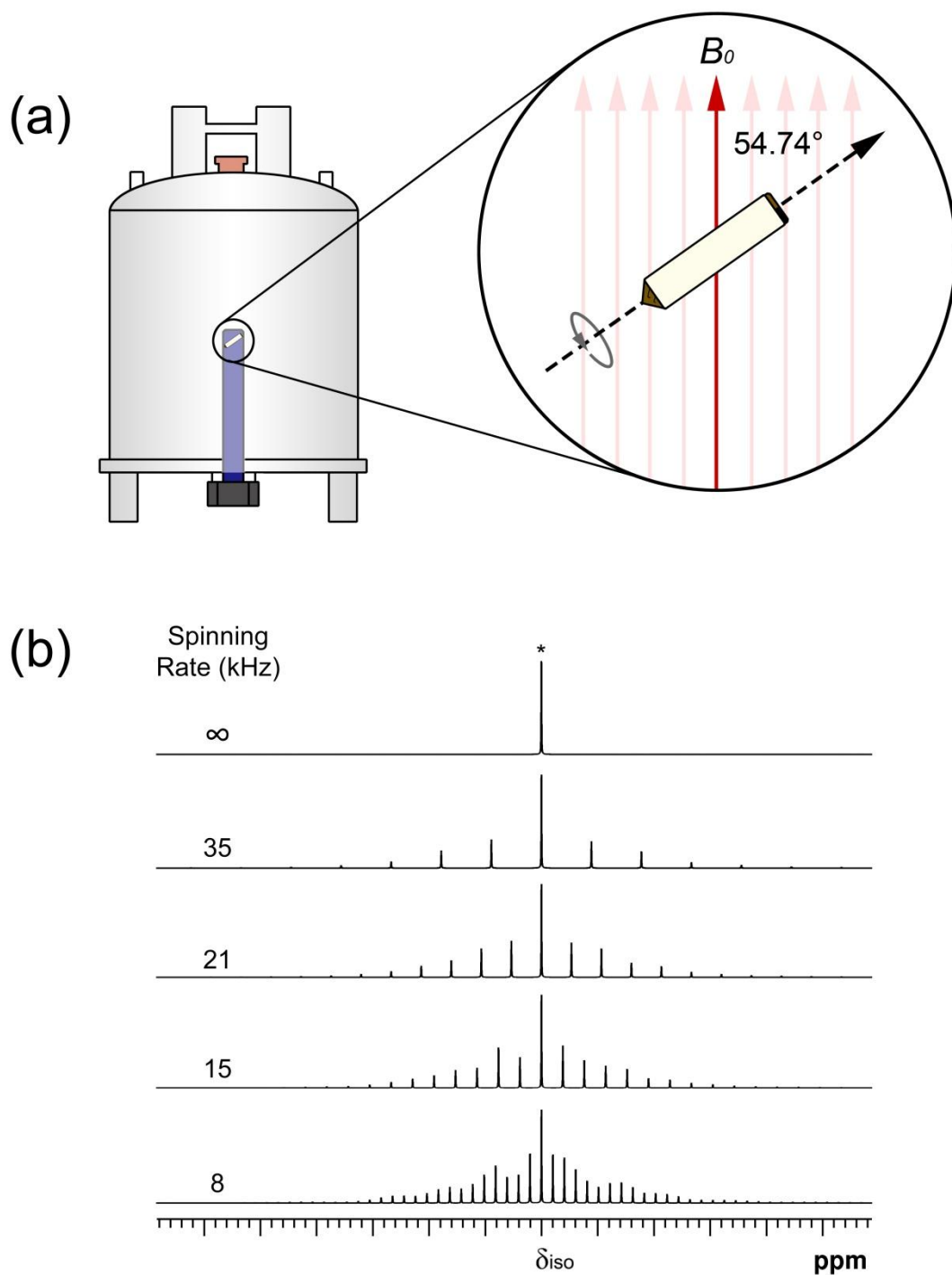


**Figure 3.6.** (a) An NMR spectrometer equipped for solids with a magic-angle spinning (MAS) probe. The sample rotor is oriented at  $54.74^\circ$  with respect to the magnetic field ( $B_0$ ) and rotated about its long axis. (b) The isotropic chemical shift of an MAS NMR signal exhibiting CSA stays fixed as the spinning rate is adjusted. At a (theoretical) infinite spinning rate, only the isotropic shift would be observed.

with respect to  $B_0$ . The “magic angle” is chosen precisely to solve the  $(3\cos^2\theta-1)$  term that defines the spatial dependencies of CSA, the first-order quadrupolar interaction, and dipolar coupling. An improvement in spectral resolution and signal-to-noise is obtained under MAS, where conventional probe designs can access MAS rates up to 70 kHz (i.e., 70 000 rotations/second). Chemical shift tensor spans are not typically overcome with moderate-to-high spinning rates (10-35 kHz), in which case a series of peaks appear on either side of  $\delta_{\text{iso}}$  separated by the spinning rate, known as *spinning sidebands*. The location of  $\delta_{\text{iso}}$  is not always obvious, but can be easily located by collecting spectra at different spinning rates as the position of  $\delta_{\text{iso}}$  remains fixed (Figure 3.6b) [32].



## Chapter 4

# NMR Nuclides of Model HLW Glass

*As expressed in Chapter 3, a number of intrinsic nuclear properties factor into the viability of NMR experiments of a particular nuclide. The complex compositions of nuclear waste glasses enable a large selection of NMR-active nuclides that can be used to probe glass structure and phase-separated crystalline products. Owing to the distribution of cesium and sodium cations in the glassy and crystalline phases, the protocol adopted for this study utilises  $^{133}\text{Cs}$  and  $^{23}\text{Na}$  NMR as primary characterisation tools for determining the degree of phase separation, although experiments using  $^{95}\text{Mo}$  are also attractive because of its centrality in phase separation. Characterisation of the glass phase can be accomplished with  $^{11}\text{B}$  and  $^{29}\text{Si}$  NMR, where additional sensitivity to paramagnetic cations allows for useful quantitative relationships to be established.*

### 4.1 Cesium-133 NMR

Cesium-133 is a spin-7/2 nucleus with a 100% natural abundance, moderate resonance frequency (79 MHz at 14.1 T), and low quadrupolar moment ( $Q = -0.343 \times 10^{-30} \text{ m}^2$ ). The high polarisability of the heavy cesium nucleus results in a large chemical shift range (~ 300 ppm for most oxides) that displays remarkable sensitivity to diverse chemical environments. Due to the low quadrupolar moment,  $^{133}\text{Cs}$  NMR experiments of crystalline cesium environments generally produce very sharp peaks with easily identified chemical shifts [33], and have been utilised for a wide variety of purposes, including detection of structural phase changes at different

temperatures [34], characterisation of the hydration state of Cs-adsorption on clays for nuclear waste storage [35], and identification of cation defects in pyrochlores [36]. The small quadrupolar interactions in  $^{133}\text{Cs}$  NMR are close in magnitude to that of chemical shift anisotropy, as demonstrated in non-spinning studies where the relative spatial orientation between the quadrupolar and magnetic shielding tensors (expressed as ' $\alpha$ ', ' $\beta$ ', and ' $\gamma$ ' *Euler angles*) requires special attention because of its dramatic impact on  $^{133}\text{Cs}$  lineshapes [37].

$^{133}\text{Cs}$  NMR experiments of cesium in glasses show a broad featureless peak that reflects the statistical distribution of structural environments taken by  $\text{Cs}^+$ . The “chemical shift” (peak centre) of cationic  $\text{Cs}^+$  has been shown to positively trend with increasing  $\text{Cs}_2\text{O}/\text{B}_2\text{O}_3$  ratio in borate glasses [38] and increasing  $\text{Cs}_2\text{O}/\text{P}_2\text{O}_5$  ratio in phosphate glasses [39]. In a model HLW glass, the sharp peaks of the phase-separated crystalline sites appear superimposed on the broad envelopes of glass-phase cesium [20], and deconvolution by simple peak-fitting with Gaussian and Lorentzian functions provides an accurate measure of cesium partitioning.

## 4.2 Sodium-23 NMR

Sodium-23 is a spin-3/2 nucleus with a 100% natural abundance, high resonance frequency (159 MHz at 14.1 T), and moderate quadrupolar moment ( $Q = 10.4 \times 10^{-30} \text{ m}^2$ ). The high receptivity of the  $^{23}\text{Na}$  nucleus has allowed characterisation of sodium environments for a variety of crystalline compounds [40,41] and Na-containing glasses [38,42]. Although the chemical shift range of  $^{23}\text{Na}$  is not particularly wide ( $\sim 75$  ppm), the sensitive quadrupolar interaction produces  $^{23}\text{Na}$  MAS NMR peaks of varying breadth and shape, offering a secondary means to recognise and assign sodium sites (provided an accurate spectral deconvolution can be determined).

In glasses, the charge-balancing  $\text{Na}^+$  cation is found in a variety of disordered environments, reflected in  $^{23}\text{Na}$  NMR as featureless Gaussian-type peaks that display minor

sensitivity to alkali loading and variances in coordination [38,42]. As with  $^{133}\text{Cs}$  NMR, the  $^{23}\text{Na}$  NMR signatures of Na-bearing crystalline sites are readily distinguished from glassy sodium sites, although the broad quadrupolar shapes make this identification less sensitive, and deconvolution of different patterns can be somewhat ambiguous. For this reason,  $^{23}\text{Na}$  NMR studies of heterogeneous materials are best conducted at multiple magnetic field strengths to exploit changes in resolution according to the field dependence of the quadrupolar interaction [41], or by using multiple-quantum MAS (MQMAS) experiments to separate  $^{23}\text{Na}$  sites in two dimensions [43,44].

### 4.3 Molybdenum-95 NMR

Molybdenum-95 is a spin-5/2 nucleus with a 15.9% natural abundance, low resonance frequency (39.1 MHz at 14.1 T), and a moderately low quadrupolar moment ( $Q = -2.2 \times 10^{-30} \text{ m}^2$ ). Despite the slightly higher resonance frequency of the  $^{97}\text{Mo}$  nucleus (spin-5/2, 39.9 MHz at 14.1 T), its lower natural abundance (9.6%) and larger quadrupolar moment ( $Q = 25.5 \times 10^{-30} \text{ m}^2$ ) encourages routine NMR experiments involving molybdenum to be carried out using  $^{95}\text{Mo}$ .

NMR experiments of  $^{95}\text{Mo}$  are undoubtedly attractive as the most direct measure and quantification of separated molybdate phases, however the lower relative receptivity of  $^{95}\text{Mo}$  (6.8% that of  $^{133}\text{Cs}$ , and 3.5% that of  $^{23}\text{Na}$ ) requires longer experimental collection times. However, despite nuclear properties that are less favourable than most NMR-active nuclei, a diverse set of Mo-containing compounds have been parameterised by  $^{95}\text{Mo}$  NMR [45-49]. Glassy  $^{95}\text{Mo}$  signatures for  $\text{MoO}_4$  and  $\text{MoO}_6$  coordination environments have been described for silver molybdate glasses [50], sodium phosphate glasses [51], and sodium borosilicate glasses [52], where related studies of the latter show that the  $^{95}\text{Mo}$  NMR signal of  $\text{MoO}_4^{2-}$  exhibits sensitivity to both boron ( $\text{B}_2\text{O}_3$ ) and calcium ( $\text{CaO}$ ) content [21].

#### 4.4 Boron-11 NMR

Boron-11 is a spin-3/2 nucleus with an 80.1% natural abundance, high resonance frequency (193 MHz at 14.1 T), and moderate quadrupolar moment ( $Q = 4.1 \times 10^{-30} \text{ m}^2$ ). Boron is commonly encountered as either trigonal ( $\text{BO}_3$ ) or tetrahedral ( $\text{BO}_4$ ) units that can be distinguished by their contrasting  $^{11}\text{B}$  NMR lineshapes, where three-coordinated boron ( $^{[3]}\text{B}$ ) produces broad quadrupolar shapes ( $C_Q \approx 2.5 \text{ MHz}$ ) around 12-20 ppm and four-coordinated boron ( $^{[4]}\text{B}$ ) produces relatively sharp peaks ( $C_Q \approx 0.5 \text{ MHz}$ ) near 0 ppm [53-55].

With boron as an important network-forming component in HLW glasses, the observation of  $^{11}\text{B}$  NMR can provide insight into changing glass structure as a function of compositional tuning. An important application of  $^{11}\text{B}$  NMR to glasses is the determination of the relative ratio of  $^{[3]}\text{B}$  and  $^{[4]}\text{B}$ , where resolution of these two peaks is achieved at sufficiently high magnetic field strengths ( $B_0 \geq 11.7 \text{ T}$ ) [6]. The presence of anionic units (i.e.,  $^{[4]}\text{B}$  or depolymerising  $^{[3]}\text{B}$  units with *non-bridging oxygen*, NBO) result from continual addition of glass modifiers, and numerous studies have traced  $^{[3]}\text{B}/^{[4]}\text{B}$  changes to explain the relationship between network connectivity and bulk properties under varying glass compositions [38,56-58].

#### 4.5 Silicon-29 NMR

Silicon-29 is a spin-1/2 nucleus with a 4.7% natural abundance and moderate resonance frequency (119 MHz at 14.1 T). Despite the low abundance,  $^{29}\text{Si}$  spectra are relatively simple to collect due to their narrow lines, however long relaxation times (hundreds to thousands of seconds) require lengthy experiments [59]. Paramagnetic oxides (e.g.  $\text{MnO}$ ,  $\text{Fe}_2\text{O}_3$ , and  $\text{Co}_3\text{O}_4$ ) are frequently added to silicate glasses (or are present as natural impurities in silicate minerals), where the fast relaxation of the coupled electrons facilitate drastically shorter  $^{29}\text{Si}$  relaxation (known as *paramagnetic relaxation enhancement*) [28,60]. Provided that only one paramagnetic

oxide is present, such sensitivity can be used to determine its concentration within the sample (e.g., glass; see Chapter 6, section 6.3.2).

$^{29}\text{Si}$  NMR is used to quantify structural units in glasses (for silicates, the  $Q^n$  notation is used, where  $n$  represents the number of bonding oxygen atoms around Si), although partial overlapping of multiple sites provides somewhat poor resolution and accurate spectral fitting requires that the positions of the  $Q^n$  sites are known. Several relationships between  $^{29}\text{Si}$  chemical shift and structural parameters have been established, including sensitivity to Si-O bond length and Si-O-Si bond angle [28]. In glasses, the distribution of bond lengths and angles diminish the impact of these relations, however a positive relationship to the number and identity of neighbouring cations has been observed [61,62]. Such relationships are easily noted in simple glass systems (e.g. binary or ternary silicates), however the multi-component nature of HLW glasses would complicate assignment of these trends.

# Addition of Transition Metals

## to Model HLW Glass

*The ubiquitous presence of paramagnetic transition metal oxides in HLW glasses creates potential issues for the successful implementation of NMR for their study. In order to assess the impact of these components, a variety of different paramagnetic oxides ( $\text{Cr}_2\text{O}_3$ ,  $\text{MnO}_2$ ,  $\text{Fe}_2\text{O}_3$ ,  $\text{NiO}$ , and  $\text{Nd}_2\text{O}_3$ ) were added individually to generate a series of sodium borosilicate glasses (also containing cesium and molybdenum). The paramagnetic components present in these glasses are analogised with diamagnetic components (using  $\text{La}_2\text{O}_3$  and  $\text{WO}_3$ ) and a control glass with no extra additives.  $^{133}\text{Cs}$ ,  $^{23}\text{Na}$ , and  $^{11}\text{B}$  NMR experiments were used to evaluate the viability of a typical NMR characterisation procedure.*

### 5.1 Glass Series Design

Model nuclear waste glasses designed for study by NMR spectroscopy have carefully avoided the inclusion of paramagnetic components to prevent undesirable broadening effects that obscure key information (e.g. accurate NMR peak integration). A number of studies have examined the redox state and spinel-forming ability of paramagnetic transition metal oxides in model waste glasses using XRD [63], XANES [64], and optical imaging [11,65], but dedicated studies of paramagnetic waste glasses by NMR spectroscopy have been limited [66,67]. For this reason, the glasses in this study have been designed to assess NMR spectral quality and changes to the glass system and/or phase-separated products with the addition of transition metal oxides. The

previously characterised five-component glass system ( $\text{Na}_2\text{O}-\text{B}_2\text{O}_3-\text{SiO}_2-\text{Cs}_2\text{O}-\text{MoO}_3$ ) [20] acts as a control for understanding any observable changes that occur from the addition of a sixth (and potentially paramagnetic) component ( $\text{Cr}_2\text{O}_3$ ,  $\text{MnO}_2$ ,  $\text{Fe}_2\text{O}_3$ ,  $\text{NiO}$ , or  $\text{Nd}_2\text{O}_3$ ). A glass prepared with diamagnetic  $\text{La}_2\text{O}_3$  is intended to serve as an analogue for the  $\text{Nd}_2\text{O}_3$  glass, both being lanthanide series elements with identical stable oxidation states ( $\text{La}^{3+}$ ,  $\text{Nd}^{3+}$ ) and nearly identical atomic radii (1.69 and 1.64 Å, respectively). Furthermore,  $\text{WO}_3$  is used to complement the other two Group VI components (i.e.,  $\text{MoO}_3$  and  $\text{Cr}_2\text{O}_3$ ), possessing the same stable oxidation state as molybdenum ( $\text{W}^{6+}/\text{Mo}^{6+}$ ) and the same atomic radius (1.30 Å). While molybdenum may exist in paramagnetic oxidation states (i.e.,  $\text{Mo}^{2+}$ ,  $\text{Mo}^{3+}$ ,  $\text{Mo}^{4+}$ , and  $\text{Mo}^{5+}$ ), its environment consists of either tetrahedral ( $\text{MoO}_4$ ) or octahedral ( $\text{MoO}_6$ ) units containing diamagnetic  $\text{Mo}^{6+}$  when solubilised in a glass network [50].

## 5.2 Experimental

### 5.2.1 Glass Synthesis

Sodium borosilicate glasses containing cesium, molybdenum, and a variable ‘additive oxide’ ( $\text{Cr}_2\text{O}_3$ ,  $\text{MnO}_2$ ,  $\text{Fe}_2\text{O}_3$ ,  $\text{NiO}$ ,  $\text{Nd}_2\text{O}_3$ ,  $\text{La}_2\text{O}_3$ , or  $\text{WO}_3$ ) were prepared by mixing precise quantities of the oxides or their respective carbonates in an agate mortar and pestle, followed by decarbonation in platinum crucibles at 600°C for 12 hours. The crucibles were then transferred to a high-temperature vertical-tube furnace and heated at 1300°C for one hour, then cooled at a rate of 60°C h<sup>-1</sup>. The “target” and “as-weighed” mol% compositions are listed in Table 5.1 and Table 5.2, respectively. Each paramagnetic oxide was added at similar mol% concentrations to those of the reference factory glasses (e.g., see Table 2.1, page 15), while those of  $\text{Cs}_2\text{O}$  and  $\text{MoO}_3$  were made higher to heighten crystallisation in the final product. Discrepancy between the  $\text{Cs}_2\text{O}$  levels of the target (2.50 mol%) and weighed (~3.50 mol%) was deliberate and necessary due to the

**Table 5.1.** Target compositions of six-component glasses (mol%)

Glass Sample	SiO <sub>2</sub>	B <sub>2</sub> O <sub>3</sub>	Na <sub>2</sub> O	Cs <sub>2</sub> O	MoO <sub>3</sub>	Additive
(1) Base	61.83	17.50	15.67	2.50	2.50	n/a
(2) Cr	61.69	17.45	15.64	2.50	2.50	0.22 Cr <sub>2</sub> O <sub>3</sub>
(3) Mn	61.65	17.44	15.63	2.50	2.50	0.28 MnO <sub>2</sub>
(4) Fe	61.05	17.25	15.48	2.50	2.50	1.22 Fe <sub>2</sub> O <sub>3</sub>
(5) Ni	61.60	17.42	15.61	2.50	2.50	0.37 NiO
(6) Nd	61.58	17.42	15.61	2.50	2.50	0.39 Nd <sub>2</sub> O <sub>3</sub>
(7) La	61.58	17.42	15.61	2.50	2.50	0.39 La <sub>2</sub> O <sub>3</sub>
(8) W	61.54	17.41	15.60	2.50	2.50	0.45 WO <sub>3</sub>

**Table 5.2.** Batch ('weighed') compositions of six-component glasses (mol%)

Glass Sample	SiO <sub>2</sub>	B <sub>2</sub> O <sub>3</sub>	Na <sub>2</sub> O <sup>a</sup>	Cs <sub>2</sub> O <sup>a</sup>	MoO <sub>3</sub>	Additive
(1) Base	61.18	17.34	15.51	3.49	2.48	n/a
(2) Cr	60.94	17.23	15.44	3.61	2.51	0.27 Cr <sub>2</sub> O <sub>3</sub>
(3) Mn	60.92	17.28	15.55	3.45	2.48	0.32 MnO <sub>2</sub>
(4) Fe	60.46	17.05	15.35	3.45	2.46	1.23 Fe <sub>2</sub> O <sub>3</sub>
(5) Ni	61.01	17.19	15.43	3.52	2.48	0.37 NiO
(6) Nd	60.85	17.24	15.56	3.44	2.51	0.40 Nd <sub>2</sub> O <sub>3</sub>
(7) La	60.99	17.29	15.45	3.41	2.48	0.38 La <sub>2</sub> O <sub>3</sub>
(8) W	60.85	17.27	15.47	3.42	2.48	0.51 WO <sub>3</sub>

<sup>a</sup> Na<sub>2</sub>CO<sub>3</sub> and Cs<sub>2</sub>CO<sub>3</sub> values have been converted to Na<sub>2</sub>O and Cs<sub>2</sub>O, respectively, for comparison purposes.



**Table 5.3.** Target and batch (‘weighed’) compositions of glass **9** (all additives) (mol%)

	<b>Target</b>	<b>Batch<sup>a</sup></b>
<b>SiO<sub>2</sub></b>	60.22	59.31
<b>B<sub>2</sub>O<sub>3</sub></b>	17.00	16.80
<b>Na<sub>2</sub>O</b>	15.30	15.05
<b>MoO<sub>3</sub></b>	2.50	2.45
<b>Cs<sub>2</sub>O</b>	2.50	3.75
<b>Fe<sub>2</sub>O<sub>3</sub></b>	1.22	1.23
<b>Nd<sub>2</sub>O<sub>3</sub></b>	0.39	0.42
<b>NiO</b>	0.37	0.43
<b>MnO<sub>2</sub></b>	0.28	0.33
<b>Cr<sub>2</sub>O<sub>3</sub></b>	0.22	0.22

<sup>a</sup> Na<sub>2</sub>CO<sub>3</sub> and Cs<sub>2</sub>CO<sub>3</sub> values have been converted to Na<sub>2</sub>O and Cs<sub>2</sub>O, respectively, for comparison purposes.

known volatilisation of this compound at our working temperature [68]. A final glass was prepared with all additives (“Glass 9”, Table 5.3, page 39) to observe their combined effect.

Following high-temperature treatment, crystalline deposits were observed across the glass surface, indicating the occurrence of phase separation. Additionally, the glasses were easily distinguished by their colour: Cr-glass (green), Mn-glass (purple), Fe-glass (brown), and Ni-glass (light blue). The colour is attributed to the added transition metals, where *d-d* electronic transitions in the visible region of the electromagnetic spectrum are linked to particular metal oxidation state and coordination [69-71]. For example, glasses containing Ni can appear blue, brown, or green in colour according to the presence of tetrahedral, trigonal bipyramidal, and octahedral Ni units, respectively [69]. Similarly, the absorption profiles for different oxidation states of chromium ( $\text{Cr}^{3+}$  and  $\text{Cr}^{6+}$ ) and manganese ( $\text{Mn}^{2+}$ ,  $\text{Mn}^{3+}$ , and  $\text{Mn}^{4+}$ ) impart characteristic colouration to the host glass [70,71].

### 5.2.2 Nuclear Magnetic Resonance Spectroscopy

NMR experiments were conducted on a Varian <sup>Unity</sup>Inova 600 ( $B_0 = 14.1$  T) spectrometer using Varian-Chemmagetics MAS probes. The glass samples were powdered using an agate mortar and pestle and packed into zirconium oxide ( $\text{ZrO}_2$ ) MAS rotors.

$^{133}\text{Cs}$  MAS NMR spectra of all glasses were collected on a 1.6 mm triple-resonance MAS probe at a spinning rate of 30 kHz using single-pulse experiments ( $0.8\ \mu\text{s}$ ,  $\sim 20^\circ$  tip angle,  $\nu_{\text{rf}} = 71$  kHz) with a 70 s recycle delay and between 1024 and 4096 co-added transients. Sample masses between 10 and 13 mg were packed into 1.6 mm  $\text{ZrO}_2$  rotors. Pulse calibration and spectral referencing used an aqueous solution of cesium chloride (0.1 M  $\text{CsCl}$ , 0 ppm).

$^{23}\text{Na}$  MAS NMR spectra of four glasses (**1**, **2**, **4**, and **5**) were collected on a 3.2 mm double-resonance MAS probe at spinning rates between 15 and 18 kHz using single-pulse experiments ( $0.3\ \mu\text{s}$ ,  $\sim 15^\circ$  tip angle,  $\nu_{\text{rf}} = 71$  kHz) with an optimised recycle delay of 1 s and

between 256 and 4096 co-added transients. Sample masses between 33 and 35 mg were packed into 3.2 mm ZrO<sub>2</sub> rotors. Pulse calibration and spectral referencing used an aqueous solution of sodium chloride (1 M NaCl, 0 ppm).

<sup>11</sup>B MAS NMR spectra of all glasses were collected on 3.2 mm triple-resonance MAS probe at spinning rate of 10 kHz using single-pulse experiments (0.28  $\mu$ s,  $\sim 15^\circ$  tip angle,  $\nu_{rf} = 74$  kHz) with an optimised recycle delay of 1 s and 128 co-added transients. Sample masses between 30 and 35 mg were packed into 3.2 mm ZrO<sub>2</sub> rotors. Pulse calibration and spectral referencing used an aqueous solution of boric acid (0.1 M B(OH)<sub>3</sub>, 19.6 ppm).

Spectral simulations and integrations for <sup>133</sup>Cs MAS NMR data were conducted by combination Gaussian/Lorentzian lineshape fitting using SpinWorks software [72], while those of <sup>23</sup>Na and <sup>11</sup>B were completed using a quadrupolar shape-fitting module in DMFit software [73]. Error estimates for the simulated spectra were based on multiple fits or fit adjustments.

## 5.3 Results and Discussion

### 5.3.1 <sup>133</sup>Cs MAS NMR

Figure 5.1 shows the <sup>133</sup>Cs MAS NMR spectrum of the five-component base glass, along with an example of the typical peak-fitting simulation that was used for all spectra. The glassy site is well modelled by a Gaussian peak, reflecting the distribution of Cs<sup>+</sup> environments encountered throughout the network. The two predominant crystalline sites, CsNaMoO<sub>4</sub>•2H<sub>2</sub>O (-71 ppm) and Cs<sub>3</sub>Na(MoO<sub>4</sub>)<sub>2</sub> (161 & -145 ppm), have been previously characterised [20] and are fit using narrow Lorentzian or Gaussian-Lorentzian peaks. The first set of spinning sidebands for the glassy site and CsNaMoO<sub>4</sub>•2H<sub>2</sub>O are easily observed and simulated accordingly.

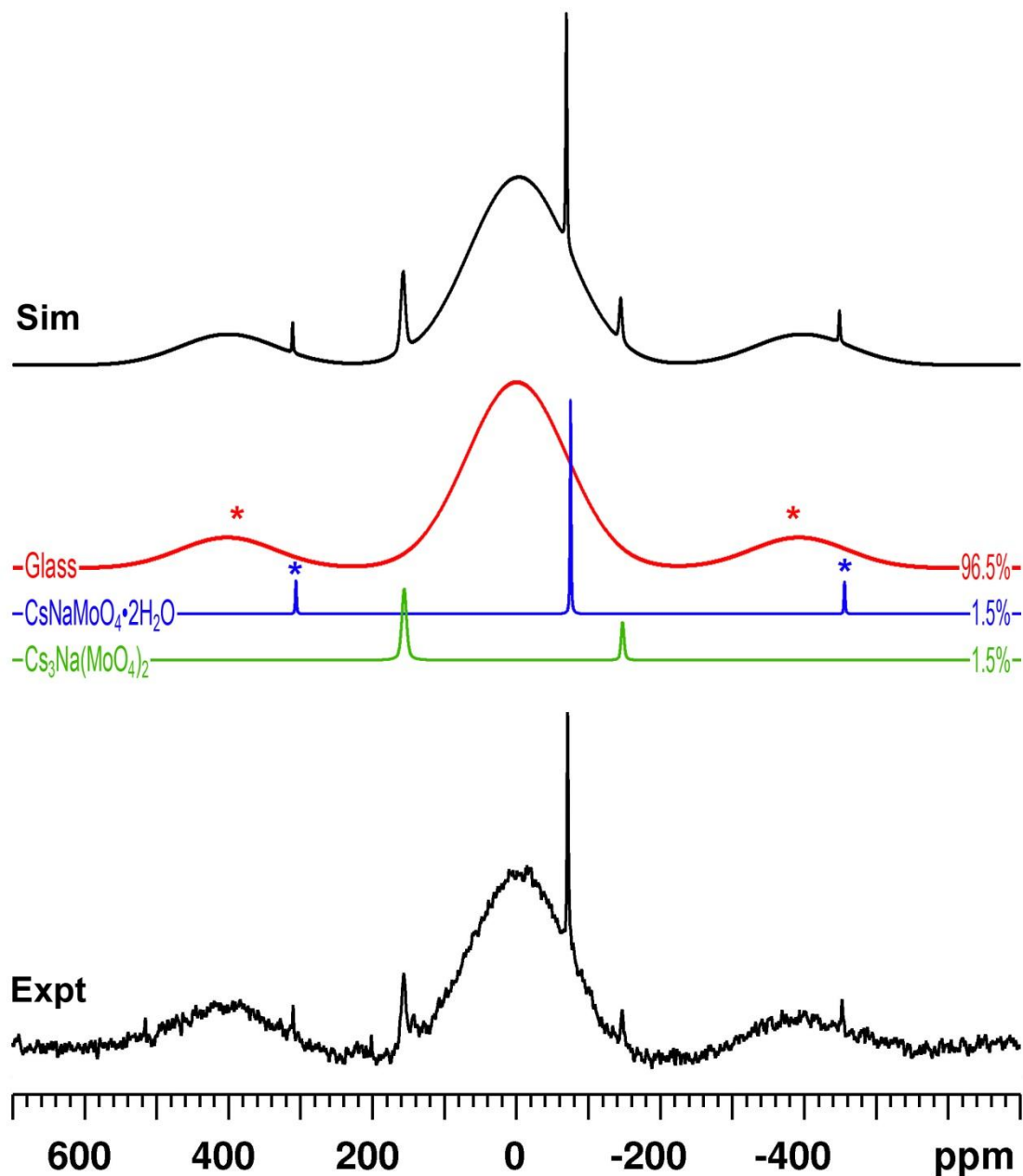


**Figure 5.1.** Experimental  $^{133}\text{Cs}$  MAS NMR spectrum of the five-component base glass, with overall simulation and deconvolution of known sites; Cs in glassy environments (red),  $\text{CsNaMoO}_4 \cdot 2\text{H}_2\text{O}$  (blue), and  $\text{Cs}_3\text{Na}(\text{MoO}_4)_2$  (two crystallographically distinct sites) (green). Spinning sidebands are denoted with an asterisk. Integrated intensities are noted, where the residual 0.5% is attributed to unknown crystalline sites (see text).

The  $^{133}\text{Cs}$  MAS NMR spectra of all eight glass samples are depicted in Figure 5.2, where it is clear that  $\text{CsNaMoO}_4 \cdot 2\text{H}_2\text{O}$  and  $\text{Cs}_3\text{Na}(\text{MoO}_4)_2$  are, not unexpectedly, the most consistently observed phases. Another common Cs-bearing phase observed in systems of this type is  $\text{Cs}_2\text{MoO}_4$  (55 & -16 ppm) [20], although its presence was not detected here. Similarly, the addition of  $\text{Cr}_2\text{O}_3$  and  $\text{WO}_3$  might enable formation of  $\text{Cs}_2\text{CrO}_4$  (26 & -100 ppm) [37] and  $\text{Cs}_2\text{WO}_4$  (-163 & -222 ppm) [74] as crystalline products for the Cr- and W-containing glasses, respectively, although no evidence of either was observed. Instead, there are several low-intensity crystalline peaks of unknown origin in the region between 25 and -40 ppm (e.g. glass **1** (base), glass **2** (Cr), glass **7** (La), and glass **8** (W)), however their inconsistency across multiple samples excludes assignment as a single unknown phase.

Integrated intensities of the  $^{133}\text{Cs}$  NMR spectra (Table 5.4) show a range between 0% (glass **7**) and 9.6% (glass **4**) crystallisation of Cs-bearing phases (i.e., 100% to 90.4%  $\text{Cs}^+$  in vitreous environments). With only one synthesised trial of each glass, it is unclear whether the changes in the degree of crystallinity can be linked to the additives, however it appears that the majority of the added transition metal oxides have been accommodated by the glass network.

Finally, no obvious paramagnetic influence was observed in  $^{133}\text{Cs}$  MAS NMR of glasses **2-6**. The full-width-at-half-maximum (FWHM) values for the glassy site of each sample have been noted in Figure 5.2, and show no appreciable deviation to higher values outside a range from 12.0 to 13.0 kHz (where the base glass FWHM is 12.8 kHz). Further experiments using variable recycle delays indicated no obvious increase in the relaxation rate of either glass or crystalline sites for samples that contain paramagnetic additives.

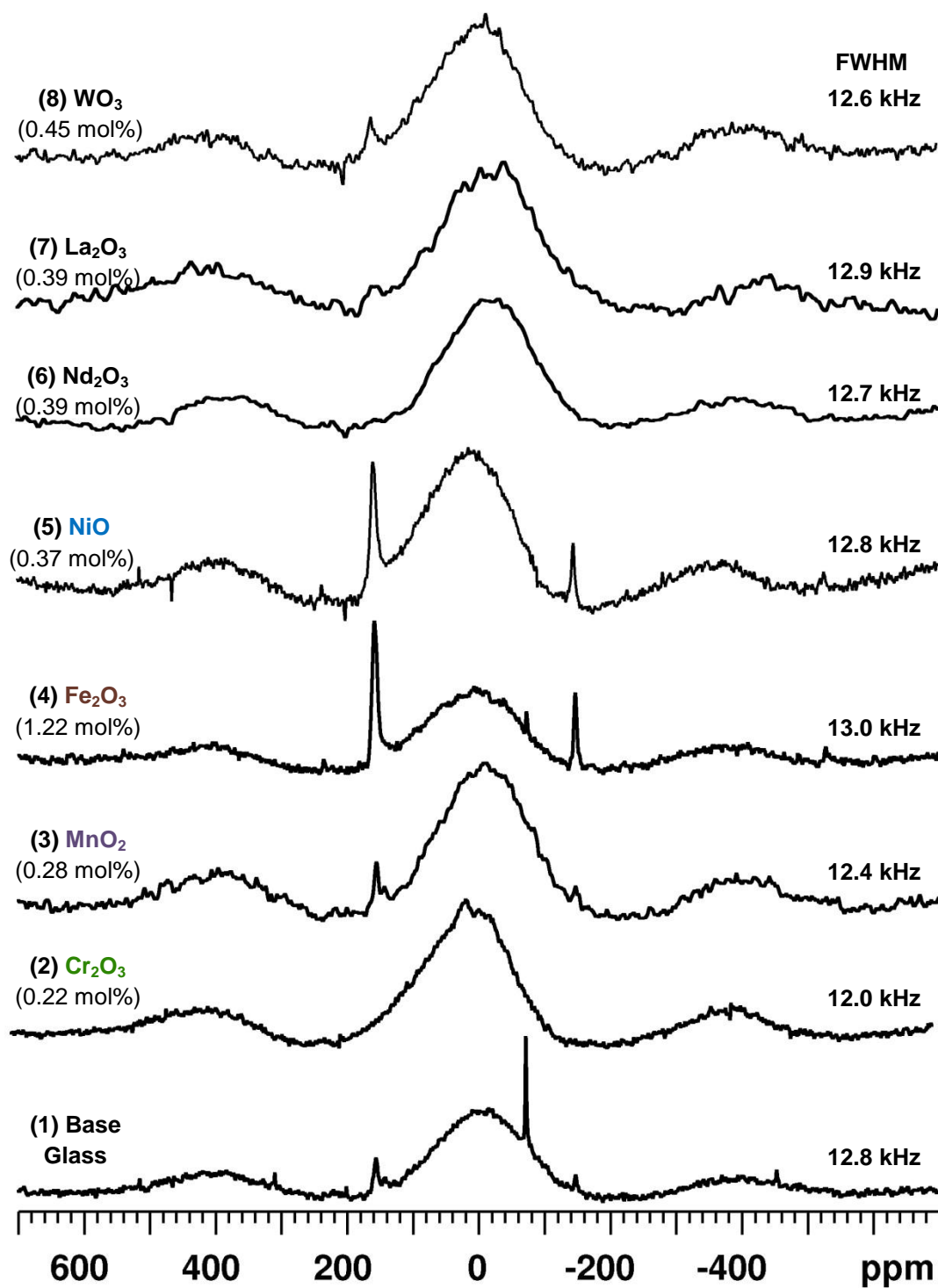


**Figure 5.2.** Experimental  $^{133}\text{Cs}$  MAS NMR spectra of the five-component base glass and six-component glasses with paramagnetic or diamagnetic additives (indicated above using target concentrations). The respective FWHM value of the glassy site (error of  $\pm 0.3$  kHz) is indicated on the right side of the spectrum.

**Table 5.4.** Integrated intensities (%) for  $^{133}\text{Cs}$  MAS NMR of glasses **1-8**

Glass Sample	Component			
	Glass	$\text{CsNaMoO}_4 \cdot 2\text{H}_2\text{O}$	$\text{Cs}_3\text{Na}(\text{MoO}_4)_2$	Unknown
<b>(1) Base</b>	96.5	1.5	1.5	0.5
	$\pm 0.3$	$\pm 0.1$	$\pm 0.1$	$\pm 0.1$
<b>(2) Cr</b>	98.8	-	-	1.2
	$\pm 0.4$	-	-	$\pm 0.4$
<b>(3) Mn</b>	98.3	-	1.4	0.3
	$\pm 0.3$	-	$\pm 0.2$	$\pm 0.1$
<b>(4) Fe</b>	90.4	0.3	8.2	1.2
	$\pm 1.6$	$\pm 0.1$	$\pm 1.3$	$\pm 0.2$
<b>(5) Ni</b>	95.0	-	4.9	$< 0.1$
	$\pm 0.6$	-	$\pm 0.6$	( $\pm 0.1$ )
<b>(6) Nd</b>	100	-	-	-
	-	-	-	-
<b>(7) La</b>	98.3	-	1.2	0.5
	$\pm 0.7$	-	$\pm 0.4$	$\pm 0.3$
<b>(8) W</b>	98.4	-	0.8	0.8
	$\pm 0.5$	-	$\pm 0.3$	$\pm 0.2$

### 5.3.2 $^{23}\text{Na}$ MAS NMR

Based on the  $^{133}\text{Cs}$  MAS NMR results, glasses **4** (Fe) and **5** (Ni) produced the highest degree of crystallisation of Cs-bearing compounds (particularly of  $\text{Cs}_3\text{Na}(\text{MoO}_4)_2$ ), and were thus investigated by  $^{23}\text{Na}$  MAS NMR along with glasses **1** (base glass; as a control) and **2** (Cr; lowest FWHM and highest integrated intensity for unknown Cs crystalline sites). The  $^{23}\text{Na}$  MAS NMR spectrum of the five-component base glass is shown in Figure 5.3 along with a simulation and deconvolution of its sites; the experimental and simulated spectra for all four selected glasses are displayed in Figure 5.4. The glassy components of the  $^{23}\text{Na}$  MAS NMR spectra were fit using Gaussian or Gaussian-Lorentzian lineshapes (as in  $^{133}\text{Cs}$  NMR). As described in Chapter 4, the unique quadrupolar shapes of crystalline Na-bearing compounds must be carefully parameterised to allow valid deconvolution estimates in highly heterogeneous systems (such as our model waste glasses). Table 5.5 summarises the NMR parameters of the compounds that were observed (and were necessary to achieve simulation of the observed lineshape) in the  $^{23}\text{Na}$  NMR spectra of the selected glasses. At a field strength of 14.1 T, the single peak of  $\text{CsNaMoO}_4$  ( $C_Q = 1.33$  MHz,  $\eta = 1$ ,  $\delta_{\text{iso}} = -0.4$  ppm) [20] appears between the discontinuities of  $\text{Na}_2\text{MoO}_4$  ( $C_Q = 2.59$  MHz,  $\eta = 0$ ,  $\delta_{\text{iso}} = -3.2$  ppm) [75] (see Figure 5.3), while  $\text{Cs}_3\text{Na}(\text{MoO}_4)_2$  ( $C_Q = 0.7$  MHz,  $\eta = 0$ ,  $\delta_{\text{iso}} = -11.8$  ppm) [20] appears just at the foot of the  $\text{Na}_2\text{MoO}_4$  pattern.

In glasses **2** (Cr), **4** (Fe), and **5** (Ni) it was necessary to include hydrated sodium molybdate ( $\text{Na}_2\text{MoO}_4 \cdot 2\text{H}_2\text{O}$ ) in the simulation to account for an appreciable amount of the signal.  $\text{Na}_2\text{MoO}_4 \cdot 2\text{H}_2\text{O}$  contains two unique sites; Na(1) with  $C_Q = 0.875$  MHz,  $\eta = 0.23$ ,  $\delta_{\text{iso}} = -1.4$  ppm, and Na(2) with  $C_Q = 2.69$  MHz,  $\eta = 0.08$ ,  $\delta_{\text{iso}} = 4.0$  ppm [75]. Given the similarity between the  $^{23}\text{Na}$  NMR parameters of  $\text{Na}_2\text{MoO}_4$  (anhydrous) and Na(2) of  $\text{Na}_2\text{MoO}_4 \cdot 2\text{H}_2\text{O}$ , the presence of hydrated sodium molybdate (in a one-dimensional  $^{23}\text{Na}$  NMR spectrum) is most easily identified by the presence of the narrower Na(1) site, although it overlap partially with that



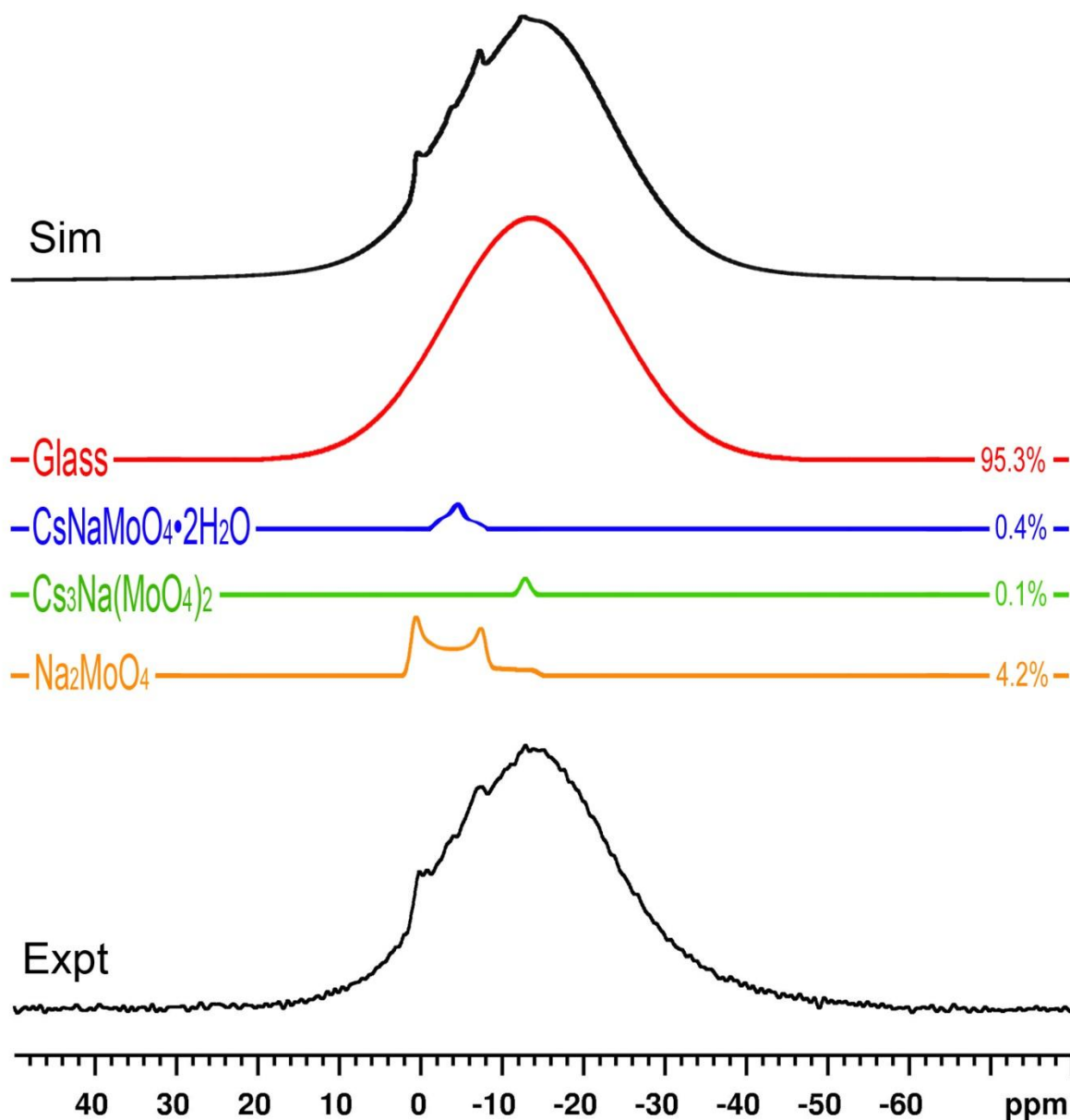


**Figure 5.3.** Experimental  $^{23}\text{Na}$  MAS NMR spectrum of the five-component base glass, with overall simulation and deconvolution of known sites; Na in glassy environments (red),  $\text{CsNaMoO}_4 \cdot 2\text{H}_2\text{O}$  (blue),  $\text{Cs}_3\text{Na}(\text{MoO}_4)_2$  (green), and  $\text{Na}_2\text{MoO}_4$  (orange). Integrated intensities are noted on the right.

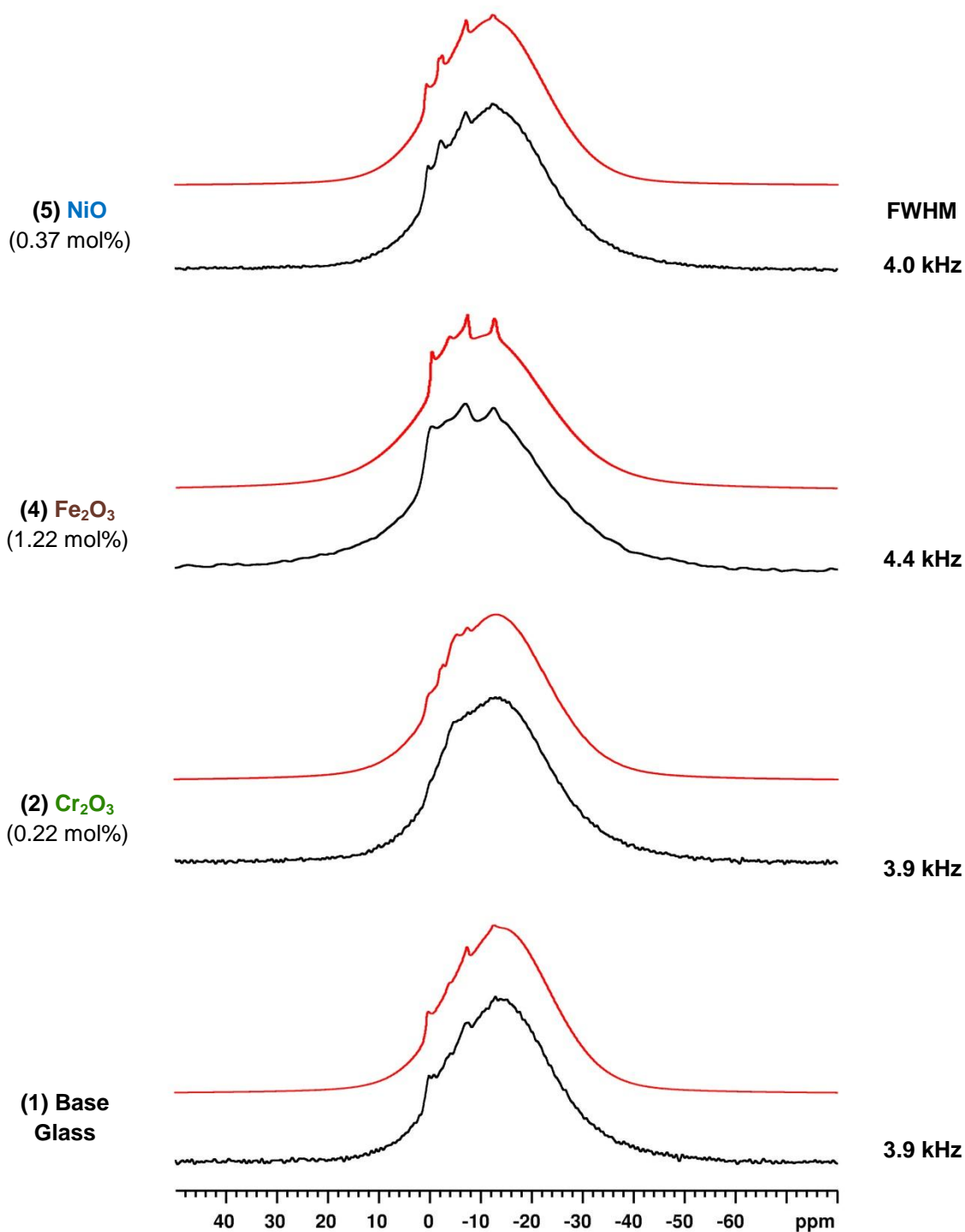


**Figure 5.4.** Experimental  $^{23}\text{Na}$  MAS NMR spectra of selected glasses (black line) with best-fit simulated spectra (red line); see Tables 5.5 and 5.6 for fit details. The respective FWHM of the glassy site (error of  $\pm 0.1$  kHz) is indicated on the right side of the experimental spectrum.

**Table 5.5.**  $^{23}\text{Na}$  NMR parameters of relevant sodium-bearing compounds

Site	$C_Q$ (MHz)	$\eta$	$\delta_{\text{iso}}$ (ppm)	Reference
<b><math>\text{Na}_2\text{MoO}_4</math></b>	2.59	0	3.2	[75]
<b><math>\text{Na}_2\text{MoO}_4 \cdot 2\text{H}_2\text{O}</math></b>				
Na(1)	0.875	0.23	-1.4	[75]
Na(2)	2.69	0.09	4.0	
<b><math>\text{CsNaMoO}_4 \cdot 2\text{H}_2\text{O}</math></b>	1.33	1	-0.4	[20]
<b><math>\text{Cs}_3\text{Na}(\text{MoO}_4)_2</math></b>	0.7	0	-11.8	[20]
<b>Unknown<sup>a</sup></b>	$\sim 1.4$	$\sim 0.5$	-5.0	n/a

<sup>a</sup> The parameters were chosen to reflect a moderate  $C_Q$  and  $\eta$  for modelling intensity in the area around -5 ppm. This site was only used in the simulation of glass **2** (Cr), as some (presumed) crystalline intensity was unaccounted for.

**Table 5.6.** Integrated intensities (%) for  $^{23}\text{Na}$  MAS NMR of selected glasses

Glass Sample	Component					
	Glass	$\text{Na}_2\text{MoO}_4$	$\text{Na}_2\text{MoO}_4 \cdot 2\text{H}_2\text{O}$	$\text{CsNaMoO}_4 \cdot 2\text{H}_2\text{O}$	$\text{Cs}_3\text{Na}(\text{MoO}_4)_2$	Unknown
<b>(1) Base</b>	95.3	4.2	-	0.4	0.1	-
	$\pm 0.8$	$\pm 0.6$	-	$\pm 0.1$	$\pm 0.1$	-
<b>(2) Cr</b>	95.6	2.6	0.6	-	-	1.2
	$\pm 0.5$	$\pm 0.2$	$\pm 0.1$	-	-	$\pm 0.2$
<b>(4) Fe</b>	94.1	4.4	0.3	0.7	0.5	-
	$\pm 1.0$	$\pm 0.4$	$\pm 0.3$	$\pm 0.2$	$\pm 0.1$	-
<b>(5) Ni</b>	95.1	3.5	1.3	-	0.1	-
	$\pm 0.5$	$\pm 0.2$	$\pm 0.2$	-	$\pm 0.1$	-

of  $\text{CsNaMoO}_4 \cdot 2\text{H}_2\text{O}$ . For this reason, the error bounds in the  $^{23}\text{Na}$  NMR integrated intensities (Table 5.6) are wider than those encountered for  $^{133}\text{Cs}$  NMR results, nevertheless they provide additional insight on hydration of the phase-separated products. Furthermore, the substantial intensity differences between sodium molybdate (3 to 4.5%; both hydrous and anhydrous) and those of the cesium-sodium molybdates (collectively 0.1 to 1.2%) signifies that  $\text{Na}^+$  is the dominant coupling cation for  $\text{MoO}_4^{2-}$  species during phase separation (versus  $\text{Cs}^+$ ), attributed to the higher abundance of sodium in these compositions.

The FWHM for each glassy site is noted in Figure 5.4, where a slight broadening is observed with increased additive concentration; from  $3.9 \pm 0.1$  kHz for glass **1** (base) to  $4.4 \pm 0.1$  kHz for glass **4** (Fe). The increase is subtle, but may reflect more  $\text{Na}^+$  cations closer to paramagnetic centres than  $\text{Cs}^+$ . The sensitivity is only significant for the sample with the highest concentration of additive, 1.22 mol%  $\text{Fe}_2\text{O}_3$ , which far exceeds the factory standard levels of the other paramagnetic additives (0.2 to 0.4 mol%). Additionally, there was no detectable relaxation enhancement for the glassy sodium sites with respect to the five-component base glass (tested with recycle delays down to 0.5 s). The glassy site of the five-component (non-paramagnetic) glass could be easily collected with a recycle delay of 1 s (using a  $15^\circ$  pulse), and a simple recycle delay test would exceed the probe duty cycle before revealing paramagnetic relaxation enhancement in the remaining samples.

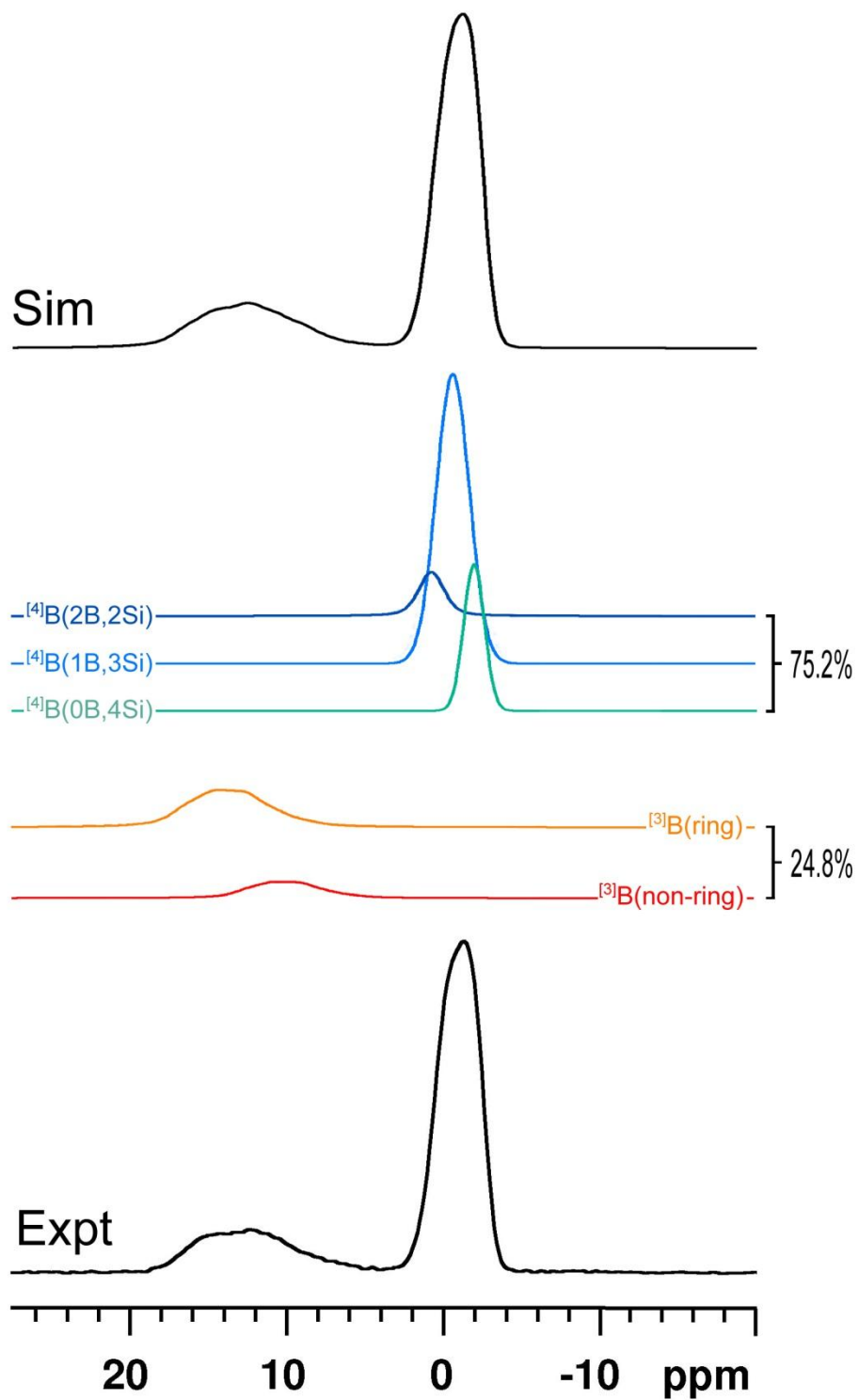
### 5.3.3 $^{11}\text{B}$ MAS NMR

Figure 5.5 shows the experimental and simulated spectrum (central transition portion) of the five-component base glass, including subspectra depicting the individual species that comprise both the  $^{13}\text{B}$  and  $^{14}\text{B}$  sites. The two regions have been fit according to  $^{11}\text{B}$  NMR parameters of similar glass compositions found in the literature [56,76,77] with ring and non-ring forms of

BO<sub>3</sub> comprising <sup>13</sup>B, and various BO<sub>4</sub> tetrahedra comprising <sup>14</sup>B (i.e., <sup>14</sup>B(2B,2Si), <sup>14</sup>B(1B,3Si), and <sup>14</sup>B(0B,4Si) separated by about 2 ppm).

The experimental <sup>11</sup>B MAS NMR spectra of glasses **1-8** are shown in Figure 5.6, where it is seen that the level and identity of paramagnetic additive impacts the breadth of both the <sup>13</sup>B and <sup>14</sup>B regions. As expressed by the FWHM values listed in Table 5.7, the breadth of <sup>13</sup>B increases from 1490 Hz (base glass) to 2880 Hz (glass **4** (Fe)), while <sup>14</sup>B increases from 615 Hz (base glass) to 1590 Hz (glass **4** (Fe)). The FWHM values of the diamagnetic glasses are consistent with the five-component base glass, and confirm that the broadening exhibited by the remaining samples is wholly attributed to the paramagnetic interaction. To enable a balanced comparison, the FWHM values have been plotted against 2S•mol% (Figure 5.7), a parameter that incorporates both the electron count and the additive concentration, where mol% has been corrected for the stoichiometry of Cr<sub>2</sub>O<sub>3</sub>, Fe<sub>2</sub>O<sub>3</sub>, and Nd<sub>2</sub>O<sub>3</sub>. The best-fit line indicates the expected positive trend between mol% of unpaired electrons and <sup>11</sup>B spectral breadth, however it is clear that experiments on glasses with 2S•mol% values in the intermediate region of the plots would assist in establishing this relationship. The FWHM values for Mn<sup>4+</sup> (S=3/2 (*d*<sup>3</sup>), 0.28 mol% MnO<sub>2</sub>) are noticeably broader than would be predicted by the trend, however the fit is improved if Mn<sup>2+</sup> (S=5/2, *d*<sup>5</sup>) is used. This model assumes only the common oxidation state for each additive, however it is possible that each may exist in multiple oxidation states, such as Cr<sup>3+</sup>/Cr<sup>6+</sup> and Fe<sup>2+</sup>/Fe<sup>3+</sup>.

The integrated intensities of the <sup>13</sup>B and <sup>14</sup>B regions are listed in Table 5.7. Since the individual sub-sites of each <sup>13</sup>B and <sup>14</sup>B are not fully resolved (in one dimension), the integrations are not considered beyond the distinction of <sup>13</sup>B and <sup>14</sup>B. Nevertheless, there are no significant deviations outside a range of 25.3 ± 1.7% for <sup>13</sup>B and 74.7 ± 1.7% for <sup>14</sup>B, which are



**Figure 5.5.** Experimental  $^{11}\text{B}$  MAS NMR spectrum of the five-component base glass, with overall simulation and deconvolution of glassy sites (as noted). The integrations are taken as the total of  $^{13}\text{B}$  and  $^{14}\text{B}$  peaks since the individual sites are not fully resolved (see text).

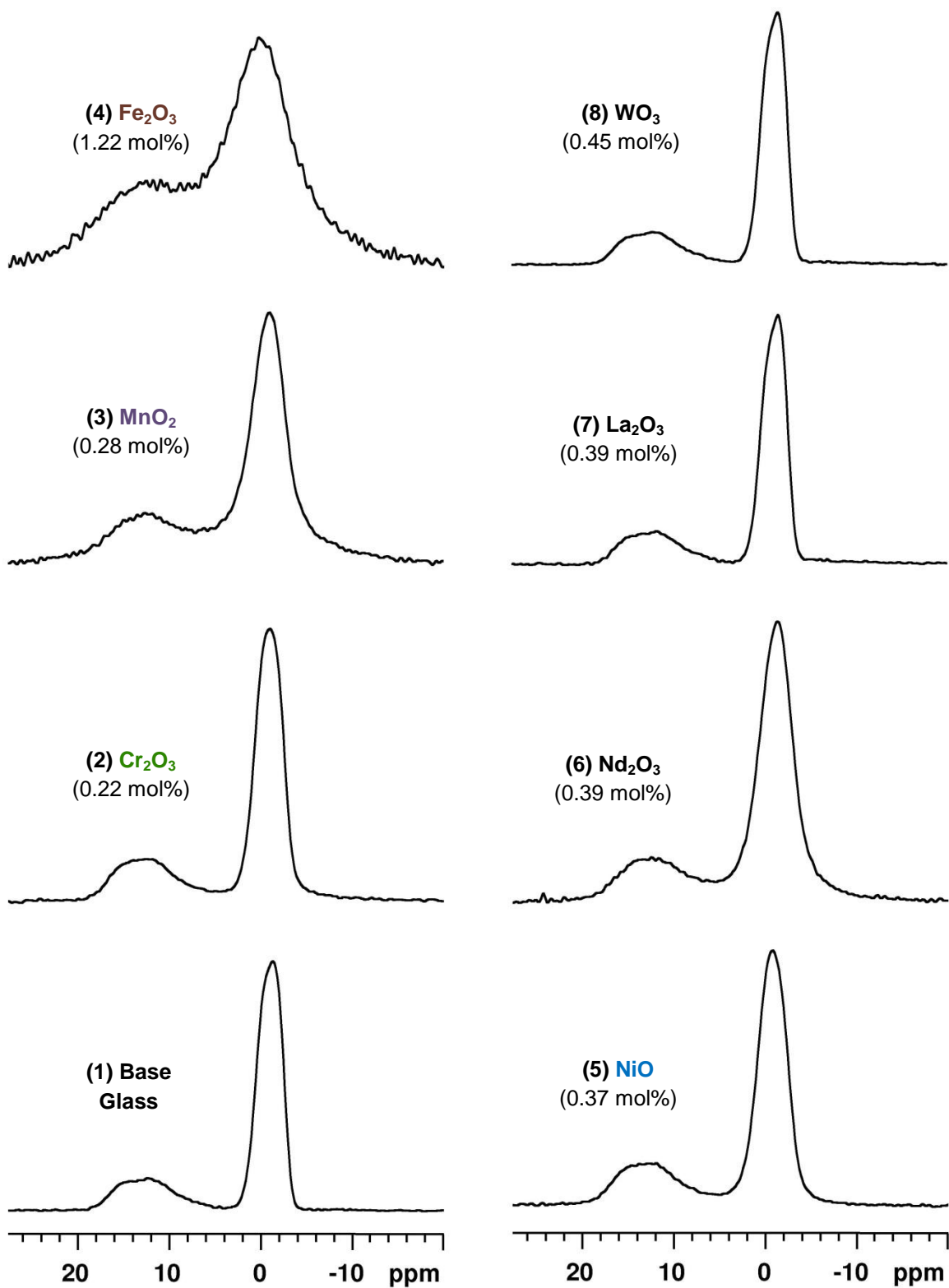


**Figure 5.6.** Experimental  $^{11}\text{B}$  MAS NMR spectra of five-component base glass and six-component glasses with paramagnetic or diamagnetic additive (indicated above using target concentrations).

**Table 5.7.** FWHM values and integrated intensities (%) for  $^{11}\text{B}$  MAS NMR of glasses **1-8**

Glass Sample	FWHM (Hz)		Integration (%) <sup>a</sup>	
	$^{[3]}\text{B}$	$^{[4]}\text{B}$	$^{[3]}\text{B}$	$^{[4]}\text{B}$
<b>(1) Base</b>	1490 $\pm 50$	615 $\pm 10$	24.8	75.2
<b>(2) Cr</b>	1590 $\pm 50$	670 $\pm 10$	26.4	73.6
<b>(3) Mn</b>	2270 $\pm 60$	830 $\pm 10$	24.5	75.5
<b>(4) Fe</b>	2880 $\pm 180$	1590 $\pm 20$	27.0	73.0
<b>(5) Ni</b>	1580 $\pm 50$	710 $\pm 10$	25.9	74.1
<b>(6) Nd</b>	1960 $\pm 80$	800 $\pm 10$	21.6	78.4
<b>(7) La</b>	1490 $\pm 50$	610 $\pm 10$	26.3	73.7
<b>(8) W</b>	1500 $\pm 50$	610 $\pm 10$	25.4	74.6

<sup>a</sup> Error in integration is less than  $\pm 2.0\%$



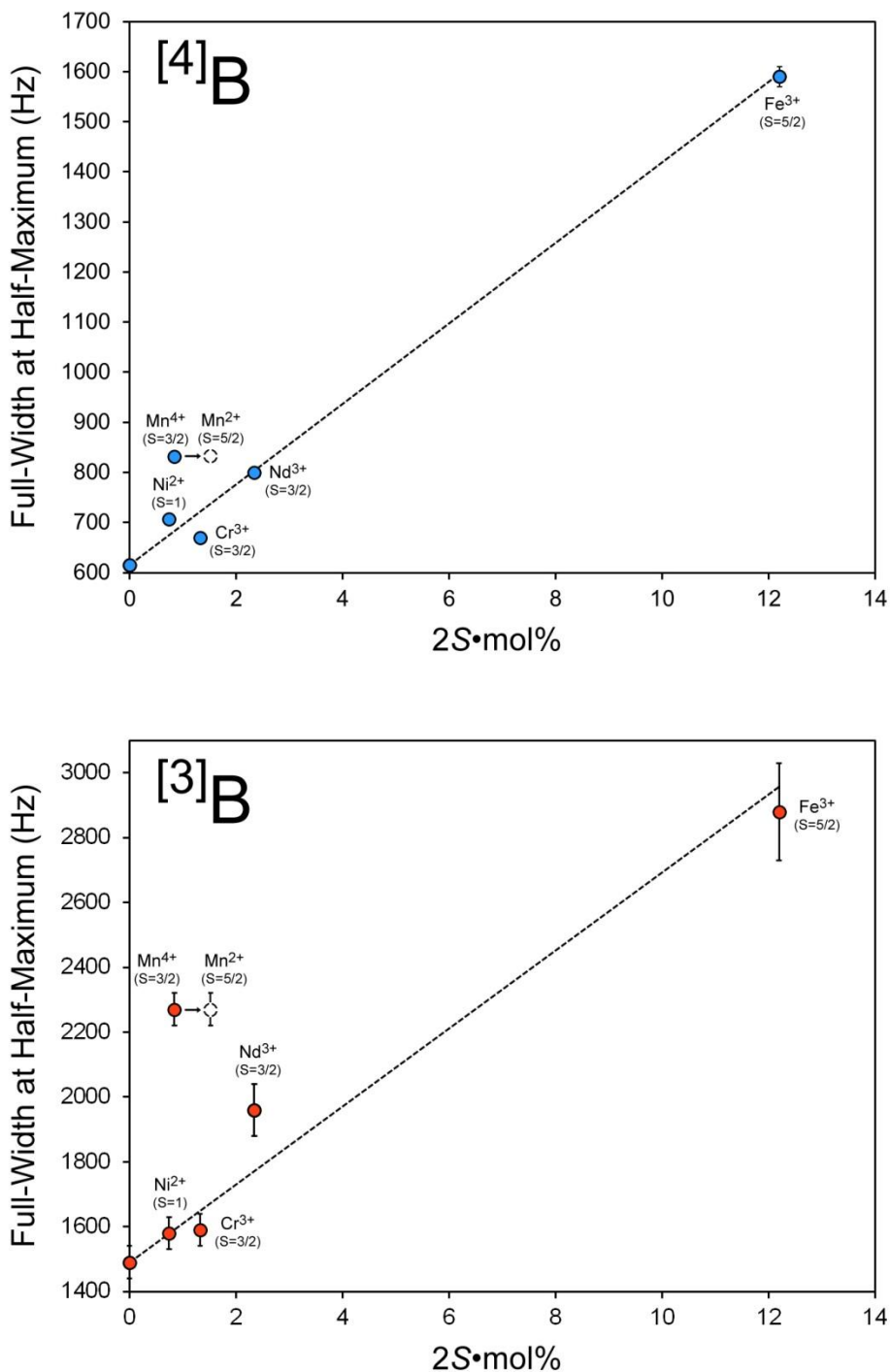


**Figure 5.7.** FWHM values for <sup>[3]</sup>B (lower) and <sup>[4]</sup>B (upper) as a function of paramagnetic content, expressed as the product of unpaired electron number ( $S$ ) and target mol% (corrected for stoichiometry, e.g. 0.22 mol% of  $\text{Cr}_2\text{O}_3$  is 0.44 mol%  $\text{Cr}^{3+}$ ). For each, the point near the origin is the five-component base glass. The position of glass **3** assuming  $\text{Mn}^{2+}$  has been noted.

expected occupancies for compositions with these levels of  $\text{Na}_2\text{O}/\text{B}_2\text{O}_3$  ( $R=0.9$ ) and  $\text{SiO}_2/\text{B}_2\text{O}_3$  ( $K=3.5$ ) [77]. Given the slight variances in the diamagnetic analogue glasses (**7** and **8**), it would appear that the network-modifying character of these additives has a stronger impact on the  $^{13}\text{B}$  and  $^{14}\text{B}$  integrations than does the paramagnetic interaction (i.e., preferential signal alteration), however the broadening encountered at higher loadings (e.g. glass **4** (Fe)) adds another level of complexity and uncertainty to spectral fitting and integration.

### 5.3.4 NMR of a Complex Model HLW Glass

Glass **9** was synthesised to explore the combined effect of all the paramagnetic additives on NMR spectral quality and interpretability.  $^{133}\text{Cs}$  MAS NMR (Figure 5.8) shows that the glassy  $\text{Cs}^+$  signal is easily obtained with short recycle delays ( $d1 = 0.5$  s), while the crystalline sites still require longer recycle delays ( $d1 = 60$  s or greater). The only crystalline signal that is easily identified is  $\text{CsNaMoO}_4 \cdot 2\text{H}_2\text{O}$  at  $-71$  ppm, although it appears that other peaks exist in the region between  $40$  and  $-40$  ppm.

The  $^{23}\text{Na}$  MAS NMR spectrum of glass **9** is shown in Figure 5.9 (page 58), where the presence of  $\text{Na}_2\text{MoO}_4 \cdot 2\text{H}_2\text{O}$  is noted by the strong signal around  $-2$  ppm, corresponding to the Na(1) site (see Table 5.5, page 49). The presence of a stronger paramagnetic interaction (than has been shown previously) is noticeable by the breadth of the glassy  $\text{Na}^+$  site, which also shows a distinct tailing toward the low frequency region that indicates a distribution of  $C_Q$  values. A better example of this change in peak shape is detailed in Chapter 7 (section 7.3.2, page 114).

The  $^{11}\text{B}$  MAS NMR spectrum of glass **9** is shown in Figure 5.10 (page 58). As would be expected, the presence of all additives produces  $^{13}\text{B}$  and  $^{14}\text{B}$  peaks that are broader ( $3200 \pm 200$  Hz and  $2250 \pm 50$  Hz, respectively) than those of any individual additive. These FWHM values are consistent with the trends in Figure 5.7 (combined  $2S \cdot \text{mol}\% = 18$  for glass **9**, see Figures 7.5 (page 122) and 7.6 (page 124) for the complete  $^{11}\text{B}$  NMR broadening dataset from this thesis.

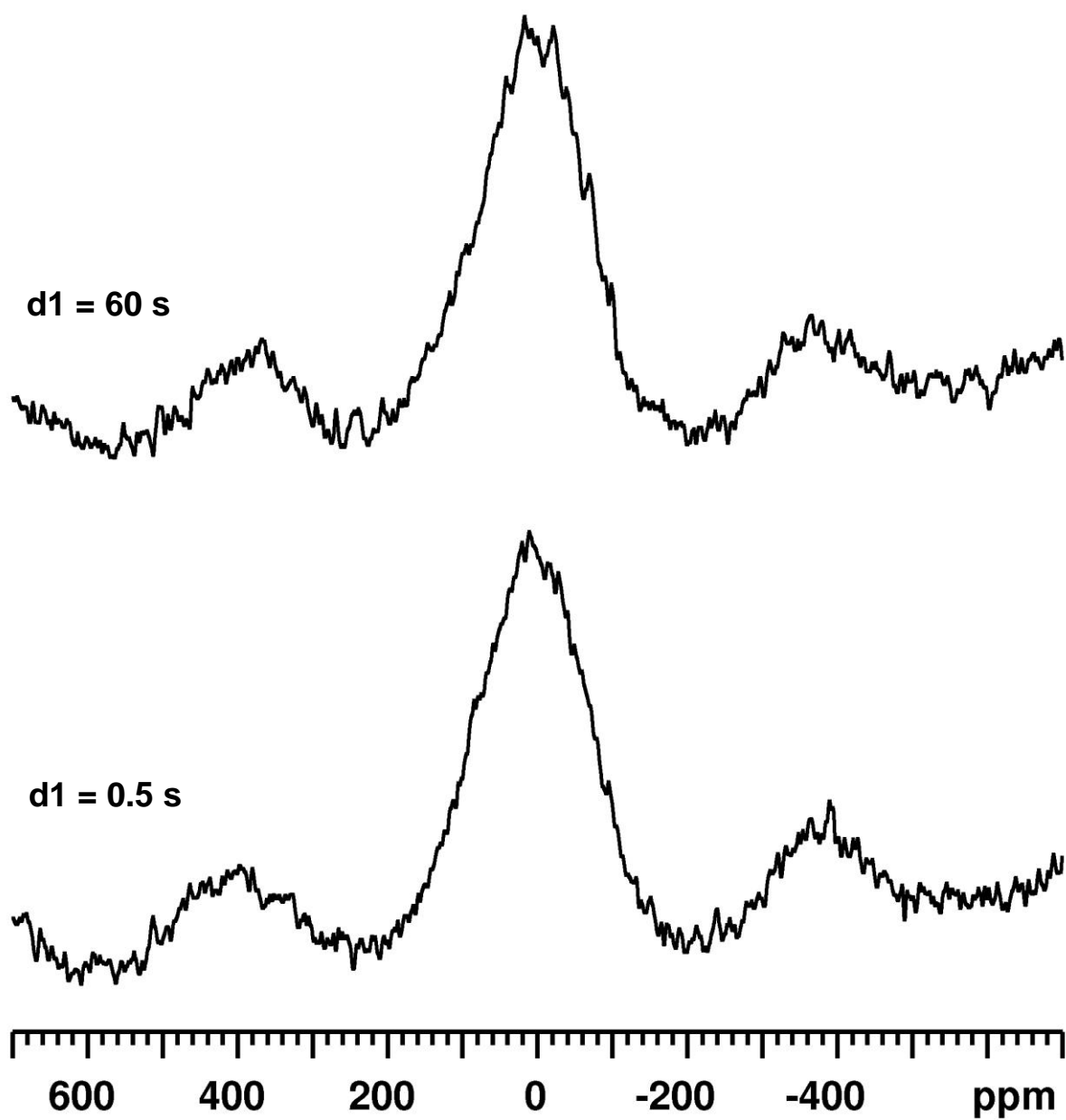


**Figure 5.8.** Experimental  $^{133}\text{Cs}$  MAS NMR spectra of glass **9** (all paramagnetic additives), collected with a recycle delay ( $d1$ ) of 0.5 s (lower) and 60 s (upper).

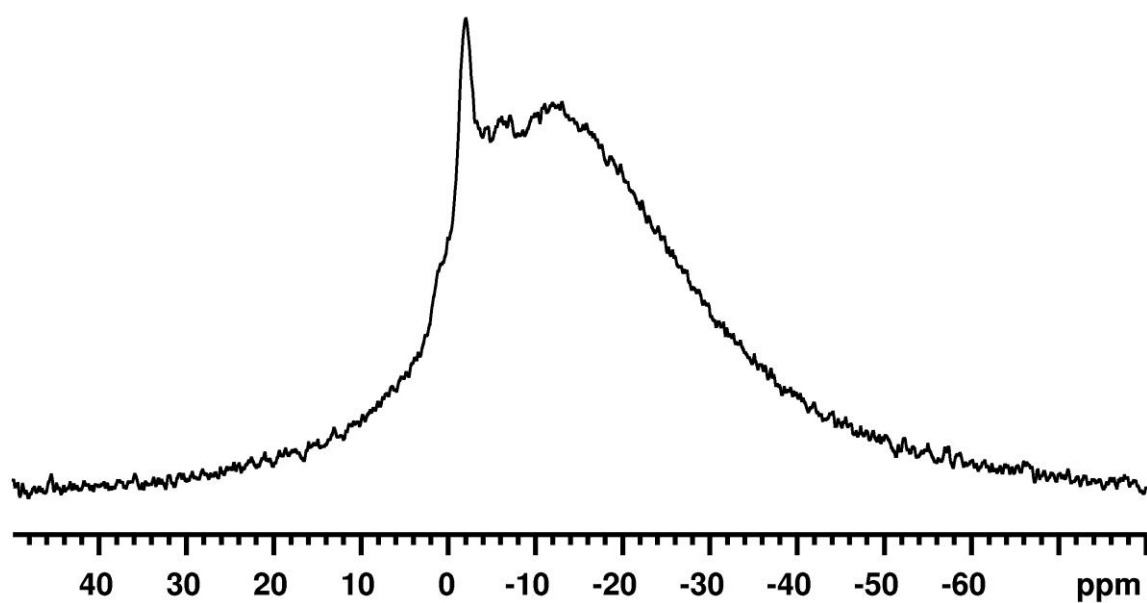


**Figure 5.9.** Experimental  $^{23}\text{Na}$  MAS NMR spectrum of glass **9** (all paramagnetic additives).

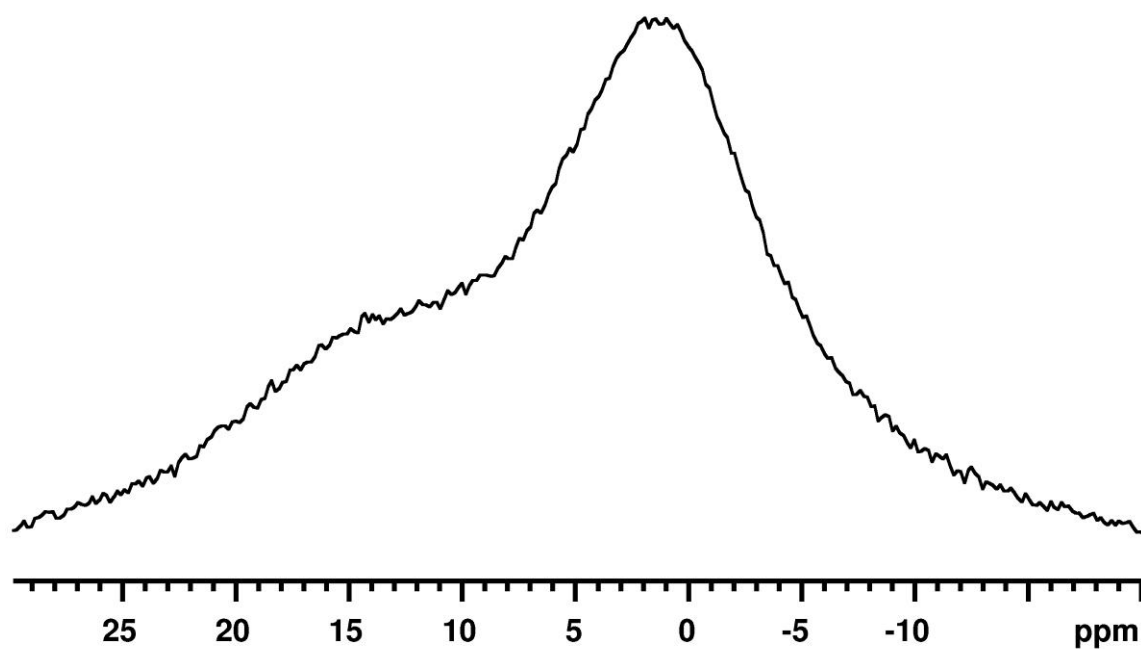


**Figure 5.10.** Experimental  $^{11}\text{B}$  MAS NMR spectrum of glass **9** (all paramagnetic additives).

## 5.4 Summary

The addition of paramagnetic oxides to our well-understood five-component glass system has shown that routine  $^{133}\text{Cs}$  and  $^{23}\text{Na}$  MAS NMR experiments remain viable in the presence of any one additive, and the observation and integration of phase-separated crystalline compounds from glasses **2-8** indicates the dominance of sodium- and cesium-sodium molybdates, as in glass **1**. The centrality of boron in glass network formation results in a higher sensitivity of  $^{11}\text{B}$  MAS NMR to the inclusion of paramagnetic additives, exhibiting broadening that scales as a function of additive concentration and paramagnetic strength (i.e., number of unpaired electrons). These effects suggest the incorporation of the transition metals as network modifiers that are accepted by the glass and do not crystallise as a detectable component of *yellow phase*.

The approach taken in the design of this glass series – adding paramagnetic oxides according to their factory concentrations – does not clearly establish a balanced comparison between the various additives. Therefore, it was necessary to fine-tune the design and create a sub-series of glasses to provide a gradient measure of each additive, thus allowing the observation of various broadening and structural effects that evolve as the paramagnetic oxide concentration is increased. Within this work, the two additives covered in this manner are  $\text{Cr}_2\text{O}_3$  (Chapter 6) and  $\text{Fe}_2\text{O}_3$  (Chapter 7).

# Chromium-Bearing Model HLW Glasses

*To investigate the behaviour of chromium in a simplified model nuclear waste glass system, including its role in phase separation and the effect of paramagnetic  $\text{Cr}^{3+}$  on the NMR spectra, a series of glasses with an increasing concentration of chromium (III) oxide ( $\text{Cr}_2\text{O}_3$ ) was prepared. Multinuclear magnetic resonance was used to characterise both the glassy and phase-separated crystalline material.  $^{133}\text{Cs}$ ,  $^{23}\text{Na}$ , and  $^{95}\text{Mo}$  NMR revealed the partitioning of chromium in the phase-separated products, while  $^{11}\text{B}$  and  $^{29}\text{Si}$  NMR of the glass network demonstrated broadening and relaxation effects, respectively, according to the presence of paramagnetic  $\text{Cr}^{3+}$ .*

## 6.1 Chromium in HLW Glasses

Chromium is a minor fission product and is also generated by melter container corrosion [78], with a concentration around 0.23 mol%  $\text{Cr}_2\text{O}_3$  in factory HLW glasses (see SON68 composition, Chapter 2, page 15). Compositional tuning of HLW glasses considers several key preparation and storage factors, including the balance between processing ability and waste loading. Due to their ability to exist in multiple oxidation states, incorporation of heavy-metal waste products requires control of the glass redox environment. For example, chromium may exist as  $\text{Cr}^{2+}$ ,  $\text{Cr}^{3+}$ ,  $\text{Cr}^{4+}$ ,  $\text{Cr}^{5+}$ , and  $\text{Cr}^{6+}$ , with each displaying particular solubility characteristics [64,79,80]. In the glass phase,  $\text{Cr}^{2+}$  is only found under strongly reducing conditions, and in general the majority of Cr exists as a balance of  $\text{Cr}^{3+}$  and  $\text{Cr}^{6+}$  in oxide environments [64]. Furthermore,  $\text{Cr}^{3+}$  is seen to phase-separate as eskolaite ( $\text{Cr}_2\text{O}_3$ ) or partition into spinel-type structures, while  $\text{Cr}^{6+}$  may

separate as part of a molten salt component (e.g., alkali-sulfates, -phosphates, and -molybdates), where it imparts the characteristic colour of *yellow phase* [13,81,82]. The chemistry of  $\text{Cr}^{6+}$  closely resembles that of  $\text{Mo}^{6+}$  in a series of cesium-metal oxides ( $\text{Cs}_2\text{XO}_4$ ,  $\text{Cs}_2\text{X}_3\text{O}_{10}$ , and  $\text{Cs}_2\text{X}_4\text{O}_{13}$ , where  $\text{X} = \text{Mo}$  or  $\text{Cr}$ ) [83-88] and it is therefore useful to understand the role of chromium in the formation of Cs-bearing *yellow phase*. The model waste glasses presented in this chapter serve to investigate Cr partitioning among phases while assessing the performance of solid-state NMR of a glass system that contains a variable concentration of paramagnetic centres.

It should be noted that one may perform NMR experiments on diamagnetic chromium environments using the NMR-active  $^{53}\text{Cr}$  nucleus (spin-3/2) [89]. Practically, however, with the low natural abundance (9.55%), low resonance frequency (33.9 MHz at 14.1 T), and large quadrupolar moment ( $Q = 15 \times 10^{-30} \text{ m}^2$ ) of  $^{53}\text{Cr}$ , coupled with the paramagnetic state (predominantly  $\text{Cr}^{3+}$ ) and low molar concentration of  $\text{Cr}_2\text{O}_3$  added to this series of glasses (between 0.05 and 2.48 mol%),  $^{53}\text{Cr}$  NMR experiments would be impractical for these samples.

## 6.2 Experimental

### 6.2.1 Glass Synthesis

Sodium borosilicate glasses containing cesium, molybdenum, and a variable level of chromium were prepared in a manner identical to that outlined in Chapter 5 (see page 37). The target and as-weighed glass compositions are listed in Table 6.1, showing how the levels of  $\text{Cr}_2\text{O}_3$  were gradually increased across the series (a total of five unique Na-B-Si-Cs-Mo-Cr oxide compositions) from 0.04 to 1.04 mol% at the expense of  $\text{Na}_2\text{O}$ ,  $\text{B}_2\text{O}_3$ , and  $\text{SiO}_2$  (by proportion, preserving the Na-B-Si ratio) while  $\text{Cs}_2\text{O}$  and  $\text{MoO}_3$  were held at 2.50 mol% each to induce crystallisation of the final product. To explore the phase-separation tendency of chromium in an alkali borosilicate independently from molybdenum, a sixth glass composition was prepared with

**Table 6.1.** Compositions of chromium series glasses (mol%) <sup>a</sup>

Sample		SiO <sub>2</sub>	B <sub>2</sub> O <sub>3</sub>	Na <sub>2</sub> O	Cs <sub>2</sub> O	MoO <sub>3</sub>	Cr <sub>2</sub> O <sub>3</sub>	Total
<b>Cr-1<sup>b</sup></b>	<b>Target</b>	61.80	17.49	15.67	2.50	2.50	0.04	100.00
	<b>Weighed</b>	61.05	17.20	15.53	3.71	2.46	0.05	100.00
	<b>EMPA</b>	61.05	16.24	13.92	1.22	0.69	0.002	93.12
		± 0.75	± 1.02	± 0.53	± 0.08	± 0.08	± 0.004	
<b>Cr-2</b>	<b>Target</b>	61.78	17.48	15.66	2.50	2.50	0.08	100.00
	<b>Weighed</b>	60.64	17.54	15.49	3.75	2.50	0.08	100.00
	<b>EMPA</b>	60.64	14.02	13.78	0.88	0.66	0.05	90.04
		± 0.70	± 0.64	± 0.23	± 0.04	± 0.06	± 0.01	
	<b>LA-ICP-MS</b>	60.64	13.69	13.67	0.87	0.69	0.04	89.60
	<b>(spot)</b>	n/a	± 0.06	± 0.94	± 0.04	± 0.07	± 0.01	
<b>Cr-3<sup>b</sup></b>	<b>Target</b>	61.75	17.47	15.65	2.50	2.50	0.13	100.00
	<b>Weighed</b>	60.93	17.27	15.43	3.75	2.46	0.16	100.00
	<b>EMPA</b>	60.93	17.71	14.96	2.22	0.67	0.11	96.59
		± 0.55	± 0.71	± 0.29	± 0.06	± 0.05	± 0.01	
<b>Cr-4<sup>b</sup></b>	<b>Target</b>	61.50	17.39	15.59	2.50	2.50	0.52	100.00
	<b>Weighed</b>	60.45	17.26	15.50	3.71	2.56	0.52	100.00
	<b>EMPA</b>	60.45	17.92	14.21	2.31	0.60	0.32	95.81
		± 0.63	± 0.74	± 0.30	± 0.06	± 0.06	± 0.06	
<b>Cr-5</b>	<b>Target</b>	61.16	17.29	15.51	2.50	2.50	1.04	100.00
	<b>Weighed</b>	60.22	17.10	15.28	3.75	2.53	1.12	100.00
	<b>EMPA</b>	60.22	15.10	13.54	0.97	0.63	0.69	91.15
		± 0.83	± 0.96	± 0.68	± 0.04	± 0.05	± 0.04	
	<b>LA-ICP-MS</b>	60.22	12.88	11.51	0.98	0.49	0.40	86.47
	<b>(spot)</b>	n/a	± 0.89	± 0.52	± 0.02	± 0.07	± 0.07	
<b>Cr-5<sup>b</sup> (duplicate)</b>	<b>LA-ICP-MS</b>	60.22	13.15	11.33	1.14	0.45	0.37	86.67
	<b>(line)</b>	± 1.26	± 0.88	± 0.78	± 0.10	± 0.04	± 0.04	
	<b>Target</b>	61.16	17.29	15.51	2.50	2.50	1.04	100.00
	<b>Weighed</b>	60.41	16.97	15.20	3.76	2.54	1.12	100.00
<b>Cr-6<sup>b</sup></b>	<b>EMPA</b>	60.41	15.48	13.96	1.49	0.66	0.69	94.96
		± 0.85	± 0.81	± 0.24	± 0.07	± 0.10	± 0.04	
	<b>LA-ICP-MS</b>	60.41	15.56	12.24	1.53	0.66	0.47	90.87
	<b>(spot)</b>	n/a	± 0.77	± 1.15	± 0.19	± 0.05	± 0.05	
<b>Cr-6<sup>b</sup></b>	<b>LA-ICP-MS</b>	60.41	16.18	11.89	1.69	0.51	0.36	91.05
	<b>(line)</b>	± 1.24	± 0.93	± 0.67	± 0.15	± 0.07	± 0.05	

<sup>a</sup> Compositions by EMPA and LA-ICP-MS are normalised to the nominal ('weighed') mol% SiO<sub>2</sub> (see text).<sup>b</sup> Denotes samples that were prepared with a lid on the crucible.



2.50 mol%  $\text{Cr}_2\text{O}_3$  (glass “Cr-6”) and contains no  $\text{MoO}_3$ . While all samples received identical heat treatments, some were prepared with the use of a lid to cover the crucible (discussed later).

From this series of six glass compositions, a total of three glasses - “Cr-1r” (a replicate trial of Cr-1), “Cr-3”, and “Cr-4” - produced phase-separated crystalline deposits that were easily separated by hand. These *yellow phase* samples are named YP1, YP3, and YP4 according to the parent glass from which they were separated.

### 6.2.2 Elemental Analysis

*Electron Microprobe Analysis (EMPA).* Sample compositions for glasses Cr-1 through Cr-5 and the crystalline phase assemblage YP4 were analysed by EMPA (Department of Geology, University of Manitoba, with assistance from Dr. Ravinder Sidhu). A beam current of 10 nA and diameter of 40  $\mu\text{m}$  was used to analyse the glass samples, while a beam diameter of 20  $\mu\text{m}$  was used for ground glass samples and the crystalline sample. The total number of measurements made for each sample was between 6 and 15 spots, from which an average value and standard deviation were determined. The effects of sodium mobility (i.e., migration away from measurement area; underestimate of  $\text{Na}_2\text{O}$  concentrations) were corrected using a linear regression method by calibration of a glass standard composed of 79% Si and 14% Na. [90,91]

*Laser-Ablation Inductively-Coupled-Plasma Mass Spectrometry (LA-ICP-MS).* Sample compositions for glasses Cr-2, Cr-3, and Cr-5 were analysed by LA-ICP-MS (Department of Geology, University of Manitoba, with assistance from Dr. Panseok Yang) using both spot measurements and line profiles. A laser energy of 30  $\text{J cm}^{-2}$ , beam width of 30  $\mu\text{m}$ , ablation frequency of 10 Hz, and ablation speed between 2-5  $\mu\text{m/s}$  (for line measurements) was used to analyse elemental profiles across the sample surface. Due to penetration of the laser through the crystalline deposits, only reliable measurements for the glass phase could be made.

### 6.2.3 Nuclear Magnetic Resonance Spectroscopy

All NMR experiments were conducted on a Varian <sup>Unity</sup>Inova 600 ( $B_0 = 14.1$  T) spectrometer using a 1.6 mm triple-resonance Varian-Chemmagetics MAS probe at a spinning rate of 30 kHz, unless otherwise stated. The samples were ground using an agate mortar and pestle and packed into appropriately sized ZrO<sub>2</sub> rotors.

<sup>133</sup>Cs MAS NMR spectra of all samples (“Cr” glasses and crystalline “YP” assemblages) were collected in a manner identical to that outlined in Chapter 5 (see page 40), with the exception that the YP samples were collected with optimised recycle delays between 200 and 500 s. Additional <sup>133</sup>Cs NMR spectra were collected on a Bruker Avance II 900 ( $B_0 = 21.1$  T) spectrometer with a 1.3 mm Bruker MAS probe at a spinning frequency of 60 kHz, using single-pulse experiments (0.4  $\mu$ s,  $\sim 30^\circ$  tip angle,  $\nu_{rf} = 71$  kHz) with a 60 s recycle delay and 512 co-added transients. Pulse calibration and spectral referencing on both spectrometers were completed with an aqueous solution of cesium chloride (0.1 M CsCl, 0 ppm).

<sup>23</sup>Na MAS NMR spectra of all samples were collected using single-pulse experiments (0.19  $\mu$ s,  $\sim 15^\circ$  tip angle,  $\nu_{rf} = 111$  kHz) with recycle delays of 1 s, and between 256 and 3072 co-added transients. Additionally, single-pulse (for samples Cr-2, YP3, and YP4) (0.15 to 1.0  $\mu$ s,  $15^\circ$  to  $60^\circ$  tip angle,  $\nu_{rf} = 93$  kHz) and two-dimensional (3QMAS; for YP4) experiments were conducted on the 21.1 T instrument with a 2.5 mm MAS probe at spinning rates between 20 and 30 kHz. Pulse calibration and spectral referencing on both spectrometers were completed with an aqueous solution of sodium chloride (1 M NaCl, 0 ppm).

<sup>95</sup>Mo MAS NMR spectra of YP1, YP3, and YP4 were collected using single-pulse experiments (1.4  $\mu$ s,  $90^\circ$  tip angle,  $\nu_{rf} = 59$  kHz) with recycle delays between 30 and 120 s, and between 224 and 3072 co-added transients. <sup>95</sup>Mo MAS NMR was conducted on glass sample Cr-2 with a 5 mm MAS probe at a spinning rate of 5 kHz, using a single-pulse experiment

(1.5  $\mu$ s,  $\sim 30^\circ$  tip angle,  $\nu_{\text{rf}} = 19$  kHz) with a 10 s recycle delay and 94 000 co-added transients. An additional  $^{95}\text{Mo}$  NMR spectrum of Cr-2 was collected on the 21.1 T instrument with a 7 mm MAS probe at a spinning rate of 9 kHz, using a single-pulse experiment (1.5  $\mu$ s,  $\sim 30^\circ$  tip angle,  $\nu_{\text{rf}} = 21$  kHz) with a 10 s recycle delay and 4096 co-added transients. Pulse calibration and spectral referencing on both spectrometers were completed with an aqueous solution of sodium molybdate (0.1 M  $\text{Na}_2\text{MoO}_4$ , 0 ppm).

$^{11}\text{B}$  MAS NMR spectra for Cr glass samples were collected using single-pulse experiments (0.16  $\mu$ s,  $15^\circ$  tip angle,  $\nu_{\text{rf}} = 250$  kHz) with a 1 s recycle delay and 512 co-added transients. Pulse calibration and spectral referencing were completed with an aqueous solution of boric acid (0.1 M  $\text{B}(\text{OH})_3$ , 19.6 ppm).

$^{29}\text{Si}$  MAS NMR experiments were conducted on a Bruker Avance III 400 ( $B_0 = 9.4$  T) using a 4 mm Bruker MAS probe to evaluate the  $^{29}\text{Si}$   $T_1$  relaxation time of the five-component base glass (see composition in Table 5.1, page 40) and selected Cr glasses (Cr-2, Cr-3, and Cr-4). Variable-delay spectra were collected using an optimised *saturation recovery* pulse sequence [92,93] with a 1 s recycle delay and 256 co-added transients. Pulse calibration and spectral referencing were completed with a solution of hexamethyldisiloxane ( $\text{O}[\text{Si}(\text{CH}_3)_3]_2$ , 6.7 ppm).

### 6.3 Results and Discussion

Sample masses were measured pre- and post-decarbonation, and again after high-temperature treatment, where it was found that the final masses were between 5 and 15% lower than expected. This is attributed to the volatilisation of cesium oxide at  $1300^\circ\text{C}$  over the one-hour holding time [18,68]. The gradual increase in chromium content over the series is visually apparent by an increasing intensity in the green colour of the glassy portion, which also indicates the predominance of  $\text{Cr}^{3+}$  (over  $\text{Cr}^{6+}$ ) in the glassy phase. Several phase-separated crystalline

deposits were observable across the glass surface and appeared yellow in colour due to the presumed inclusion of chromium as  $\text{Cr}^{6+}$ .

### 6.3.1 Compositional Analyses of the Bulk Material

To verify the final sample compositions, elemental analysis (by EMPA and LA-ICP-MS) was conducted. The glass-phase compositions obtained through EMPA and LA-ICP-MS are shown in Table 6.1 (page 58), contrasted against the target and as-weighed compositions. The analysed glass-phase compositions are normalised using the weighed amount of  $\text{SiO}_2$ , assuming it to be the component least likely to volatilise. Using this approach, it can be noted that the mol% totals of the analysed compositions do not sum to unity, which can be attributed to volatilisation during heating (for  $\text{Cs}_2\text{O}$ ) and phase separation (facilitated by  $\text{MoO}_3$ ) during cooling. For example, the tabulated compositions indicate  $\text{MoO}_3$  concentrations in the glass of around 0.65 mol% (by EMPA), representing a consistent solubility limit for Mo under this particular model treatment. This suggests that approximately 1.85 mol%  $\text{MoO}_3$  (i.e., the difference between the ‘weighed’ and ‘analysed’ contribution for this component) separates to form crystalline molybdate phases. Correspondingly, the molar fractions of  $\text{Na}_2\text{O}$ ,  $\text{Cs}_2\text{O}$ , and  $\text{Cr}_2\text{O}_3$  also appear lower than their nominal levels, reflecting either their sequestration by  $\text{MoO}_4^{2-}$  or inclusion as other *yellow phase* components. The analysed composition of the crystalline phase assemblage YP4 (by EMPA) is discussed in section 6.3.4.

A comparison of the two analytical methods used for elemental analysis, EMPA and LA-ICP-MS, shows the former to provide better agreement with the nominal compositions regarding  $\text{B}_2\text{O}_3$  and  $\text{Na}_2\text{O}$ , where LA-ICP-MS shows (in general) an appreciable decrease in these components. This effect may be explained by an increased mobility of  $\text{Na}_2\text{O}$  under exposure to the high power and temperature of the ablation laser, causing migration to areas away from the

ablation zone. LA-ICP-MS  $B_2O_3$  mol% values were closer to the ‘weighed’ and EMPA values when collection was conducted as a line measurement (continuous ablation over a specified distance), while  $Na_2O$  values determined by LA-ICP-MS showed better agreement when collected as a spot measurement (continuous ablation on a single spot). However, the line measurements more effectively characterise the bulk composition due to their ability to probe inhomogeneity across the sample. An example of an LA-ICP-MS line profile is shown in Figure 6.1, where the distinct crystalline regions can be noted by decreases in glassy constituents ( $SiO_2$  and  $B_2O_3$ ) with corresponding increases in the crystalline components ( $Cs_2O$  is used as an example).

Glass samples were prepared in the high-temperature furnace two at a time, with one crucible stacked upon the other using a metal plate lid between the two. To test the sensitivity of  $Cs_2O$  volatilisation with respect to sample handling during heating (i.e., presence or absence of a lid), a duplicate trial of glass Cr-5 was prepared using a lid during high-temperature treatment (whereas the original Cr-5 was prepared without a lid). Comparing the two trials in Table 6.1, it can be seen that the use of a crucible lid allowed for the retention of approximately 50% more cesium throughout the high-temperature cycle for this sample. Undoubtedly, more trials would be required to obtain a quantitative assessment of this effect (and to control for possible variability in the amount of  $Cs_2O$  being incorporated into the *yellow phase*), however the test involving Cr-5 demonstrates the importance of crucible coverage during high-temperature heating. Samples prepared with the use of a crucible lid have been identified in Table 6.1 accordingly, which show more  $Cs_2O$  than those prepared without a lid.

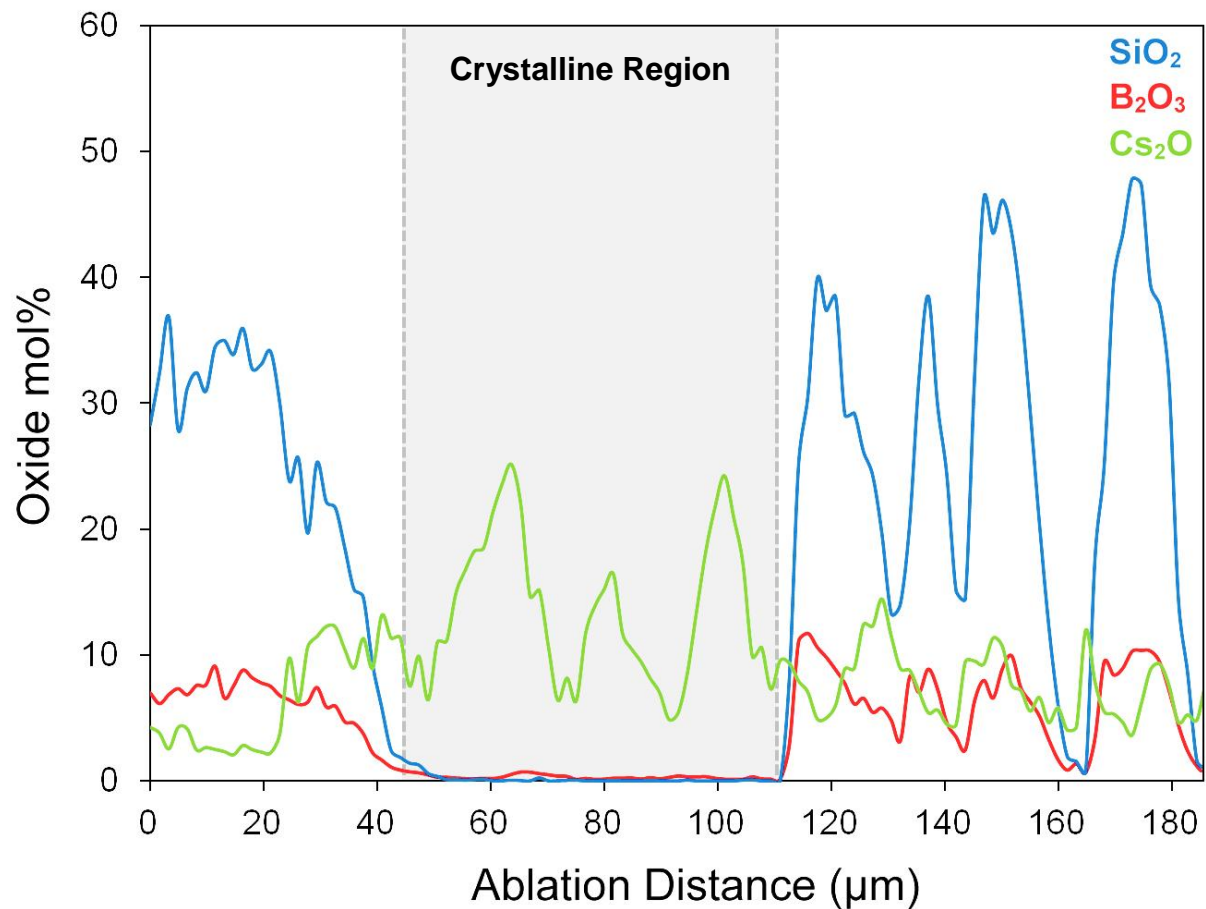


**Figure 6.1.** LA-ICP-MS line profile of a phase-separated Cr-containing glass. The region between 45-110  $\mu\text{m}$  (shaded) represents a crystalline deposit, where the contributions from the glassy components SiO<sub>2</sub> and B<sub>2</sub>O<sub>3</sub> sharply drop as they are not present in *yellow phase*. The variability of Cs<sub>2</sub>O in this region reflects the heterogeneity of the *yellow phase* deposit, while variations elsewhere (including those in SiO<sub>2</sub> and B<sub>2</sub>O<sub>3</sub>) represent smaller crystalline deposits on the glass surface.

### 6.3.2 NMR of the Bulk Material

<sup>133</sup>Cs MAS NMR. The <sup>133</sup>Cs MAS NMR spectra of glasses Cr-1 through Cr-6 are shown in Figure 6.2, where CsNaMoO<sub>4</sub>•2H<sub>2</sub>O (-71 ppm) is the most commonly observed compound (seen in glasses Cr-2, Cr-3, and Cr-4). Additionally, two phases that were mentioned (but not observed) in Chapter 5 – Cs<sub>2</sub>MoO<sub>4</sub> (55 & -16 ppm) and Cs<sub>2</sub>CrO<sub>4</sub> (26 & -100 ppm) – are observed across the spectra of glasses Cr-2, Cr-3, and Cr-4, to varying degrees. Additionally, glass Cr-5 shows a number of sites in the region between -120 and -200 ppm. The largest of these peaks, situated at -151 ppm, resembles that of Cs(2) from Cs<sub>3</sub>Na(MoO<sub>4</sub>)<sub>2</sub> (-145 ppm), however no accompanying Cs(1) site is observed at 161 ppm. Glass Cr-1 produced only a small amount of Cs<sub>3</sub>Na(MoO<sub>4</sub>)<sub>2</sub>, and when this sample was prepared a second time (as “Cr-1r”), a larger amount of phase-separated crystalline material was produced ; the multinuclear magnetic resonance results of this hand-separated product (“YP1”) are described in section 6.3.3.

Glass Cr-6 (which contains no MoO<sub>3</sub>) clearly shows the occurrence of phase separation, presumably of some unknown Cs-containing chromate phase(s). The first three peaks of the series present in the <sup>133</sup>Cs NMR of Cr-6 appear at a consistent separation of 23 ppm and relative ratio of 18:33:49, perhaps indicating that these observed sites are related (e.g., by discrete Cs-Na environments). The final peak at 151 ppm appears to be the same as that observed in Cr-5, indicating that it does not represent a molybdate compound. The integrated intensities of the <sup>133</sup>Cs MAS NMR spectra are listed in Table 6.2 (note that manual removal of crystalline *yellow phase* from samples Cr-3 and Cr-4 decreases the contribution of the crystalline products). A more precise breakdown of the unknown sites for Cr-5 and Cr-6, including their chemical shifts and integrated intensities, is shown in Table 6.3.

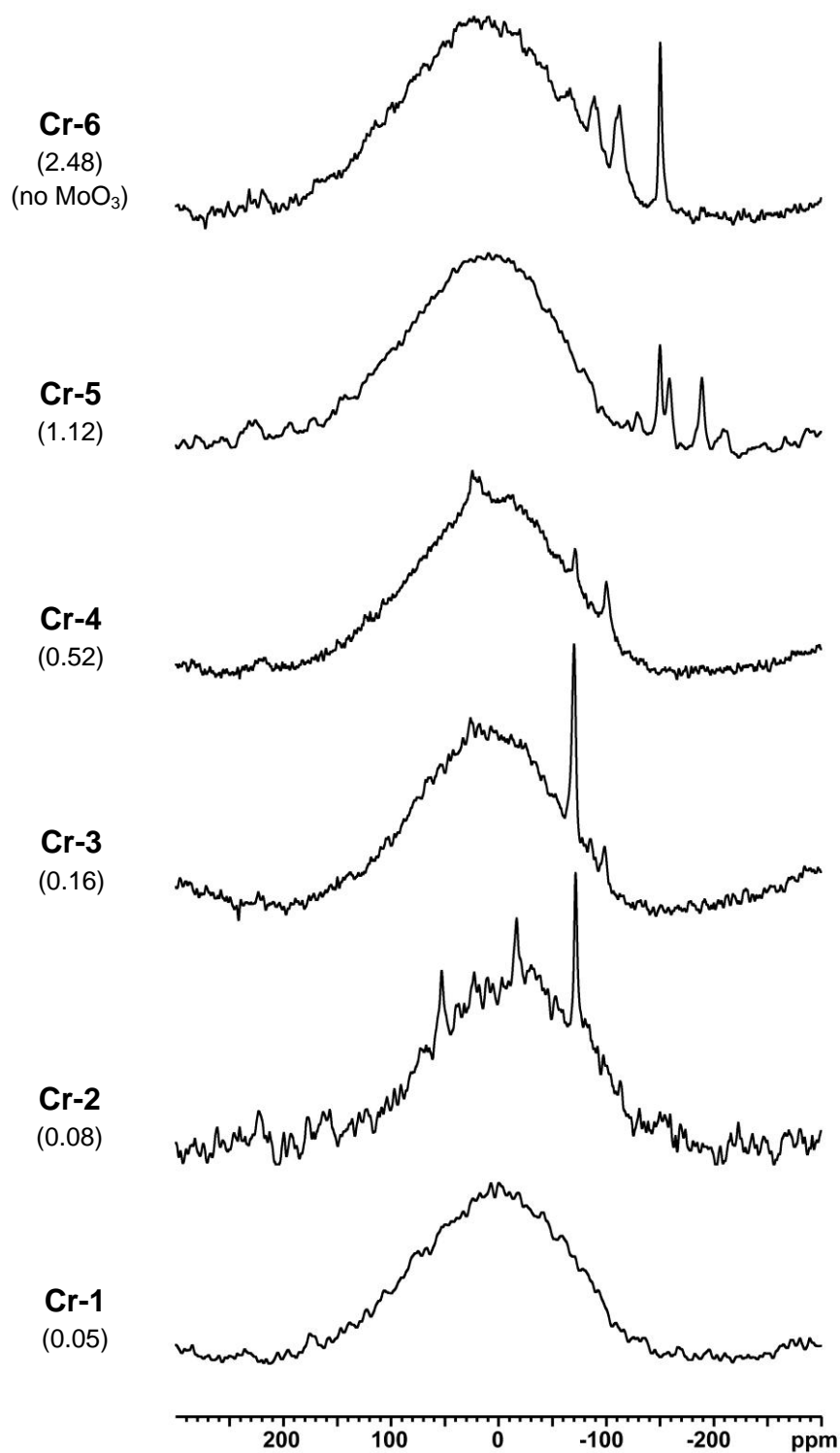


**Figure 6.2.** Experimental  $^{133}\text{Cs}$  MAS NMR spectra of chromium series glasses. The nominal ('weighed') mol% of  $\text{Cr}_2\text{O}_3$  is noted beneath each sample name.



**Table 6.2.** Integrated intensities (%) for  $^{133}\text{Cs}$  MAS NMR of Cr series glasses

Glass Sample	Component					
	Glass	$\text{Cs}_2\text{MoO}_4$	$\text{Cs}_2\text{CrO}_4$	$\text{CsNaMoO}_4 \cdot 2\text{H}_2\text{O}$	$\text{Cs}_3\text{Na}(\text{MoO}_4)_2$	Unknown
<b>Cr-1</b>	98.7	-	-	-	1.3	-
	$\pm 0.6$	-	-	-	$\pm 0.6$	-
<b>Cr-2</b>	94.9	2.3	-	2.8	-	-
	$\pm 0.9$	$\pm 0.4$	-	$\pm 0.5$	-	-
<b>Cr-3<sup>a</sup></b>	95.1	-	1.0	2.9	-	1.0
	$\pm 0.9$	-	$\pm 0.2$	$\pm 0.3$	-	$\pm 0.4$
<b>Cr-4<sup>a</sup></b>	96.0	-	1.9	0.8	-	0.3
	$\pm 0.6$	-	$\pm 0.2$	$\pm 0.1$	-	$\pm 0.1$
<b>Cr-5</b>	93.4	-	-	-	-	6.6
	$\pm 0.7$	-	-	-	-	$\pm 0.7$
<b>Cr-6</b>	95.2	-	-	-	-	4.8
	$\pm 0.4$	-	-	-	-	$\pm 0.4$

<sup>a</sup> Integrated intensities represent what remains after a large portion of phase-separated crystalline material (YP3, YP4) was hand-separated.

**Table 6.3.** Integrated intensities (%) of unknown  $^{133}\text{Cs}$  NMR sites of Cr-5 and Cr-6 glasses

Glass Sample	Glass	Unknown Chemical Shifts (ppm)								
		230	-67	-89	-113	-130	-151	-160	-190	-210
<b>Cr-5</b>	93.4	1.3	-	-	-	0.2	1.4	1.2	1.3	1.2
	$\pm 0.7$	$\pm 0.2$	-	-	-	$\pm 0.1$	$\pm 0.1$	$\pm 0.1$	$\pm 0.1$	$\pm 0.1$
<b>Cr-6</b>	95.2	-	0.6	1.1	1.6	-	1.5	-	-	-
	$\pm 0.4$	-	$\pm 0.1$	$\pm 0.1$	$\pm 0.1$	-	$\pm 0.1$	-	-	-

<sup>23</sup>Na MAS NMR. The <sup>23</sup>Na MAS NMR spectra of glasses Cr-1 through Cr-6 are shown in Figure 6.3. The most obvious feature in these spectra is the narrow signal around -2 ppm, which can be attributed to both Na(1) of Na<sub>2</sub>MoO<sub>4</sub>•2H<sub>2</sub>O and the single site of CsNaMoO<sub>4</sub>•2H<sub>2</sub>O (see section 5.3.2). Given the overlap of the previously mentioned spectral patterns, as well as Na<sub>2</sub>MoO<sub>4</sub> and Na(2) of Na<sub>2</sub>MoO<sub>4</sub>•2H<sub>2</sub>O, deconvolution of the <sup>23</sup>Na MAS NMR spectra are not as straightforward as those of <sup>133</sup>Cs MAS NMR. However, the integrated relationship of cesium-sodium molybdates by <sup>23</sup>Na NMR establishes a link to the <sup>133</sup>Cs NMR, showing anhydrous and hydrated Na<sub>2</sub>MoO<sub>4</sub> to be the dominant products of phase-separation in glasses Cr-1 through Cr-5. The integrated intensities of the <sup>23</sup>Na NMR spectra are listed in Table 6.4, determined through a peak-fitting procedure identical to that described in Chapter 5.

<sup>23</sup>Na MAS NMR of glass Cr-6 reveals a sodium signature that is likely paired with at least one of the three unknown peaks observed in the <sup>133</sup>Cs MAS NMR spectrum. The unknown <sup>133</sup>Cs NMR peak at -151 ppm, detected in appreciable levels in both Cr-5 and Cr-6, must not be tied to the unknown <sup>23</sup>Na NMR site, since the latter is only observed in <sup>23</sup>Na NMR of Cr-6. Deconvolution of the Cr-6 <sup>23</sup>Na MAS NMR spectrum (Figure 6.4) can be accomplished using four sites (i.e., one for sodium in glassy environments and three for the unknown crystalline signals that were required for the remaining intensity). The quadrupolar shape (orange trace in Figure 6.4) was simulated with  $C_Q = 2.3 \pm 0.2$  MHz,  $\eta = 0.2 \pm 0.2$ , and  $\delta_{iso} = 0.0 \pm 0.5$  ppm.

<sup>95</sup>Mo MAS NMR. The <sup>95</sup>Mo MAS NMR spectra of glass Cr-2, collected at 14.1 T and 21.1 T, are shown in Figure 6.5. Given the experimental difficulties and lengthy collection times of <sup>95</sup>Mo NMR (see Chapter 4), the glass sample Cr-2 was chosen because of its high degree of crystallinity (as measured by <sup>133</sup>Cs and <sup>23</sup>Na NMR integrations) and varying crystallisation products (Na<sub>2</sub>MoO<sub>4</sub>, Na<sub>2</sub>MoO<sub>4</sub>•2H<sub>2</sub>O, Cs<sub>2</sub>MoO<sub>4</sub>, CsNaMoO<sub>4</sub>•2H<sub>2</sub>O, and Cs<sub>3</sub>Na(MoO<sub>4</sub>)<sub>2</sub>) were

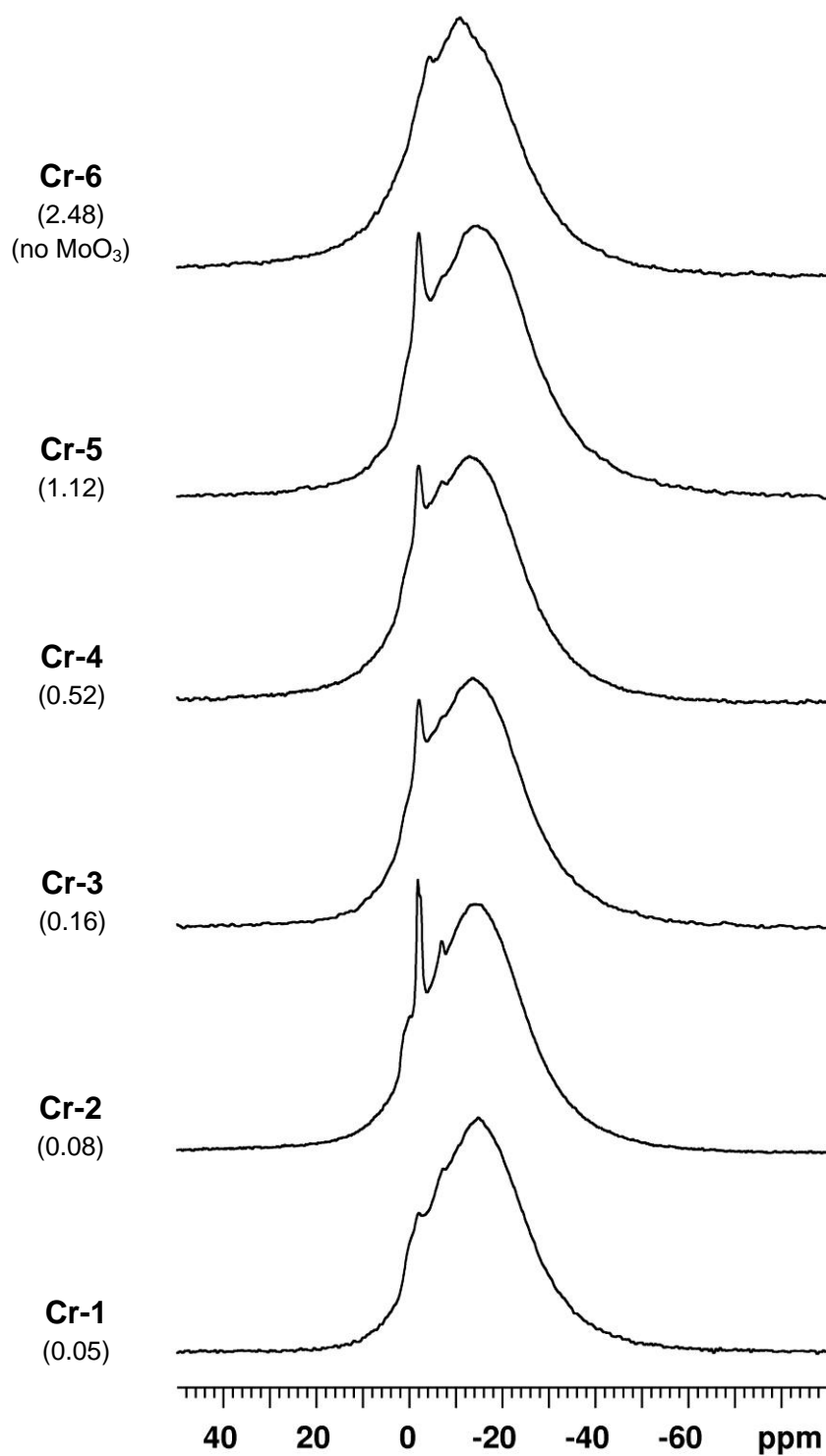


**Figure 6.3.** Experimental  $^{23}\text{Na}$  MAS NMR spectra of chromium series glasses. The nominal ('weighed') mol% of  $\text{Cr}_2\text{O}_3$  is noted beneath each sample name.

**Table 6.4.** Integrated intensities (%) for  $^{23}\text{Na}$  MAS NMR of Cr series glasses

Glass Sample	Component				
	Glass	$\text{Na}_2\text{MoO}_4$	$\text{Na}_2\text{MoO}_4 \cdot 2\text{H}_2\text{O}$	$\text{CsNaMoO}_4 \cdot 2\text{H}_2\text{O}$	Unknown
<b>Cr-1</b>	94.9	4.1	1.0	-	-
	$\pm 0.6$	$\pm 0.4$	$\pm 0.2$	-	-
<b>Cr-2</b>	94.5	0.8	3.6	1.1	-
	$\pm 1.0$	$\pm 0.4$	$\pm 0.2$	$\pm 0.4$	-
<b>Cr-3</b>	95.2	0.1	3.3	1.4	-
	$\pm 0.8$	$\pm 0.1$	$\pm 0.4$	$\pm 0.3$	-
<b>Cr-4</b>	95.3	0.1	3.9	0.7	-
	$\pm 0.5$	$\pm 0.1$	$\pm 0.2$	$\pm 0.2$	-
<b>Cr-5</b>	94.9	0.7	4.4	-	-
	$\pm 0.7$	$\pm 0.3$	$\pm 0.4$	-	-
<b>Cr-6</b>	96.0	-	-	-	4.0
	$\pm 0.4$	-	-	-	$\pm 0.4$

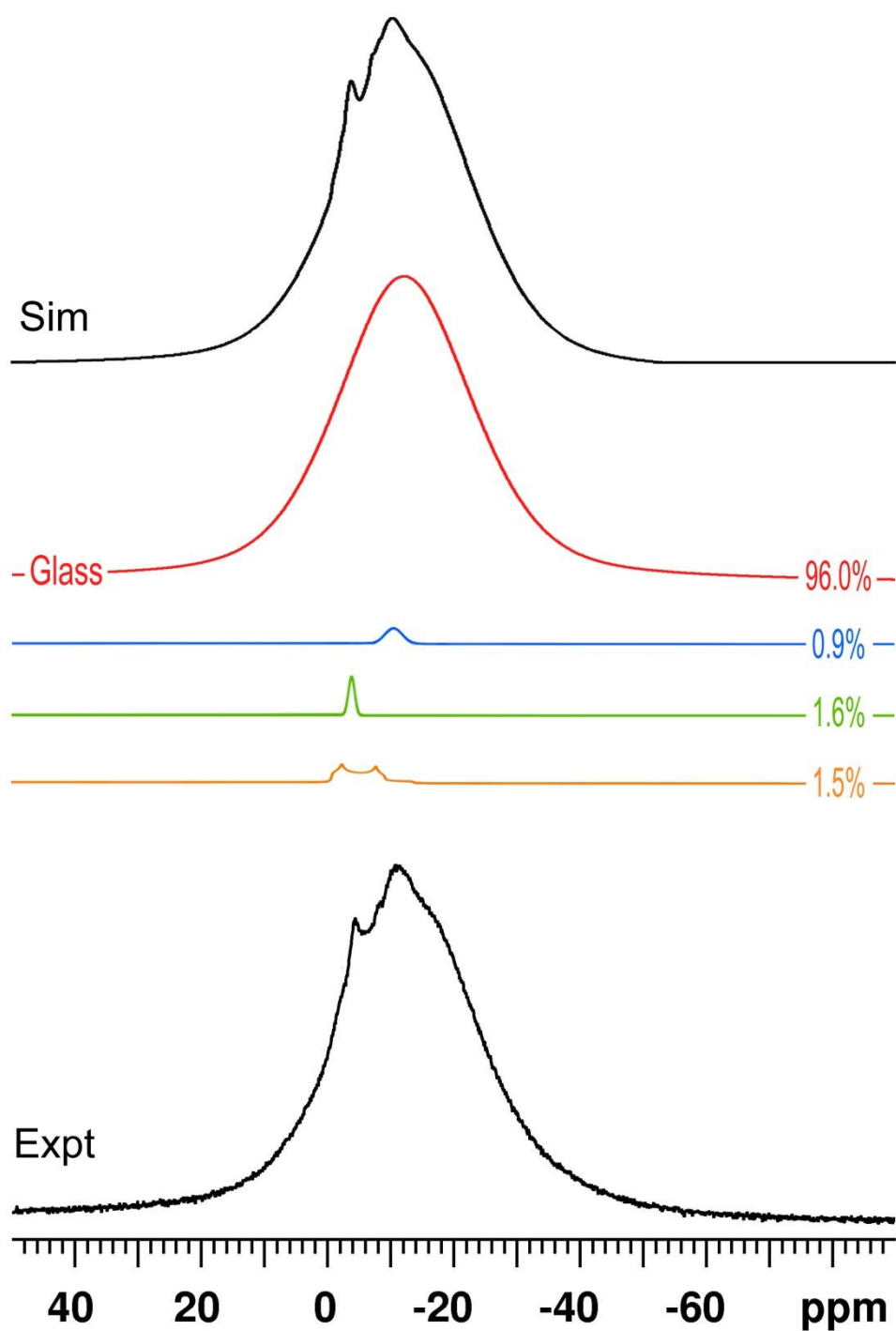


**Figure 6.4.** Experimental  $^{23}\text{Na}$  MAS NMR spectrum of glass Cr-6 (lower), with overall simulation and deconvolution of sites; Na in glassy environments (red), unknown at -11 ppm (blue), unknown at -4 ppm (green), and unknown with quadrupolar fit (orange). Integrated intensities are noted on the right.

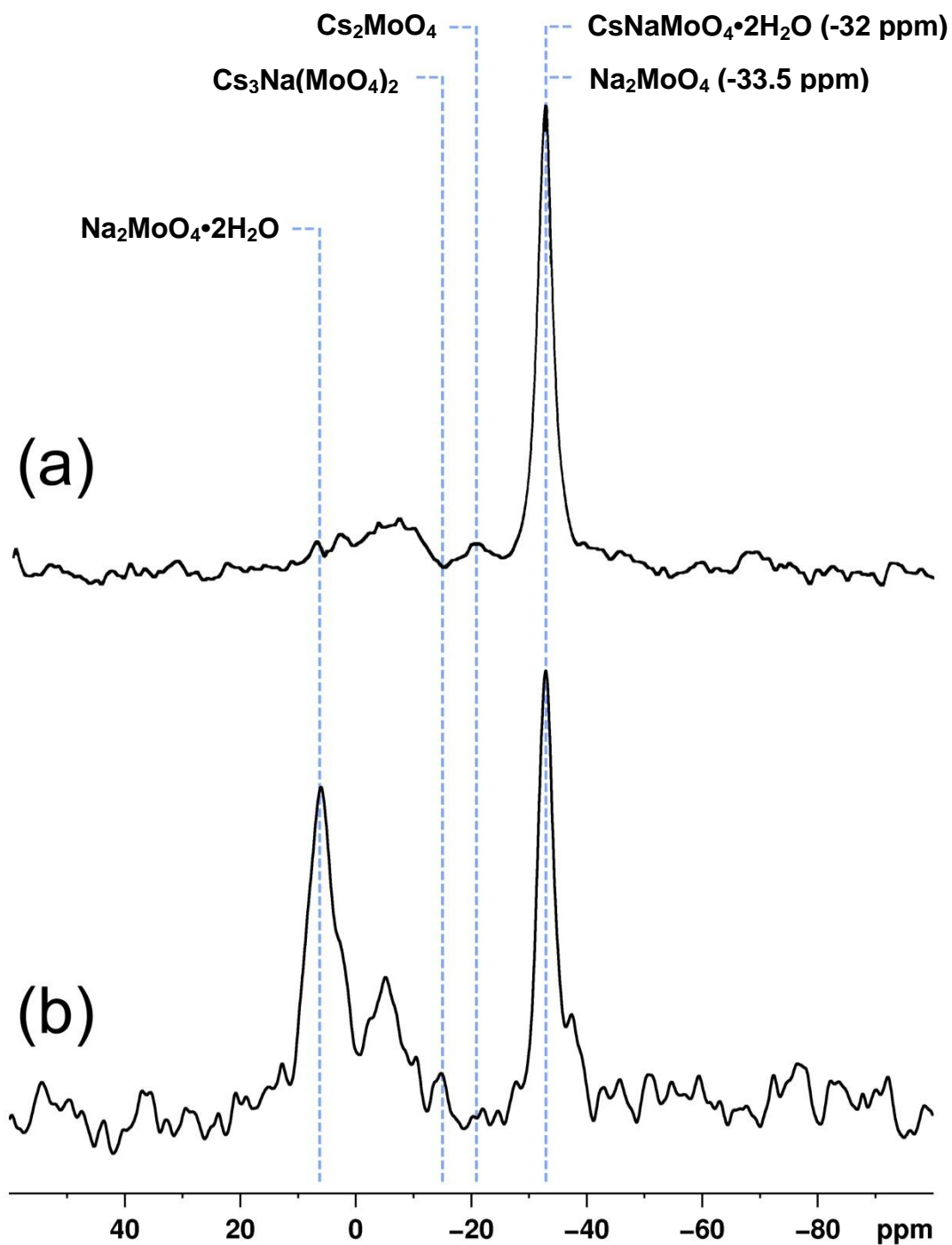


**Figure 6.5.** Experimental  $^{95}\text{Mo}$  MAS NMR spectrum of glass Cr-2 at (a) 14.1 T (39.1 MHz) and (b) 21.1 T (58.7 MHz). The known peak positions of selected molybdates have been noted.

**Table 6.5.**  $^{95}\text{Mo}$  NMR parameters of relevant molybdenum-bearing compounds

Site	$C_Q$ (MHz)	$\eta$	$\delta_{\text{iso}}$ (ppm)	Reference
$\text{Na}_2\text{MoO}_4$	0	1	-33.5	[45]
$\text{Na}_2\text{MoO}_4 \cdot 2\text{H}_2\text{O}$	1.15	0.82	8	[46]
$\text{Cs}_2\text{MoO}_4$	0	n.d.	-25	[45]
$\text{CsNaMoO}_4 \cdot 2\text{H}_2\text{O}$	n.d.	n.d.	-32	[20]
$\text{Cs}_3\text{Na}(\text{MoO}_4)_2$	n.d.	n.d.	-15	[20]
Glass ( $\text{MoO}_4$ )	n.d.	n.d.	$20 \rightarrow -80^a$	[20,21,51,52]

<sup>a</sup> Depending on the local environment, glassy  $\text{MoO}_4$  can take a wide range of values. The actual peak breadths will differ from this range and between samples.

identified by  $^{133}\text{Cs}$  and/or  $^{23}\text{Na}$  NMR). Indeed, many of these sites are observed in both  $^{95}\text{Mo}$  NMR spectra, and their parameters are summarised in Table 6.5. The 21.1 T spectrum reveals  $\text{Na}_2\text{MoO}_4 \cdot 2\text{H}_2\text{O}$  (-8 ppm),  $\text{Na}_2\text{MoO}_4$  (-33.5 ppm), and  $\text{CsNaMoO}_4 \cdot 2\text{H}_2\text{O}$  (-32 ppm) as the largest contributing components. Interestingly, the 14.1 T spectrum does not show the presence of  $\text{Na}_2\text{MoO}_4 \cdot 2\text{H}_2\text{O}$ . However, this was caused by atmospheric sample hydration during preparation of the sample for the 21.1 T spectrometer, while that used for the 14.1 T collection was prepared in dry conditions directly after removal from the desiccator in which the sample was stored (discussed in section 6.3.3).

$^{11}\text{B}$  MAS NMR. The  $^{11}\text{B}$  MAS NMR spectra of glasses Cr-1 through Cr-5 are shown in Figure 6.6 along with the spectrum of the five-component base glass for reference. As expected based on the results from Chapter 5 (see section 5.3.3, page 50), the increasing  $\text{Cr}_2\text{O}_3$  content is reflected by an increasing breadth of the  $^{13}\text{B}$  and  $^{14}\text{B}$  sites. At higher loadings (glasses Cr-3, Cr-4, and Cr-5) the sites become sufficiently broadened that the resolution of  $^{13}\text{B}$  and  $^{14}\text{B}$  is affected. Furthermore, the increased breadth results in decreased relative peak heights, meaning that a greater number of co-added transients would be desired for glasses with higher  $\text{Cr}_2\text{O}_3$  content to offer more accurate spectral fitting for integration.

The FWHM values of the two sites are noted in Figure 6.6 and plotted against the  $2S \cdot \text{mol}\%$  factor (for consistency with the Chapter 5 results) in Figure 6.7, showing a roughly linear dependency between  $\text{Cr}_2\text{O}_3$  content and spectral breadth for each site. While the difference in breadth between Cr-5 and the base glass is greater for  $^{13}\text{B}$  (difference of 415 Hz) than  $^{14}\text{B}$  (difference of 153 Hz), their relative broadening factors (ratio of Cr-5 breadth to base glass breadth) are in agreement ; 1.28 for  $^{13}\text{B}$  and 1.25 for  $^{14}\text{B}$ . A  $^{11}\text{B}$  MAS NMR study of rare-earth-doped aluminoborate glasses has shown a linear dependence between  $^{13}\text{B}$  and  $^{14}\text{B}$  broadening



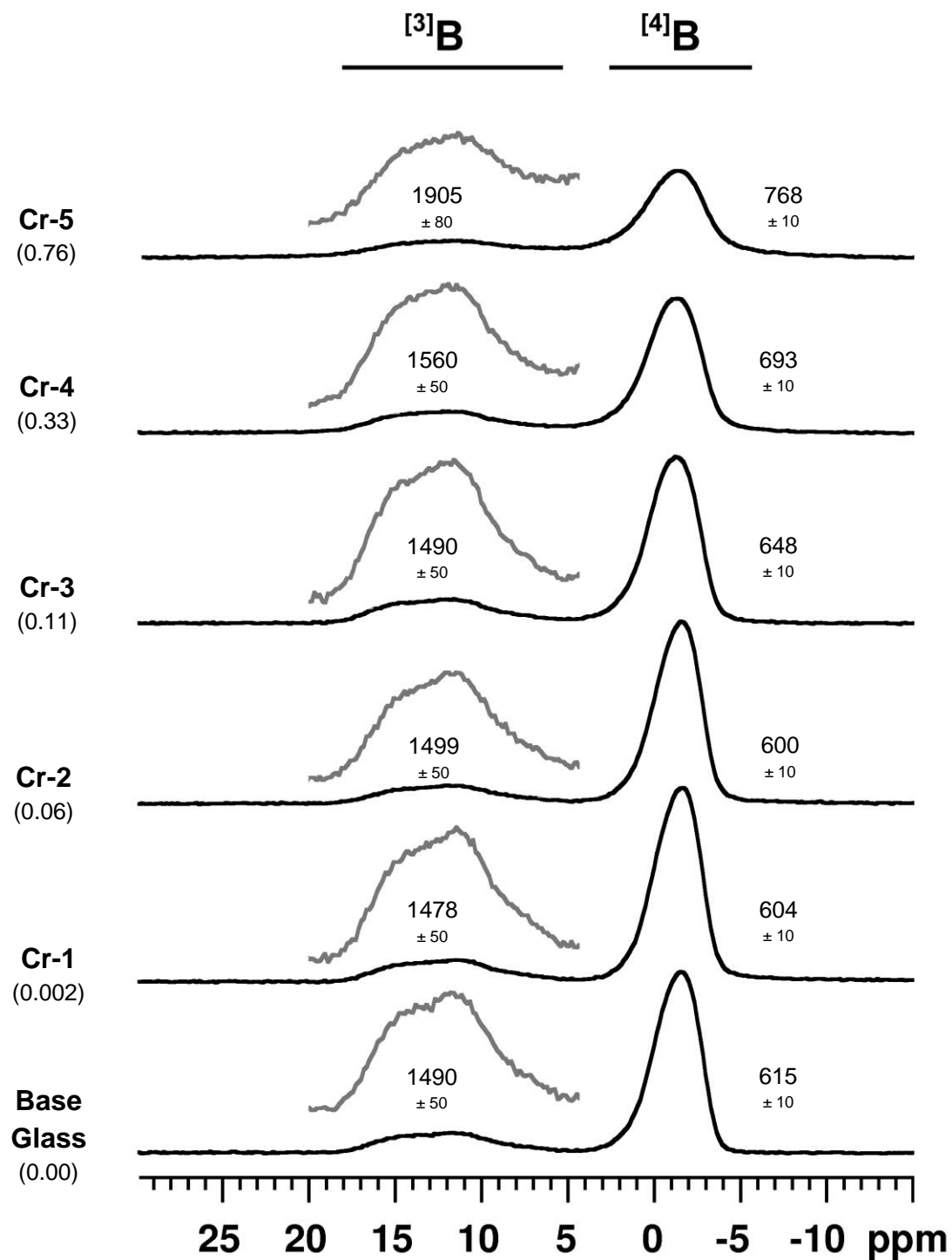


**Figure 6.6.** Experimental  $^{11}\text{B}$  MAS NMR spectra of base glass and chromium series glasses (mol%  $\text{Cr}_2\text{O}_3$  indicated above using the EMPA concentrations). FWHM values for the  $^{[3]}\text{B}$  and  $^{[4]}\text{B}$  sites are indicated beside their respective sites. The  $^{[3]}\text{B}$  site has been vertically enhanced to show the increase in breadth at higher  $\text{Cr}_2\text{O}_3$  loadings.

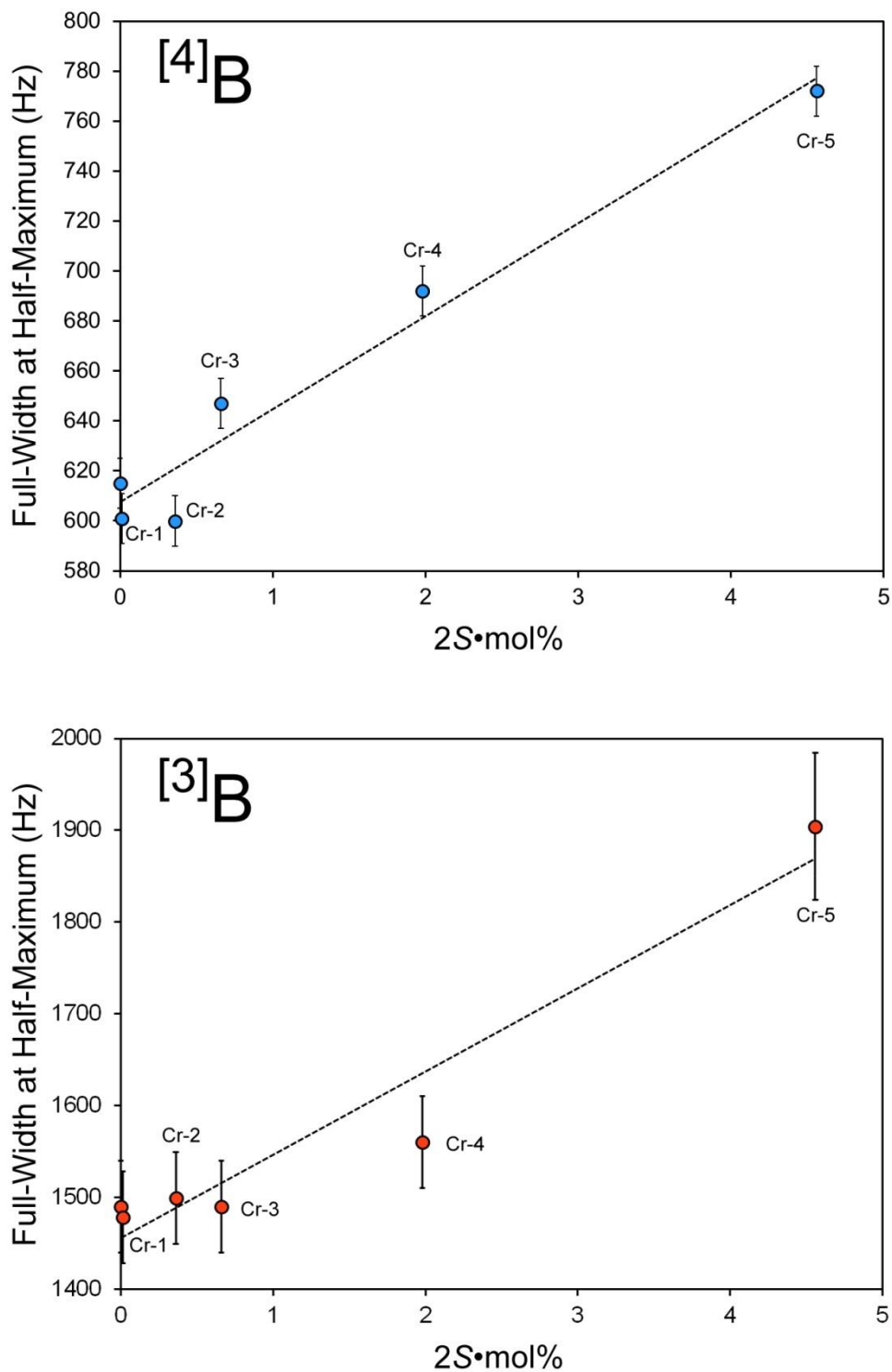


**Figure 6.7.** FWHM values for  $^{[3]}\text{B}$  (lower) and  $^{[4]}\text{B}$  (upper) as a function of  $\text{Cr}^{3+}$  content, expressed as the product of unpaired electron number ( $S$ ) and analysed  $\text{Cr}_2\text{O}_3$  mol% (from EMPA). For each, the unlabelled point near the origin is the five-component base glass.

and the mol% of the  $\text{Er}^{3+}$ ,  $\text{Yb}^{3+}$ , and  $\text{Nd}^{3+}$  dopant cations. Furthermore, equivalent levels of broadening were observed for  $^{13}\text{B}$  and  $^{14}\text{B}$ , and differences for each dopant cation could be attributed to their respective magnetic moments [94].

*$^{29}\text{Si}$  MAS NMR.*  $^{29}\text{Si}$  exhibits long spin-lattice relaxation times and displays particularly noticeable relaxation enhancement with the inclusion of paramagnetic centres (see Chapter 4, section 4.5, page 34). A saturation recovery pulse sequence, which consists of two  $90^\circ$  pulses separated by a variable time  $\tau$  (Figure 6.8), is used to perform  $T_1$  relaxation measurements on nuclei with long relaxation times. Relaxation of the five-component base glass was studied using 13  $\tau$  values over a range of 0.5-400 s, while the Cr glasses required ranges of 0.5-200 s (Cr-2 and Cr-3) and 0.1-20 s (Cr-4). Figure 6.9a shows the saturation recovery array for the five-component base glass, where the spectral intensity increases as a function of  $\tau$ . A fit of normalised integrated area against  $\tau$  generates a curve that can be fit as a logarithmic function to determine  $T_1$  (Figure 6.9b). The fully relaxed  $^{29}\text{Si}$  MAS NMR spectra of the five-component base glass and selected chromium glasses (Cr-2, Cr-3, and Cr-4) are depicted in Figure 6.10a, and show how the silicon environment remains unchanged with the addition of a small amount of chromium. Conversely, the corresponding  $T_1$  values show a drastic decrease (from 164 s in the base glass to 16 s in Cr-2) with even a small amount of added  $\text{Cr}_2\text{O}_3$  (Figure 6.10b), demonstrating how an equally informative  $^{29}\text{Si}$  MAS NMR spectrum is obtained in significantly less experimental time. Furthermore, the sensitivity of  $T_1$  to  $\text{Cr}_2\text{O}_3$  content provides a means to quantify the level of this additive within the glass for future samples. This method, however, would only be applicable for glasses of similar composition (Na-B-Si-Cs-Mo-Cr), as the inclusion of additional paramagnetic components would alter the  $T_1$  trend.

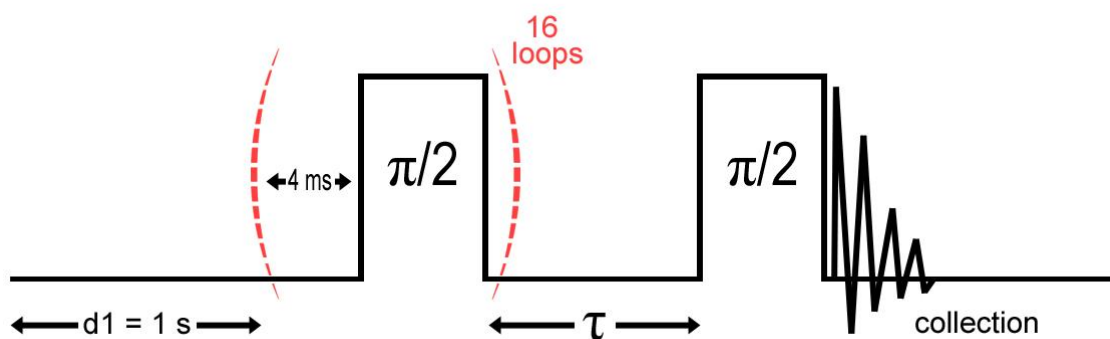


**Figure 6.8.** Graphical depiction of a *saturation recovery* pulse sequence. A series of  $90^\circ$  ( $\pi/2$ ) are used to “saturate” the spins, and a final  $90^\circ$  pulse is applied after a delay time ( $\tau$ ). The experiment is repeated for an array of  $\tau$  times (e.g. the five-component base glass was arrayed from 0.5 s to 400 s), resulting in an exponential increase in signal that is related to the relaxation time  $T_1$  (see Figure 6.9). This experiment allows  $T_1$  to be determined without having to wait the full relaxation time ( $5T_1$ ) for each scan; a recycle delay of 1 s was used for these experiments.

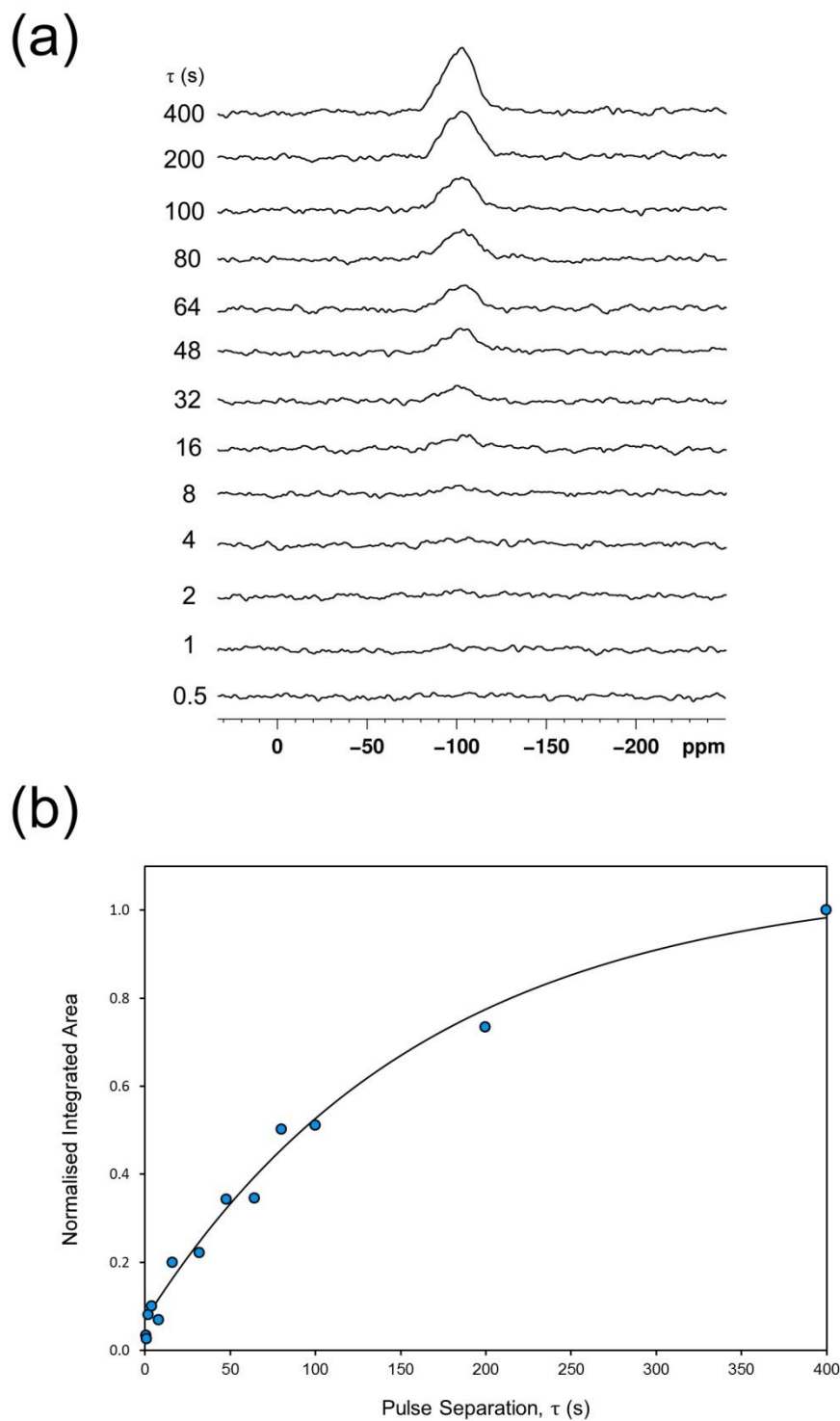


**Figure 6.9.** (a)  $^{29}\text{Si}$  MAS NMR spectra of the five-component base glass with changing saturation recovery pulse separation time  $\tau$ . (b) Determination of  $T_1$  based on a logarithmic fit of the normalised integrated area as a function of  $\tau$ .

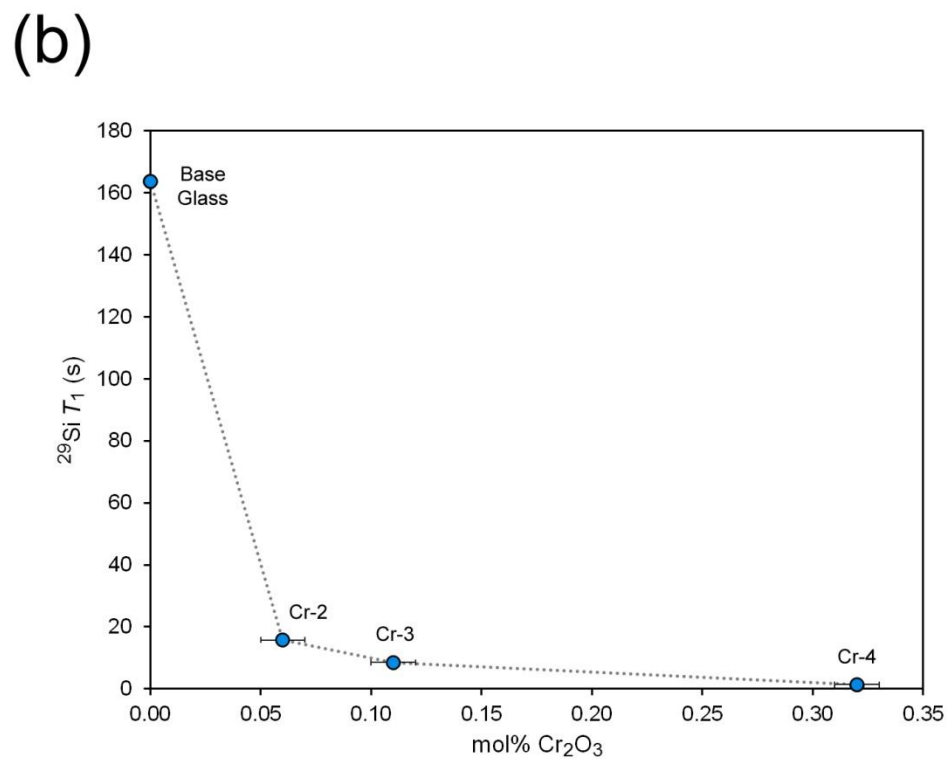
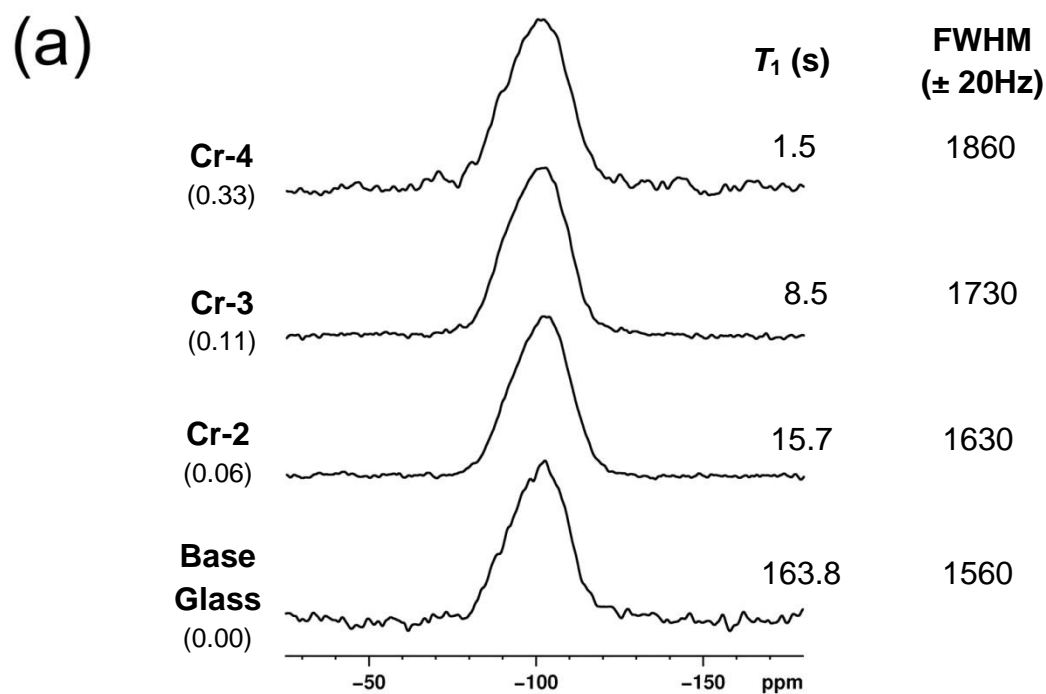


**Figure 6.10.** (a) Fully relaxed  $^{29}\text{Si}$  MAS NMR spectra of the five-component base glass and selected chromium series glasses. (b) Comparison of the  $T_1$  values as a function of chromium content (plotted using analysed  $\text{Cr}_2\text{O}_3$  concentrations from EMPA).

### 6.3.3 NMR of the Model Yellow Phases

<sup>133</sup>Cs MAS NMR. The advantage of hand-separating the crystalline deposits from the glass is the avoidance of the broad glassy NMR signal, allowing the spectrum to be more easily interpreted [16]. The <sup>133</sup>Cs MAS NMR spectra of samples YP1, YP3, and YP4 at 14.1 T are shown in Figure 6.11, where the distinct cesium environments of multiple crystalline components are identified. The integrated intensities are listed in Table 6.6, with noted spectral contributions from Cs<sub>2</sub>MoO<sub>4</sub> and Cs<sub>2</sub>CrO<sub>4</sub> along with the typical cesium-sodium molybdate compounds.

Interestingly, the signals corresponding to Cs<sub>3</sub>Na(MoO<sub>4</sub>)<sub>2</sub> do not appear as expected (two sharp resonances at 161 & -145 ppm), but rather as a distributed series of equally spaced peaks originating at each cesium site for this compound (separation of approximately 20 ppm from  $\delta_{\text{iso}}$ , Cs(2) at 161 ppm, and 13 ppm from  $\delta_{\text{iso}}$ , Cs(2) at -145 ppm). Due to the chemical similarity between Cr<sup>6+</sup> and Mo<sup>6+</sup>, this distribution of peaks is attributed to the random substitution of Cr<sup>6+</sup> for Mo<sup>6+</sup> according to the general formula Cs<sub>3</sub>Na(Mo<sub>1-x</sub>Cr<sub>x</sub>O<sub>4</sub>)<sub>2</sub>. The changing occupancies of these resonances with increasing chromium content (nominal mol% Cr<sub>2</sub>O<sub>3</sub>) reinforces that this anomaly is attributed to the incorporation of Cr into Cs<sub>3</sub>Na(MoO<sub>4</sub>)<sub>2</sub>. The distinct chemical shifts encountered as a result of this substitution represent discrete increases in the number of Cr atoms within the second coordination sphere of sites Cs(1) and Cs(2) of Cs<sub>3</sub>Na(MoO<sub>4</sub>)<sub>2</sub>, and reflect the sensitivity and diagnostic ability of the <sup>133</sup>Cs NMR chemical shift to local structure. Given that the crystal structure of Cs<sub>3</sub>Na(MoO<sub>4</sub>)<sub>2</sub> has not been reported in the literature, an inference must be made regarding the number of Mo sites available for substitution by Cr around each Cs site. A maximum of four unique resonances were observed for both Cs(1) and Cs(2), meaning that there are at least three neighbouring Mo atoms by which Cr substitution may occur to produce four combinations of Mo and Cr (Figure 6.12, page 89). It remains possible that the second-sphere

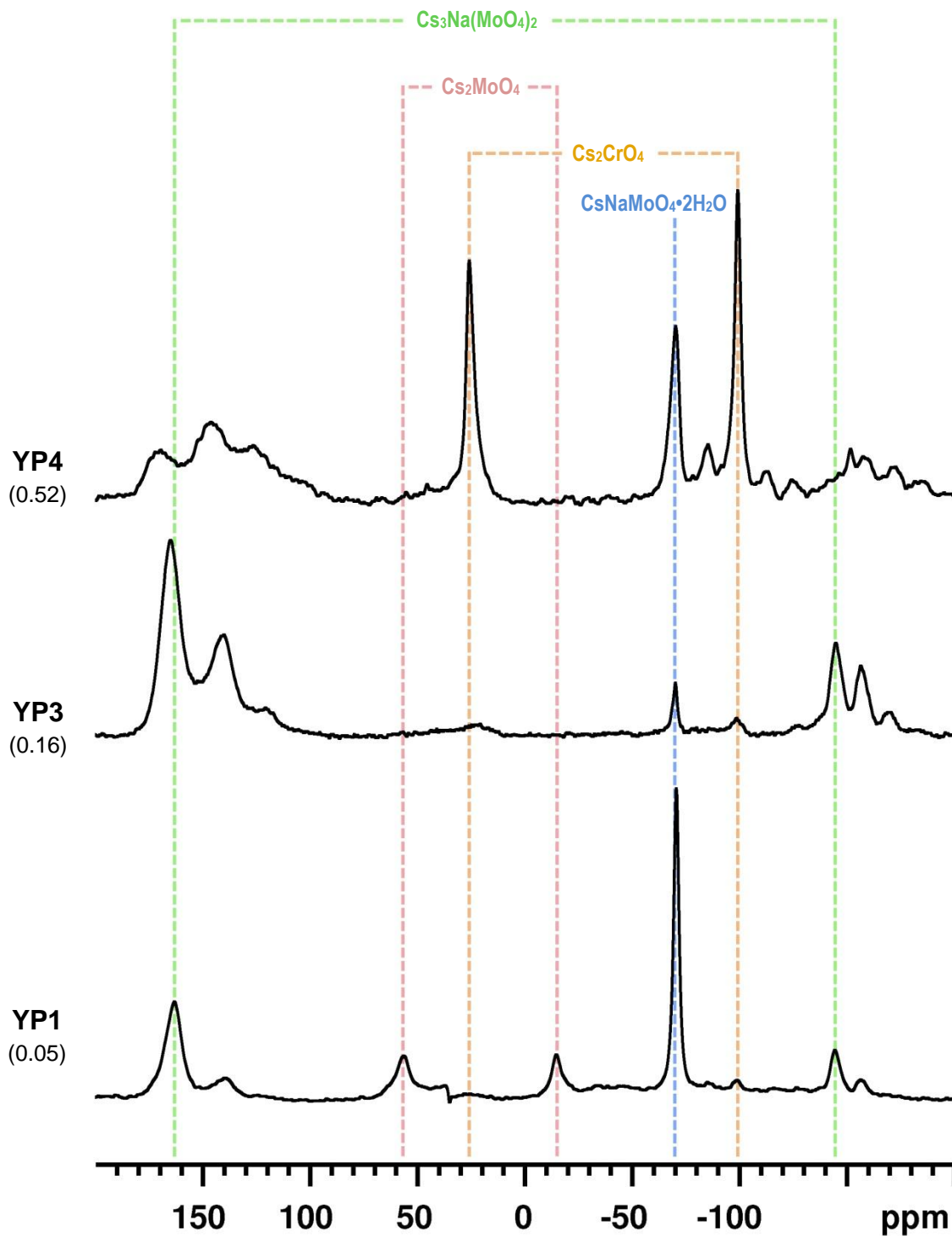


**Figure 6.11.**  $^{133}\text{Cs}$  MAS NMR spectra of hand-separated *yellow phase* deposits from glasses Cr-1r (YP1), Cr-3 (YP3), and Cr-4 (YP4) at 14.1 T. The chemical shifts of the labelled compounds are as follows:  $\text{Cs}_2\text{MoO}_4$  (55 & -16 ppm),  $\text{Cs}_2\text{CrO}_4$  (26 & -100 ppm),  $\text{CsNaMoO}_4 \cdot 2\text{H}_2\text{O}$  (-71 ppm), and  $\text{Cs}_3\text{Na}(\text{MoO}_4)_2$  (161 & -145 ppm). The nominal (glass) mol%  $\text{Cr}_2\text{O}_3$  is indicated in brackets for each sample.



**Table 6.6.** Integrated intensities (%) for  $^{133}\text{Cs}$  MAS NMR of model *yellow phase* samples

Sample	Component				
	$\text{Cs}_2\text{MoO}_4$	$\text{Cs}_2\text{CrO}_4$	$\text{CsNaMoO}_4 \cdot 2\text{H}_2\text{O}^{\text{a}}$	$\text{Cs}_3\text{Na}(\text{MoO}_4)_2^{\text{a}}$	Unknown
	(55 & 16 ppm)	(26 & -100 ppm)	(-71 ppm)	(161 & -145 ppm)	
<b>YP1</b>	22.4	-	33.1	44.5	-
	$\pm 0.3$	-	$\pm 0.5$	$\pm 0.4$	-
<b>YP3</b>	-	3.2	2.4	93.9	0.5
	-	$\pm 0.4$	$\pm 0.2$	$\pm 0.5$	$\pm 0.1$
<b>YP3</b> (21.1 T) <sup>b</sup>	6.8	6.0	35.6	49.0	2.6
	$\pm 0.2$	$\pm 2.2$	$\pm 2.5$	$\pm 0.6$	$\pm 0.2$
<b>YP4</b>	-	23.2	17.4	57.4	2.0
	-	$\pm 1.2$	$\pm 0.4$	$\pm 1.0$	$\pm 0.3$
<b>YP4</b> (21.1 T) <sup>b</sup>	-	37.6	29.5	32.3	0.6
	-	$\pm 1.0$	$\pm 0.4$	$\pm 1.1$	$\pm 0.2$

<sup>a</sup> Includes intensity of Cr substitution sites (see text).<sup>b</sup> See Figure 6.14 (page 93) for a comparison of the 14.1 and 21.1 T spectra.

environment of Cs contains more than three Mo atoms; for example, the reported crystal structure of  $\text{CsNaMoO}_4 \cdot 2\text{H}_2\text{O}$  contains four second-sphere Mo atoms (within 5 Å of Cs) [95]. Given the close relationship between  $\text{CsNaMoO}_4 \cdot 2\text{H}_2\text{O}$  and  $\text{Cs}_3\text{Na}(\text{MoO}_4)_2$  (i.e., their interconversion by hydration/dehydration, discussed below), it is reasonable to expect four Mo neighbours to each Cs site in the structure of the latter. Such an arrangement would generate five unique Mo and Cr combinations about Cs (Figure 6.12), implying that the fifth site (most Cr substituted) did not reach appreciable occupancy to be observed in the  $^{133}\text{Cs}$  MAS NMR spectra of these YP samples. Enhanced views of the YP  $^{133}\text{Cs}$  MAS NMR spectra are shown in Figure 6.13a, where the changes in the  $\text{Cs}_3\text{Na}(\text{MoO}_4)_2$  sites with increasing chromium content are highlighted. The peaks distributed about Cs(1) and Cs(2) are each assigned an identity using the integer notation “0” through “4” to represent the number of substituted Cr atoms in the second coordination sphere of Cs. By using a continuous statistical plot of the theoretical relative  $^{133}\text{Cs}$  NMR integrations as a function of Cr substitution (shown in Figure 6.13b for the four-cation model), the precise  $\text{Cs}_3\text{Na}(\text{Mo}_{1-x}\text{Cr}_x\text{O}_4)_2$  composition for each YP sample can be determined [16]. The binomial distribution that governs the relative probabilities has been previously described in the literature for NMR purposes [96,97], and the details for the three- and four-cation models employed here are detailed in the Appendix (page 141). Interpolations of the four-cation plot are depicted in Figure 6.13b, while the numerical results for the experimental determination and theoretical (three- and four-) cation models are summarised in Table 6.7. While there is little difference between the choice of cation model for the samples with lower  $\text{Cr}_2\text{O}_3$  content (YP1 and YP3), an appreciable difference is noted for YP4, where the four-cation model returns theoretical numbers that are in better agreement with the experimental values than the three-cation model (particularly for the “1 Cr” and “3 Cr” sites). In the solid-solution

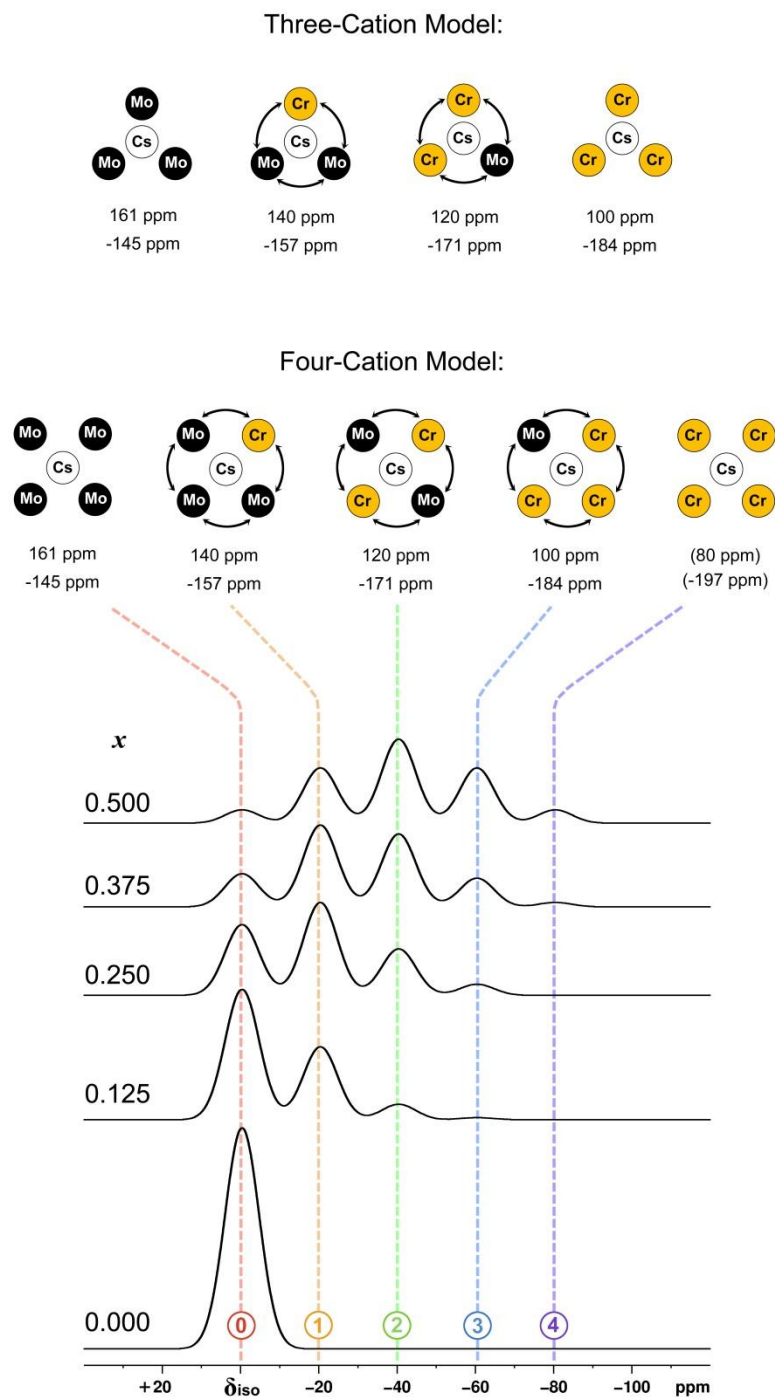


**Figure 6.12.** Stylised depiction of the three- and four-cation model environments (upper) used to evaluate the distribution of sites in the  $^{133}\text{Cs}$  MAS NMR signature of  $\text{Cs}_3\text{Na}(\text{Mo}_{1-x}\text{Cr}_x\text{O}_4)_2$  (arrows indicate that permutations are possible). A  $^{133}\text{Cs}$  NMR spectral simulation (lower) using the chemical shift separation (20 ppm) of the Cs(1) site is shown for the four-cation model with increasing Cr substitution ( $x$ ). The integer notation (“0” through “4”) represents the number of substituted Cr atoms.

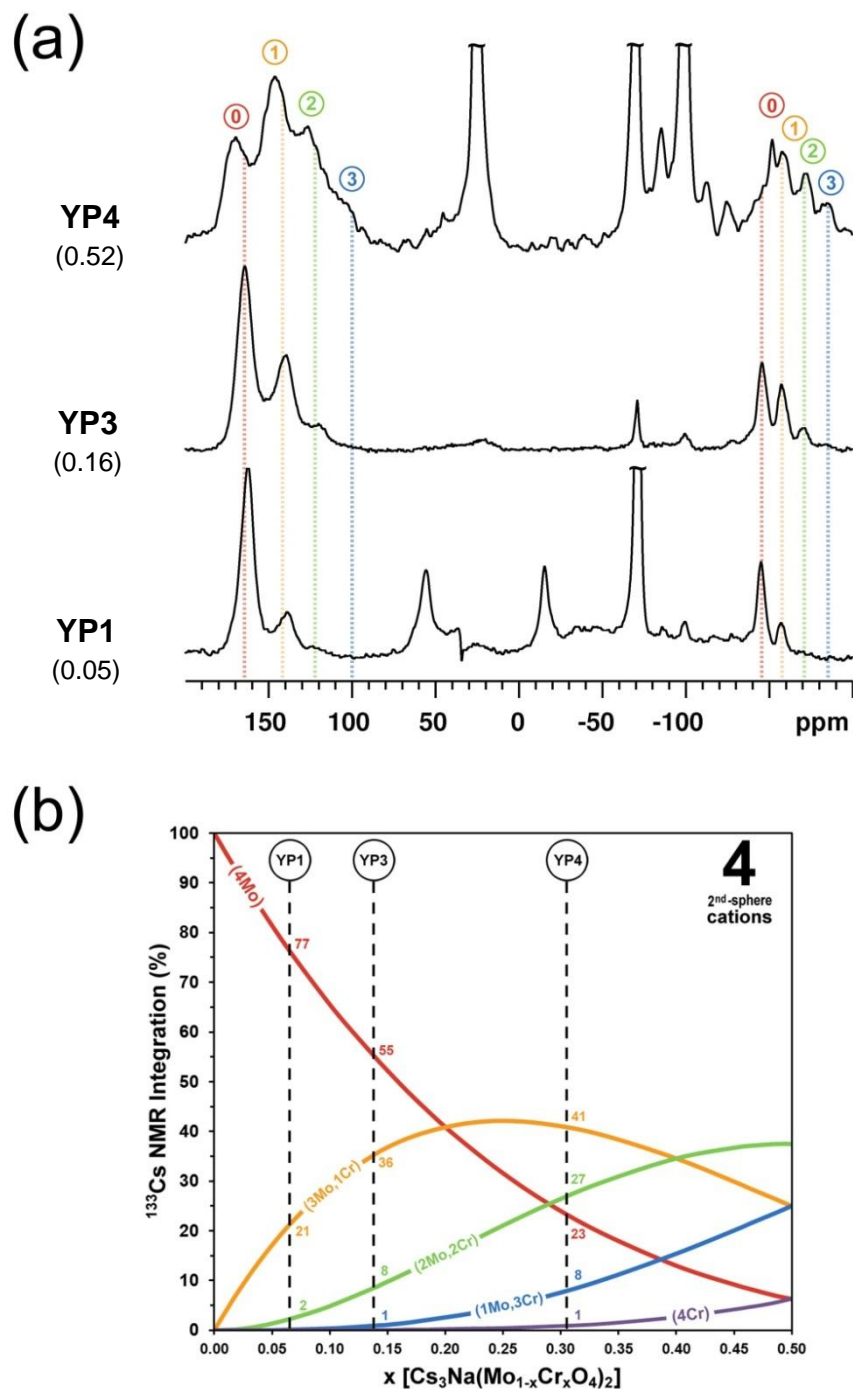


**Figure 6.13.** (a) Expanded view of the  $^{133}\text{Cs}$  MAS NMR spectra of model yellow phase samples for comparison of the substitution signals originating from  $\text{Cs}_3\text{Na}(\text{MoO}_4)_2$ . The approximate location of successive peaks have been marked and labelled according to the number of Cr atoms in the coordination sphere of each Cs site. (b) Substitution model assuming an environment of four second-sphere Mo atoms. The integrations of each YP can be interpolated to yield the composition ( $x$  value).

[16] – Reproduced by permission of the PCCP Owner Societies.

**Table 6.7.** Relative intensities (%) for  $^{133}\text{Cs}$  MAS NMR of the  $\text{Cs}_3\text{Na}(\text{Mo}_{1-x}\text{Cr}_x\text{O}_4)_2$  sites

Sample	Method	Substitution Site				
		4 Mo, 0 Cr	3 Mo, 1 Cr	2 Mo, 2 Cr	1 Mo, 3 Cr	0 Mo, 4 Cr
		(161 & -145 ppm)	(140 & -157 ppm)	(120 & -171 ppm)	(100 & -184 ppm)	(not observed)
<b>YP1</b>	Expt ( $\pm 2\%$ )	77	22	1	-	-
	3 Cat. ( $x = 0.08$ )	77	21	2	-	-
	4 Cat. ( $x = 0.07$ )	77	21	2	-	-
<b>YP3</b>	Expt ( $\pm 2\%$ )	55	37	8	-	-
	3 Cat. ( $x = 0.18$ )	55	36	8	1	-
	4 Cat. ( $x = 0.14$ )	55	36	8	1	0
<b>YP3</b> (21.1 T)	Expt ( $\pm 2\%$ )	48	42	10	-	-
	3 Cat. ( $x = 0.22$ )	48	40	11	1	-
	4 Cat. ( $x = 0.17$ )	47	39	12	2	0
<b>YP4</b>	Expt ( $\pm 2\%$ )	25	38	24	13	-
	3 Cat. ( $x = 0.38$ )	24	44	27	5	-
	4 Cat. ( $x = 0.31$ )	24	41	26	8	1
<b>YP4</b> (21.1 T)	Expt ( $\pm 2\%$ )	23	42	26	9	-
	3 Cat. ( $x = 0.38$ )	24	44	27	5	-
	4 Cat. ( $x = 0.31$ )	24	41	26	8	1

notation, the results of this interpretation can be written as  $\text{Cs}_3\text{Na}(\text{Mo}_{0.92}\text{Cr}_{0.08}\text{O}_4)_2$  (in YP1),  $\text{Cs}_3\text{Na}(\text{Mo}_{0.82}\text{Cr}_{0.18}\text{O}_4)_2$  (in YP3), and  $\text{Cs}_3\text{Na}(\text{Mo}_{0.62}\text{Cr}_{0.38}\text{O}_4)_2$  (in YP4) under the three-cation model, and  $\text{Cs}_3\text{Na}(\text{Mo}_{0.93}\text{Cr}_{0.07}\text{O}_4)_2$  (in YP1),  $\text{Cs}_3\text{Na}(\text{Mo}_{0.86}\text{Cr}_{0.14}\text{O}_4)_2$  (in YP3), and  $\text{Cs}_3\text{Na}(\text{Mo}_{0.69}\text{Cr}_{0.31}\text{O}_4)_2$  (in YP4) under the four-cation model.

The quantitative determination of Cr substitution in  $\text{Cs}_3\text{Na}(\text{MoO}_4)_2$  described above relies on accurate peak fitting of the obtained  $^{133}\text{Cs}$  MAS NMR spectra. As the series of  $\text{Cs}_3\text{Na}(\text{MoO}_4)_2$  peaks of the  $^{133}\text{Cs}$  MAS NMR spectra collected at 14.1 T are not fully resolved, two of the samples (YP3 and YP4) were sent to the National Ultrahigh-Field NMR Facility for Solids to test if collection at a higher magnetic field strength (21.1 T) would provide better resolution of the individual substitution sites. The resulting spectra, compared against the original 14.1 T data in Figure 6.14, show that no appreciable gain in resolution of the  $\text{Cs}_3\text{Na}(\text{Mo}_{1-x}\text{Cr}_x\text{O}_4)_2$  sites is obtained at 21.1 T. As second-order quadrupolar broadening (SOQB) scales with the inverse-square of the magnetic field strength, the breadth of the substituted peaks cannot be attributed to a distribution of quadrupolar coupling constants, otherwise the resolution would have been improved at 21.1 T. This reveals that the peak breadth is largely attributable to inherent disorder in the  $\text{Cs}_3\text{Na}(\text{Mo}_{1-x}\text{Cr}_x\text{O}_4)_2$  crystal structure, generating a distribution of chemical shifts for each site.

It should be noted that the 21.1 T spectrum of YP3 appears considerably different than that collected at 14.1 T, showing the presence of  $\text{Cs}_2\text{MoO}_4$  and larger fractions of both  $\text{Cs}_2\text{CrO}_4$  and  $\text{CsNaMoO}_4 \cdot 2\text{H}_2\text{O}$ . The integrated intensities of the 21.1 T  $^{133}\text{Cs}$  MAS NMR data are listed in Table 6.6, where significant changes from the 14.1 T integrated intensities of YP3 are the decrease in  $\text{Cs}_3\text{Na}(\text{MoO}_4)_2$  (93.9% to 49.0%) and corresponding increases in  $\text{CsNaMoO}_4 \cdot 2\text{H}_2\text{O}$  (2.4% to 35.6%),  $\text{Cs}_2\text{MoO}_4$  (0.0% to 6.8%), and  $\text{Cs}_2\text{CrO}_4$  (3.2% to 6.0%). Current studies in our

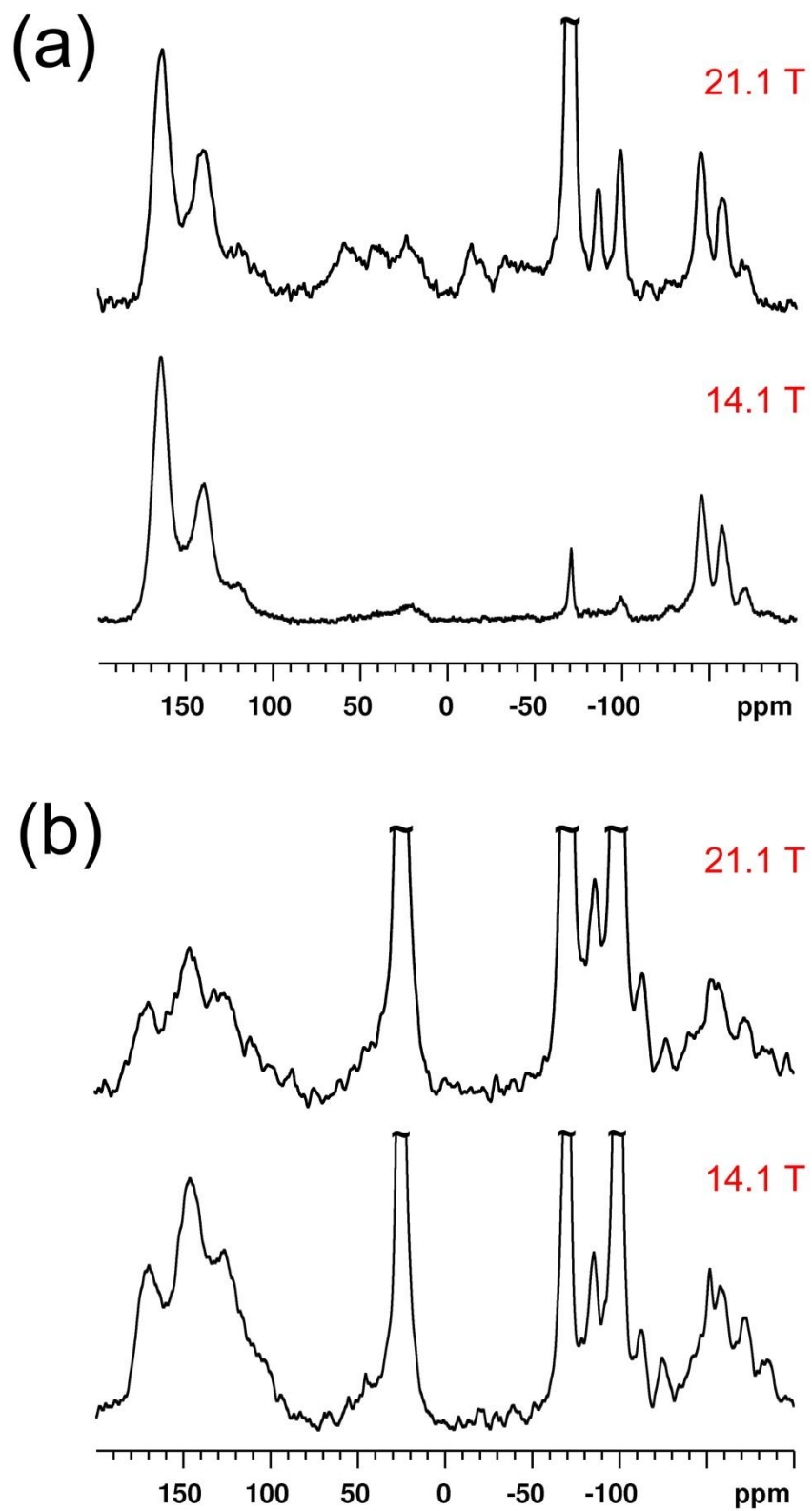
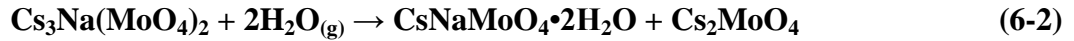


**Figure 6.14.**  $^{133}\text{Cs}$  MAS NMR spectra of (a) YP3 and (b) YP4 at 14.1 T and 21.1 T.

group (unpublished material) indicate that  $\text{Cs}_3\text{Na}(\text{MoO}_4)_2$  is highly sensitive to atmospheric hydration and readily converts to  $\text{CsNaMoO}_4 \cdot 2\text{H}_2\text{O}$  by an unknown mechanism. From previous spectral observations, this change is consistent with the uptake of  $\text{Na}_2\text{MoO}_4$  and  $\text{H}_2\text{O}$  (or alternatively  $\text{Na}_2\text{MoO}_4 \cdot 2\text{H}_2\text{O}$ ) to generate the more sodium-rich  $\text{CsNaMoO}_4 \cdot 2\text{H}_2\text{O}$  compound according to the following reversible scheme:



However, given the notable formation of  $\text{Cs}_2\text{MoO}_4$  by hydration of the YP3 sample prior to collection at 21.1 T, it would appear that an alternative mechanism exists whereby the Cs:Na ratio of 3:1 in  $\text{Cs}_3\text{Na}(\text{MoO}_4)_2$  is adjusted to 1:1 ( $\text{CsNaMoO}_4 \cdot 2\text{H}_2\text{O}$ ) by the release of  $\text{Cs}_2\text{MoO}_4$ :



where equation (6-2) is noted as a one-way reaction since the possibility of reversibility has not been tested. It is likely that dehydration subsequent to equation (6-2) could occur by the reverse of equation (6-1). However, the conversion of  $\text{Cs}_3\text{Na}(\text{MoO}_4)_2$  to  $\text{CsNaMoO}_4 \cdot 2\text{H}_2\text{O}$  exclusively by equation (6-2) would have produced more than 6.8% integrated intensity ( $^{133}\text{Cs}$  NMR) of  $\text{Cs}_2\text{MoO}_4$ , indicating that a combination of reactions (6-1) and (6-2) likely produced the resulting composition upon hydration. Additionally, the substitution of Cr into  $\text{Cs}_3\text{Na}(\text{MoO}_4)_2$  as  $\text{Cs}_3\text{Na}(\text{Mo}_{0.86}\text{Cr}_{0.14}\text{O}_4)_2$  (in YP3, four-cation model result) would explain the formation of  $\text{Cs}_2\text{CrO}_4$  in the 21.1 T spectrum (i.e., if the phase  $\text{Cs}_3\text{Na}(\text{Mo}_{1-x}\text{Cr}_x\text{O}_4)_2$  is used in equation (6-2)). Interpretation of the  $\text{Cs}_3\text{Na}(\text{Mo}_{1-x}\text{Cr}_x\text{O}_4)_2$  peaks in the  $^{133}\text{Cs}$  MAS NMR spectrum of YP3 at 21.1 T by the four-cation model yields a phase composition of  $\text{Cs}_3\text{Na}(\text{Mo}_{0.83}\text{Cr}_{0.17})$ , indicating that the non-substituted molybdate units more readily convert to  $\text{CsNaMoO}_4 \cdot 2\text{H}_2\text{O}$  than do the Cr-substituted units. This assertion also verifies why the peaks adjacent to  $\text{CsNaMoO}_4 \cdot 2\text{H}_2\text{O}$  (at



-87 ppm and -99 ppm, the latter obscured by  $\text{Cs}_2\text{CrO}_4$ ), presumed to be Cr-substitution peaks according to  $\text{CsNa}(\text{Mo}_{1-x}\text{Cr}_x)\text{O}_4 \cdot 2\text{H}_2\text{O}$ , do not appear in a statistical manner.

<sup>23</sup>Na MAS NMR. The <sup>23</sup>Na MAS NMR spectra of YP1, YP3, and YP4 at 14.1 T are shown in Figure 6.15, each composed of overlapping quadrupolar shapes of the various sodium sites. The integrated intensities of the simulated spectra are listed in Table 6.8 (page 99), with the largest components being  $\text{Na}_2\text{MoO}_4$  (between 60 and 95% in these spectra) and  $\text{Na}_2\text{MoO}_4 \cdot 2\text{H}_2\text{O}$  (19.8% in YP4). As expected from their observation in the <sup>133</sup>Cs MAS NMR spectra,  $\text{Cs}_3\text{Na}(\text{MoO}_4)_2$  and  $\text{CsNaMoO}_4 \cdot 2\text{H}_2\text{O}$  were detected in <sup>23</sup>Na MAS NMR of YP1 and YP4, while YP3 only showed evidence of the former due to the small concentration of  $\text{CsNaMoO}_4 \cdot 2\text{H}_2\text{O}$  in this sample (only 2.4% in <sup>133</sup>Cs MAS NMR at 14.1 T, which becomes insignificant compared to the large proportion of  $\text{Na}_2\text{MoO}_4$ ).

Several spectral features in the 14.1 T data, including the low-intensity shoulder around -20 ppm and intensity in the -9 ppm region, suggest that more sites are present than the sodium- and cesium-sodium molybdates already described. For this reason, samples YP3 and YP4 were collected at 21.1 T to explore the changes in resolution of the quadrupolar patterns based on the reduction of SOQB with higher magnetic field strength. The high-field data, shown in Figure 6.16 along with spectral simulations, reveal the disadvantageous overlap of the  $\text{Na}_2\text{MoO}_4$ ,  $\text{Na}_2\text{MoO}_4 \cdot 2\text{H}_2\text{O}$ , and  $\text{CsNaMoO}_4 \cdot 2\text{H}_2\text{O}$  patterns around the -1.5 ppm region. However, the resolution between  $\text{Na}_2\text{MoO}_4$  and the Na(2) site of  $\text{Na}_2\text{MoO}_4 \cdot 2\text{H}_2\text{O}$  is improved at 21.1 T, as the high-frequency discontinuity of the latter (around 3 ppm) can be partially identified in the 21.1 T spectrum of YP4. Additionally, the 21.1 T spectrum provides better resolution of the two sites of  $\text{Na}_2\text{Mo}_2\text{O}_7$  [98-100]; Na(1) with  $C_Q = 1.44 \pm 0.01$  MHz,  $\eta = 0.53 \pm 0.03$ , and  $\delta_{\text{iso}} = -5.9 \pm 0.02$  ppm, and Na(2) with  $C_Q = 2.57 \pm 0.02$  MHz,  $\eta = 0.16 \pm 0.02$ , and  $\delta_{\text{iso}} = -9.9 \pm 0.1$  ppm. As the

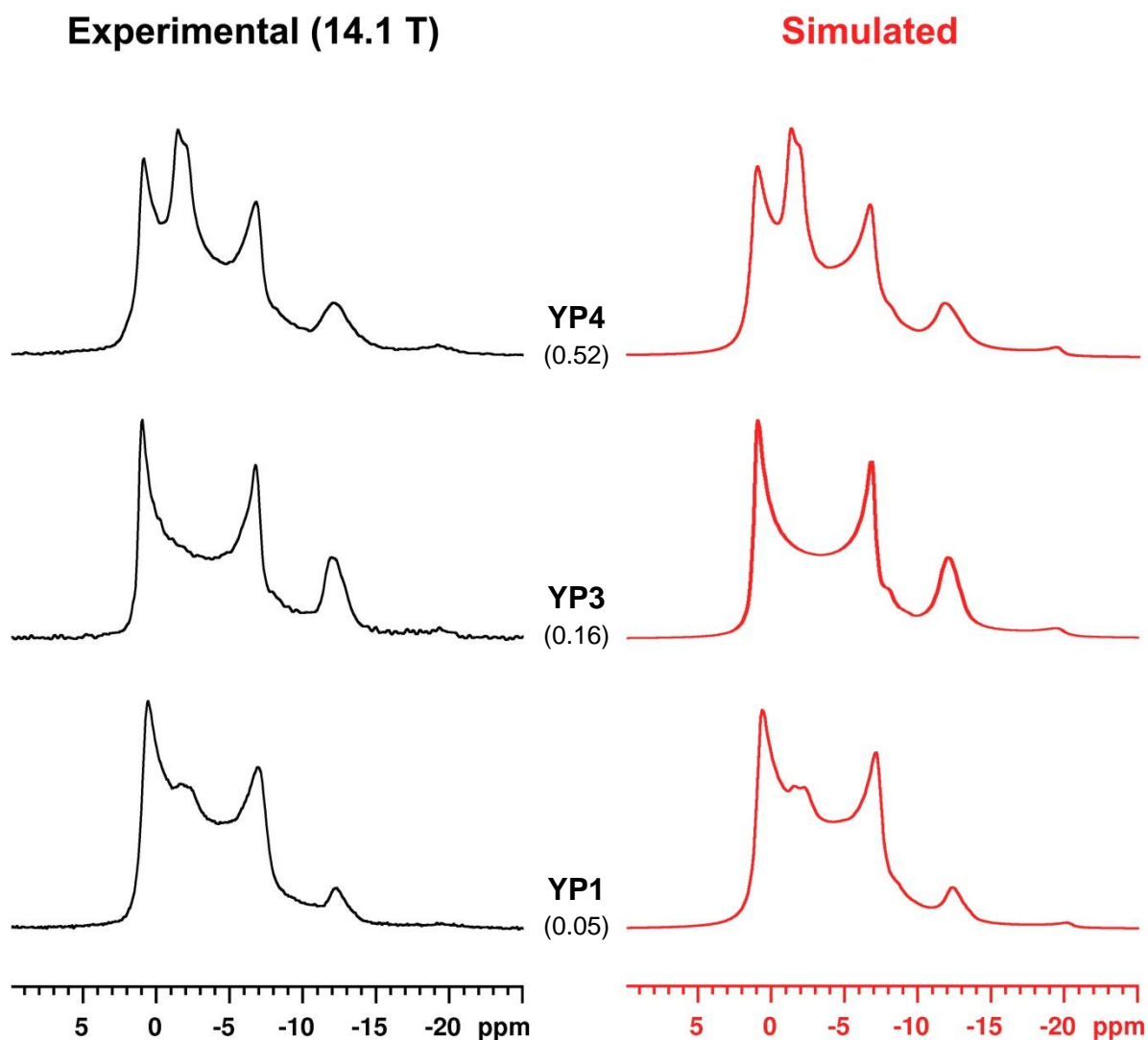


**Figure 6.15.** Experimental (left) and simulated (right)  $^{23}\text{Na}$  MAS NMR spectra of hand-separated YP1, YP3, and YP4 at 14.1 T. The prominent quadrupolar pattern is  $\text{Na}_2\text{MoO}_4$  ( $C_Q = 2.59$  MHz,  $\eta = 0$ ,  $\delta_{\text{iso}} = 3.2$  ppm). The nominal mol%  $\text{Cr}_2\text{O}_3$  is indicated in brackets for each.

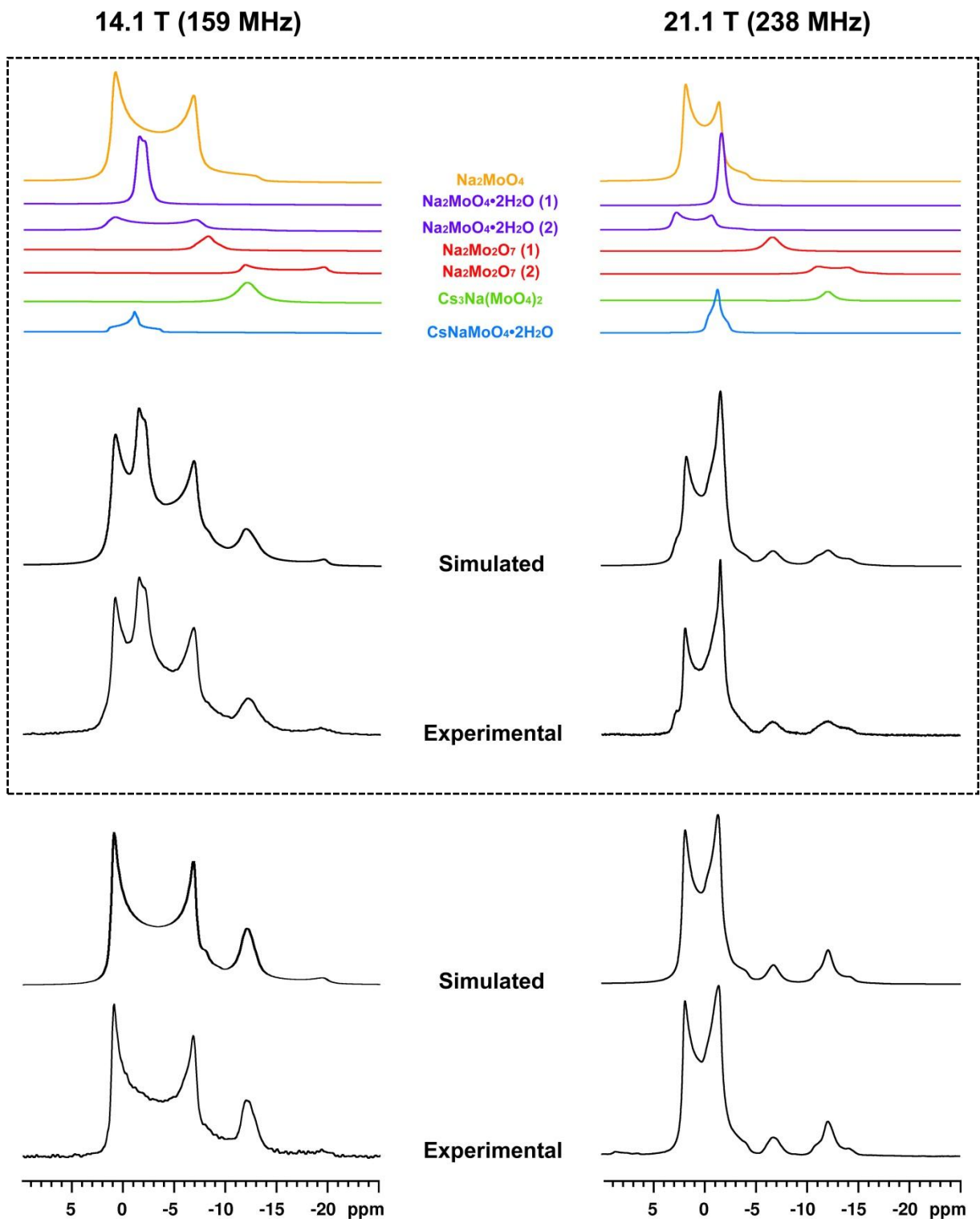


**Figure 6.16.** Experimental and simulated  $^{23}\text{Na}$  MAS NMR spectra of YP3 (lower) and YP4 (upper) at 14.1 T (left) and 21.1 T (right). The deconvolution of seven unique sites (top) is for YP4, where the reduction in SOQB at 21.1 T causes the patterns to overlap in a different manner.

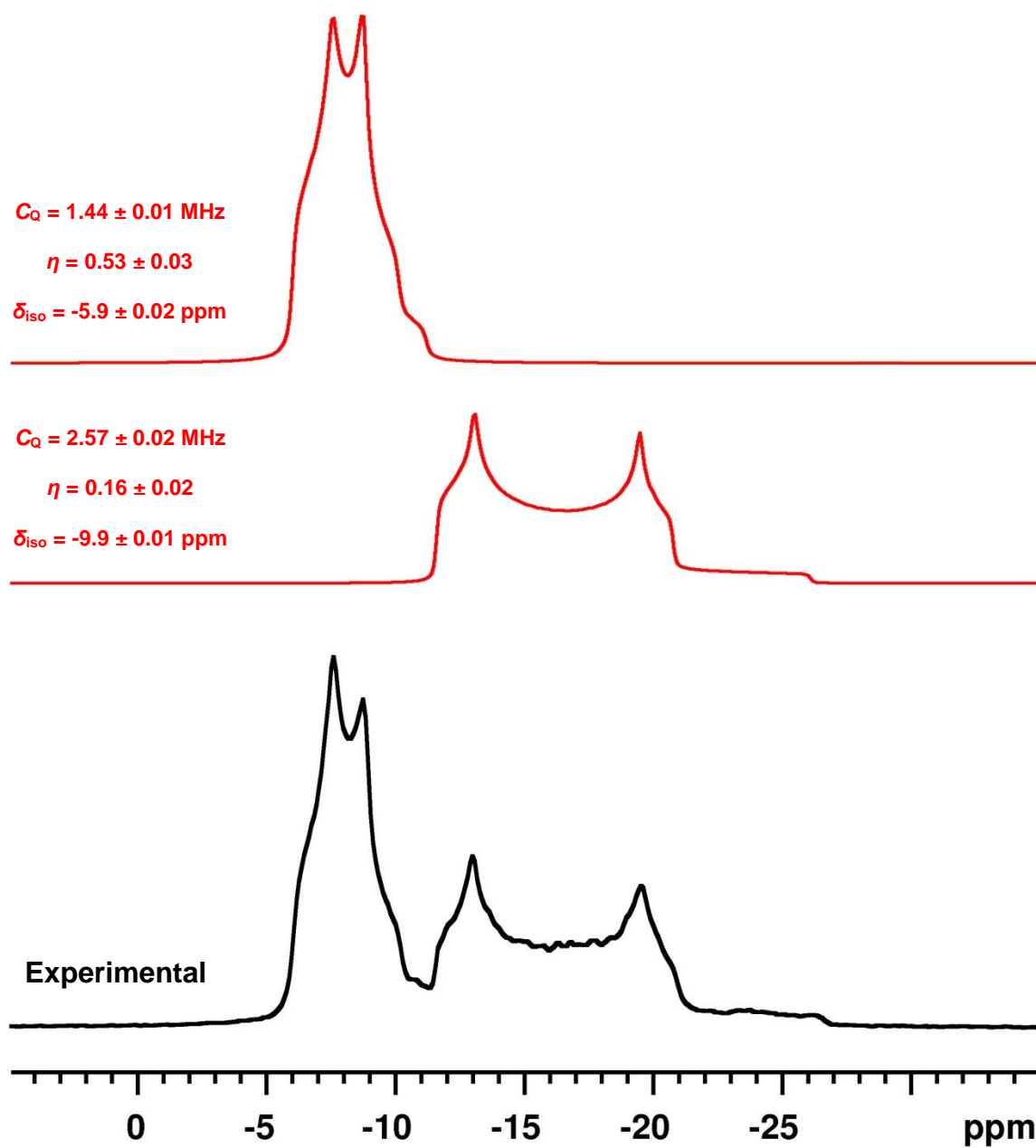


**Figure 6.17.** Experimental  $^{23}\text{Na}$  MAS NMR spectrum of  $\text{Na}_2\text{Mo}_2\text{O}_7$  with spectral simulations of its two unique sites.

**Table 6.8.** Integrated intensities (%) for  $^{23}\text{Na}$  MAS NMR of model *yellow phase* samples

Sample	Component				
	$\text{Na}_2\text{MoO}_4$	$\text{Na}_2\text{MoO}_4 \cdot 2\text{H}_2\text{O}$	$\text{Na}_2\text{Mo}_2\text{O}_7$	$\text{CsNaMoO}_4 \cdot 2\text{H}_2\text{O}$	$\text{Cs}_3\text{Na}(\text{MoO}_4)_2$
<b>YP1</b>	84.6	3.0	5.5	4.7	2.2
	$\pm 0.8$	$\pm 0.3$	$\pm 0.7$	$\pm 0.3$	$\pm 0.2$
<b>YP3</b>	81.3	-	10.0	-	8.7
	$\pm 1.0$	-	$\pm 0.3$	-	$\pm 0.3$
<b>YP3</b> (21.1 T)	75.2	-	8.8	10.4	5.6
	$\pm 0.5$	-	$\pm 0.2$	$\pm 0.4$	$\pm 0.1$
<b>YP4</b>	60.9	19.8	7.7	6.3	5.3
	$\pm 1.3$	$\pm 3.6$	$\pm 0.4$	$\pm 2.6$	$\pm 0.2$
<b>YP4</b> (21.1 T)	54.9	23.0	10.6	8.8	2.7
	$\pm 0.4$	$\pm 0.9$	$\pm 0.9$	$\pm 0.6$	$\pm 0.3$

NMR parameters of  $\text{Na}_2\text{Mo}_2\text{O}_7$  have not been reported in the literature, the assignment of these sites was determined by collecting a  $^{23}\text{Na}$  MAS NMR spectrum of a prepared sample of  $\text{Na}_2\text{Mo}_2\text{O}_7$  at 14.1 T (Figure 6.17, page 98). The structure of  $\text{Na}_2\text{Mo}_2\text{O}_7$  consists of chains of  $\text{MoO}_6$  and  $\text{MoO}_4$  moieties [98, 99], suggesting how the two sodium environments would be expected to produce very different quadrupolar parameters in  $^{23}\text{Na}$  NMR. Integrated intensities of the 21.1 T spectral fittings (Table 6.8) confirm the conversion of  $\text{Cs}_3\text{Na}(\text{MoO}_4)_2$  to  $\text{CsNaMoO}_4 \cdot 2\text{H}_2\text{O}$  (as postulated on the basis of the  $^{133}\text{Cs}$  NMR data), however the changes are less apparent due to the predominance of  $\text{Na}_2\text{MoO}_4$  [16].

Given the spectral complexity of these heterogeneous samples (showing the presence of seven unique sites in the one-dimensional  $^{23}\text{Na}$  MAS NMR spectra), a  $^{23}\text{Na}$  MQMAS spectrum of YP4 was collected to enhance spectral resolution using two dimensions (Figure 6.18). Most notably, the patterns of  $\text{Na}_2\text{MoO}_4$ ,  $\text{Na}_2\text{MoO}_4 \cdot 2\text{H}_2\text{O}$ , and  $\text{CsNaMoO}_4 \cdot 2\text{H}_2\text{O}$ , which existed with significant overlap in one-dimensional collections at 14.1 T and 21.1 T, are resolved using MQMAS. The slight chemical shift offset of  $\text{Na}_2\text{MoO}_4$  and Na(2) of  $\text{Na}_2\text{MoO}_4 \cdot 2\text{H}_2\text{O}$ , which otherwise contain very similar quadrupolar parameters (i.e.,  $C_Q$  and  $\eta$ ), is noticeable along with the offset of  $\text{CsNaMoO}_4 \cdot 2\text{H}_2\text{O}$  and Na(1) of  $\text{Na}_2\text{MoO}_4 \cdot 2\text{H}_2\text{O}$ , exhibiting how these positions present difficulty in one-dimensional spectral fitting. Lastly, the two-dimensional pattern of  $\text{Cs}_3\text{Na}(\text{MoO}_4)_2$  shows evidence of structural disorder (appears at a diagonal rather than horizontal; broadening in two dimensions [101,102]), revealing that  $^{23}\text{Na}$  NMR is also sensitive to the substitution of Cr in this compound. Unfortunately, the MQMAS pulse sequence confers preferential excitation depending on the quadrupolar parameters, so the two-dimensional spectrum is not quantitative. Nevertheless, verification of the number of sodium sites and their relative positions strengthens the quantitative determinations made from the one-dimensional data.

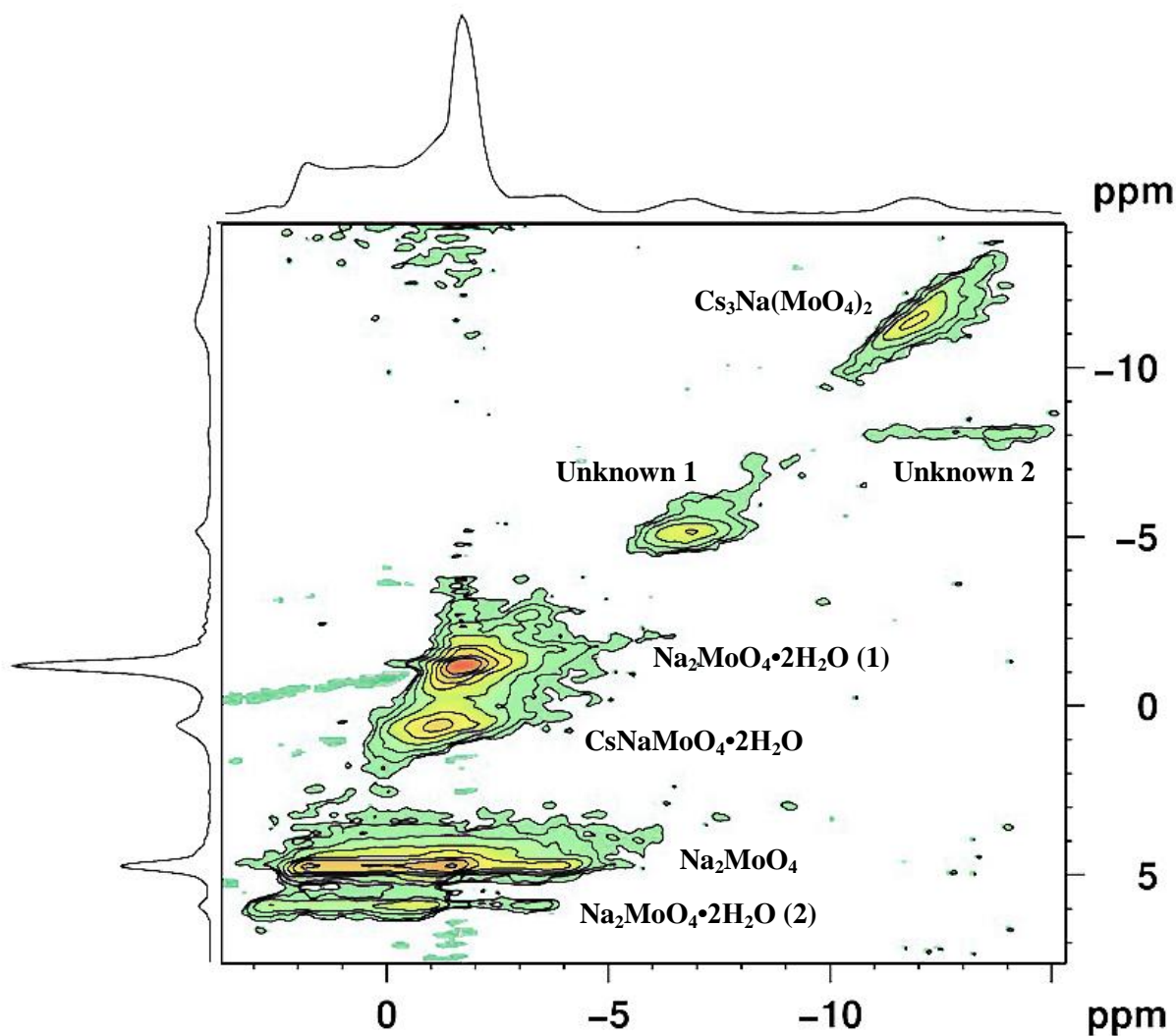


**Figure 6.18.**  $^{23}\text{Na}$  MQMAS NMR of YP4 at 21.1 T. The seven unique sodium sites (see Figure 6.16 and Table 6.8 for fit details) are resolved in two dimensions.

$^{95}\text{Mo}$  MAS NMR. The  $^{95}\text{Mo}$  MAS NMR spectra of YP1, YP3, and YP4 at 14.1 T are shown in Figure 6.19. As stated in previous sections, overlap of the narrow  $\text{Na}_2\text{MoO}_4$  ( $\delta_{\text{iso}} = -33.5$  ppm) and  $\text{CsNaMoO}_4 \cdot 2\text{H}_2\text{O}$  ( $\delta_{\text{iso}} = -32$  ppm) resonances precludes accurate deconvolution of these sites, however the majority of the peak is likely attributed to the former if the  $^{23}\text{Na}$  MAS NMR integrated intensities are taken into consideration. The signal at -15 ppm is attributed to  $\text{Cs}_3\text{Na}(\text{MoO}_4)_2$ , and is responsible for 17% and 9% of the  $^{95}\text{Mo}$  signal in YP3 and YP4, respectively, in accordance with its relative levels in the  $^{133}\text{Cs}$  and  $^{23}\text{Na}$  NMR results.

#### 6.3.4 Compositional Analyses of the Model Yellow Phases

To evaluate the composition of a heterogeneous model *yellow phase* sample, a sufficiently large piece of YP4 (the sample for which the most hand-separated material was recovered) was analysed using EMPA. The results of a 15-spot collection are shown in Table 6.9, where the variability between each measurement reflects the homogeneous nature of this material. In particular, the variation is evident in the mol% of  $\text{Cs}_2\text{O}$ , which has the largest standard deviation (relatively) of any component. However, it is clear that the largest contributions are from  $\text{Na}_2\text{O}$  and  $\text{MoO}_3$ , which agrees with the dominant fraction of  $\text{Na}_2\text{MoO}_4$  (and  $\text{Na}_2\text{MoO}_4 \cdot 2\text{H}_2\text{O}$ ) observed in the  $^{23}\text{Na}$  MAS NMR spectra (14.1 T and 21.1 T) of YP4.

In section 6.3.1 it was demonstrated that the escaped molar fractions of  $\text{Na}_2\text{O}$ ,  $\text{Cs}_2\text{O}$ ,  $\text{MoO}_3$ , and  $\text{Cr}_2\text{O}_3$  caused the analysed glass-phase compositions ( $\text{SiO}_2$ -normalised) to sum between 86 and 97% rather than 100%. A rudimentary estimate of the separated *yellow phase* composition may be obtained by normalising the residual 3 to 14% of components that were unaccounted for in analysis of the glass phase, however the volatilisation of  $\text{Cs}_2\text{O}$  must be considered as some fraction of this component is lost during heating. An example of this “composition by difference” method is detailed in Table 6.10 using YP4 (Cr-4), where it was



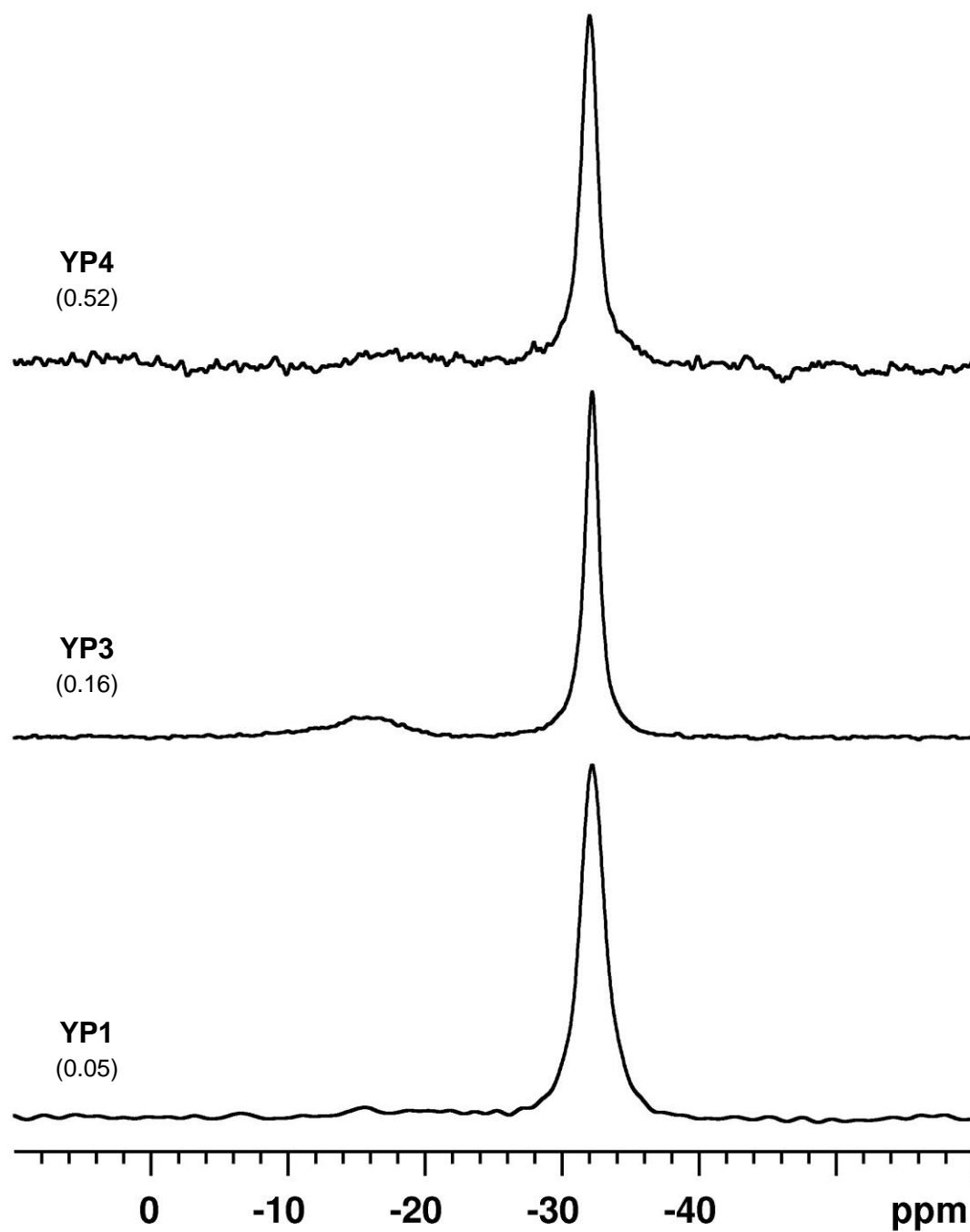


**Figure 6.19.**  $^{95}\text{Mo}$  MAS NMR spectra of YP1, YP3, and YP4 at 14.1 T. The nominal mol%  $\text{Cr}_2\text{O}_3$  is indicated in brackets for each.

**Table 6.9.** Compositional determination of YP4 by EMPA (in mol%)

<b>Spot</b>	<b>Na<sub>2</sub>O</b>	<b>Cs<sub>2</sub>O</b>	<b>MoO<sub>3</sub></b>	<b>Cr<sub>2</sub>O<sub>3</sub></b>
<b>1</b>	39.31	9.49	47.13	4.08
<b>2</b>	40.98	10.87	42.74	5.41
<b>3</b>	44.47	5.45	45.81	4.27
<b>4</b>	37.59	12.21	44.87	5.33
<b>5</b>	29.87	20.19	44.35	5.58
<b>6</b>	39.51	13.71	41.47	5.30
<b>7</b>	43.55	7.90	44.26	4.29
<b>8</b>	34.45	11.21	49.42	4.92
<b>9</b>	34.37	12.80	47.34	5.49
<b>10</b>	46.75	4.26	46.22	2.77
<b>11</b>	38.80	13.56	42.53	5.11
<b>12</b>	42.79	8.73	44.44	4.04
<b>13</b>	30.78	17.17	45.09	6.96
<b>14</b>	38.90	10.03	46.62	4.45
<b>15</b>	41.07	12.59	42.55	3.79
<b>Average</b>	<b>38.88</b>	<b>11.34</b>	<b>44.99</b>	<b>4.79</b>
<b>Std. Deviation</b>	<b>± 4.84</b>	<b>± 4.11</b>	<b>± 2.16</b>	<b>± 0.99</b>

**Table 6.10.** Example of YP4 “composition by difference” from parent glass Cr-4

Method	SiO <sub>2</sub>	B <sub>2</sub> O <sub>3</sub>	Na <sub>2</sub> O	Cs <sub>2</sub> O	MoO <sub>3</sub>	Cr <sub>2</sub> O <sub>3</sub>	Sum
<b>Cr-4</b> Nominal	60.45	17.26	15.50	3.71	2.56	0.52	100.00
<b>Cr-4</b> EMPA (normSiO <sub>2</sub> )	60.45	17.92	14.21	2.31	0.60	0.32	95.80
<b>Difference</b> <sup>a</sup>	(0.00)	(-0.64)	<b>1.29</b>	<b>1.40</b>	<b>1.96</b>	<b>0.20</b>	4.20
			↓	↓	↓	↓	
<b>YP4</b> calc <sup>b</sup>	-	-	<b>27</b>	<b>29</b>	<b>40</b>	<b>4</b>	100
<b>YP4</b> calc (25% Cs vol) <sup>c</sup>	-	-	<b>33</b>	<b>12</b>	<b>50</b>	<b>5</b>	100
			± 4	± 4	± 3	± 1	
<b>YP4</b> EMPA	-	-	<b>38.88</b>	<b>11.34</b>	<b>44.99</b>	<b>4.79</b>	100.00
			± 4.84	± 4.11	± 2.16	± 0.99	

<sup>a</sup> “Difference” = “Cr-4<sub>Nominal</sub>” – “Cr-4<sub>EMPA (normSiO<sub>2</sub>)</sub>”.

<sup>b</sup> “YP4<sub>calc</sub>” = Normalisation of the “Difference” row to 100%, excluding B<sub>2</sub>O<sub>3</sub>, without consideration of Cs<sub>2</sub>O volatilisation.

<sup>c</sup> 25% Cs<sub>2</sub>O volatilisation was applied to nominal value and a new difference was taken and normalised.

determined that a correction factor assuming 25%  $\text{Cs}_2\text{O}$  volatilisation (i.e., 0.93 mol% of the nominal 3.71 mol%  $\text{Cs}_2\text{O}$ ) was required to establish agreement between the calculated composition (“difference”) and the direct EMPA measurement of the crystalline YP4 sample. This level of volatilisation is in accord with previous observations of  $\text{Cs}_2\text{O}$  behaviour at high temperatures in borosilicate glasses [18,68].

Alternatively, the integrated intensities from the  $^{133}\text{Cs}$  and  $^{23}\text{Na}$  MAS NMR have been used as another method to determine the model *yellow phase* composition. The integrated intensities of  $\text{CsNaMoO}_4 \cdot 2\text{H}_2\text{O}$  and  $\text{Cs}_3\text{Na}(\text{MoO}_4)_2$  (i.e., compounds that are common to both the  $^{133}\text{Cs}$  and  $^{23}\text{Na}$  NMR spectra) are used to equate the multinuclear data. The derived mol% oxide composition is subject to errors based on peak-fitting of the NMR spectra and the agreement between  $^{133}\text{Cs}$  and  $^{23}\text{Na}$  NMR data. Table 6.11 summarises the various compositional determinations (i.e., direct EMPA, “composition by difference”, and NMR) of the *yellow phase* samples. For YP4, the compositions determined by difference (from Cr-4) and NMR reasonably approximate the direct EMPA measurement, with the latter showing better agreement. Being the most thoroughly characterised sample, an accurate description of phase separation can be made for glass Cr-4 (YP4), where its final disposition after phase separation and  $\text{Cs}_2\text{O}$  volatilisation is depicted in Table 6.12. For YP3, good agreement is observed between the LA-ICP-MS (difference from Cr-3 spot measurement) and NMR compositions, while the EMPA composition (by difference from Cr-3) largely disagrees, showing lower  $\text{Na}_2\text{O}$  content and higher  $\text{MoO}_3$  content than the other two methods. No change in the volatilisation factor for this sample (32%  $\text{Cs}_2\text{O}$  volatilisation is shown) could yield markedly improved agreement of the EMPA trial. A possible explanation for this disagreement may be an over-correction of  $\text{Na}_2\text{O}$  content by the linear correction method employed experimentally (see section 6.2.2), which would report larger  $\text{Na}_2\text{O}$  content in the glass, thus lower content when the difference from the nominal composition

**Table 6.11.** Compositional determinations of model *yellow phase* samples

Sample	Method	Na <sub>2</sub> O	Cs <sub>2</sub> O	MoO <sub>3</sub>	Cr <sub>2</sub> O <sub>3</sub>
<b>YP1<sup>a</sup></b>	NMR <sup>b</sup>	42	9	48	< 1
		± 3	± 3	± 3	± 1
<b>YP3</b>	EMPA <sup>c</sup>	18	12	68	2
		± 4	± 4	± 3	± 1
	LA-ICP-MS <sup>d</sup>	47	11	40	2
		± 4	± 4	± 3	± 1
	NMR <sup>e</sup>	42	12	45	1
		± 3	± 3	± 2	± 1
<b>YP4</b>	EMPA <sup>f</sup>	38.88	11.34	44.99	4.79
		± 4.84	± 4.11	± 2.16	± 0.99
	EMPA <sup>g</sup>	33	12	50	5
		± 4	± 4	± 3	± 1
	NMR <sup>e</sup>	42	12	43	3
		± 3	± 3	± 2	± 1

<sup>a</sup> The glass from which YP1 was isolated (Cr-1r) was not analysed by EMPA or LA-ICP-MS.<sup>b</sup> Calculated based on <sup>133</sup>Cs and <sup>23</sup>Na MAS NMR data at 14.1 T.<sup>c</sup> Calculated by difference from Cr-3 EMPA composition assuming 32% Cs<sub>2</sub>O volatilisation.<sup>d</sup> Calculated by difference from Cr-3 LA-ICP-MS (spot measurement) composition assuming 28% Cs<sub>2</sub>O volatilisation.<sup>e</sup> Calculated based on <sup>133</sup>Cs and <sup>23</sup>Na MAS NMR data at 14.1 T and 21.1 T.<sup>f</sup> Direct EMPA measurement of crystalline YP4.<sup>g</sup> Calculated by difference from Cr-4 EMPA composition assuming 25% Cs<sub>2</sub>O volatilisation (see Table 6.10)

**Table 6.12.** Quantification of phase separation and volatilisation in Cr-4 glass

Component	mol% (nominal)	mol% (final)	Phase
<b>SiO<sub>2</sub></b>	60.45	60.45	Glass
<b>B<sub>2</sub>O<sub>3</sub></b>	17.26	17.26	Glass
<b>Na<sub>2</sub>O</b>	15.50	14.21	Glass
		1.29	Crystalline (YP4)
<b>Cs<sub>2</sub>O</b>	3.71	2.31	Glass
		0.47	Crystalline (YP4)
		0.93	Volatilised
<b>MoO<sub>3</sub></b>	2.56	0.60	Glass
		1.96	Crystalline (YP4)
<b>Cr<sub>2</sub>O<sub>3</sub></b>	0.52	0.32	Glass
		0.20	Crystalline (YP4)

is calculated. Additionally, higher-than-expected  $\text{Na}_2\text{O}$  content may indicate a sodium-rich region in the glass, suggesting the environment cannot be treated as homogeneous. The fact that the LA-ICP-MS and NMR compositions agree and are consistent with the rest of the data set (i.e., the YP1 and YP4 compositions) suggests that the YP3 EMPA determination is unreliable. Lastly, the YP1 sample composition was only determined through NMR analysis, but is consistent with the majority of the data set. Evidence of the lower  $\text{Cs}_2\text{O}$  content in this sample can be observed in the  $^{23}\text{Na}$  NMR spectra, where lower fractions of  $\text{CsNaMoO}_4 \cdot 2\text{H}_2\text{O}$  and  $\text{Cs}_3\text{Na}(\text{MoO}_4)_2$  are observed, compared to those in YP3 and YP4 (see Table 6.8).

#### 6.4 Summary

Solid-state multinuclear magnetic resonance experiments were used to evaluate the addition of chromium (as  $\text{Cr}_2\text{O}_3$ ) in a sodium-borosilicate model nuclear waste glass containing cesium and molybdenum. By generating a series of glasses with increasing chromium content, a more comprehensive analysis was obtained with regard to changes in the NMR spectra and Cr-partitioning between the glass and crystalline phases.  $^{133}\text{Cs}$ ,  $^{23}\text{Na}$ , and  $^{95}\text{Mo}$  MAS NMR experiments of the bulk material (glass and crystalline deposits) were useful for identifying and quantifying the various crystalline compounds (including structural disorder) that make up the phase-separated portion of these heterogeneous samples, while  $^{11}\text{B}$  and  $^{29}\text{Si}$  MAS NMR were used to establish correlations with the concentration of paramagnetic  $\text{Cr}^{3+}$  distributed throughout the glass network.

The inclusion of chromium produced a more accurate model of *yellow phase*, and hand-separation of the crystalline phase assemblages proved useful for a detailed and quantitative determination of the role of chromium.  $^{133}\text{Cs}$  MAS NMR revealed Cr substitution in  $\text{Cs}_3\text{Na}(\text{MoO}_4)_2$  and  $\text{CsNaMoO}_4 \cdot 2\text{H}_2\text{O}$ , showing preferential substitution in the former that may

be related to the interconversion of these compounds through hydration. The distribution of the  $^{133}\text{Cs}$  NMR intensity across the substitution peaks would make it harder to distinguish the presence of  $\text{Cs}_3\text{Na}(\text{MoO}_4)_2$  in a bulk sample of a Cr-containing glass. The heterogeneous nature of the model *yellow phases* was also highlighted by  $^{23}\text{Na}$  NMR, where seven unique sodium environments were detected through multiple-field collections and resolved using MQMAS.

Compositional analysis of the model *yellow phase* samples by treatment of the EMPA, LA-ICP-MS, and NMR data revealed relatively consistent compositions for  $\text{Na}_2\text{O}$ ,  $\text{Cs}_2\text{O}$ , and  $\text{MoO}_3$ , and verified the increasing chromium content in the crystalline phase. In particular, the agreement of the NMR compositions with those of EMPA (for YP4) and LA-ICP-MS (for YP3) highlights the strength of this method in characterising a complex heterogeneous material, since it is also able to quantify the relative levels of each crystalline component.



# Iron-Bearing Model HLW Glasses

*Following the series of chromium glasses in Chapter 6, an analogous investigation was launched to explore model waste glasses containing iron as the paramagnetic additive. A series of three glasses with an increasing concentration of iron (III) oxide ( $\text{Fe}_2\text{O}_3$ ) was prepared and characterised by solid-state NMR.  $^{133}\text{Cs}$  and  $^{23}\text{Na}$  MAS NMR spectra succeeded in identifying a number of crystalline components, and the increasing spectral breadth observed in  $^{11}\text{B}$  NMR was used to expand the dataset related to this trend. Analysis of a hand-separated crystalline deposit from one of the iron glasses revealed low-intensity unknown signals in  $^{133}\text{Cs}$  and  $^{23}\text{Na}$  NMR, showing minimal impact of  $\text{Fe}_2\text{O}_3$  on the composition of yellow phase.*

## 7.1 Iron in HLW Glasses

Iron is a fission product with a concentration around 1.22 mol%  $\text{Fe}_2\text{O}_3$  in factory borosilicate HLW glasses (see SON68 composition, Chapter 2, page 15), however it is also intentionally added to lead-phosphate waste glasses to increase corrosion resistance [103]. Iron predominantly exists in waste glasses as  $\text{Fe}^{3+}$  in tetrahedral and octahedral coordination, although  $\text{Fe}^{2+}$  is observed when  $\text{Fe}_2\text{O}_3$  is present in low concentrations [104,105], and the distinct redox equilibrium between  $\text{Fe}^{2+}$  and  $\text{Fe}^{3+}$  provides a useful indicator of the glass redox environment [106]. The presence of iron in lead-phosphate glasses result in the formation of haematite ( $\alpha\text{-Fe}_2\text{O}_3$ ) and magnetite ( $\text{Fe}_3\text{O}_4$ ) as corrosion products [107], while crystallisation of iron-containing borosilicate waste glasses may produce  $\gamma\text{-Fe}_2\text{O}_3$ ,  $\text{Fe}_3\text{O}_4$ ,  $\text{Fe}_3\text{BO}_5$ , and  $\text{ZnFe}_2\text{O}_4$  [108].

Furthermore, haematite and magnetite products provide surface adsorption sites for a variety of radioactive nuclides, including  $^{90}\text{Sr}$ ,  $^{137}\text{Cs}$ ,  $^{144}\text{Ce}$ , and  $^{237}\text{Pu}$  [109]. While sequestration of radioactive nuclides by these components may assist in preventing their release from the glass, the migration of groundwater and presence of similar compounds in the surrounding geological environment must be considered [110]. Given the unique roles of iron in waste glasses, it is worth exploring the possible role of iron in the formation and identity of *yellow phase*, and to assess the potentially deleterious effects of paramagnetic  $\text{Fe}^{2+}/\text{Fe}^{3+}$  on a solid-state NMR characterisation.

## 7.2 Experimental

### 7.2.1 Glass Synthesis

Sodium borosilicate glasses containing cesium, molybdenum, and a variable level of iron were prepared in a manner identical to that outlined in Chapter 5 (see section 5.2.1, page 37). A series of three glasses (“Fe-1”, “Fe-2”, and “Fe-3”) were prepared with target  $\text{Fe}_2\text{O}_3$  concentrations covering a range from 0.30 to 1.75 mol%. The target and batch (as-weighed) compositions of these three glasses are listed in Table 7.1. All glasses were prepared with a lid on the crucible. One of the glasses, Fe-1, produced a large crystalline deposit that was separated by hand (designated “ $\text{YP}_{\text{Fe}}$ ”) for further NMR analysis.

### 7.2.2 Electron Microprobe Analysis

Sample compositions for all three glasses were analysed by EMPA using a beam power of 10 nA and beam size of 40  $\mu\text{m}$ , with between 4 and 19 spot measurements collected for each glass. The effects of sodium mobility were corrected using a linear regression method by calibration of a glass standard (79% Si, 14% Na). [90,91]

**Table 7.1.** Compositions of iron series samples (mol%)

Sample		SiO <sub>2</sub>	B <sub>2</sub> O <sub>3</sub>	Na <sub>2</sub> O	Cs <sub>2</sub> O	MoO <sub>3</sub>	Fe <sub>2</sub> O <sub>3</sub>	Total
Fe-1	Target	61.63	17.44	15.63	2.50	2.50	0.30	100.00
	Weighed	60.86	17.28	15.40	3.73	2.44	0.29	100.00
	EMPA <sup>a</sup>	60.86	18.83	14.65	2.57	0.72	0.28	97.91
		± 0.93	± 1.01	± 0.18	± 0.07	± 0.06	± 0.03	
Fe-2	Target	61.44	17.38	15.58	2.50	2.50	0.60	100.00
	Weighed	60.78	17.10	15.34	3.72	2.46	0.60	100.00
	EMPA <sup>a</sup>	60.78	16.71	14.26	1.74	0.72	0.57	94.78
		± 0.61	± 0.79	± 0.19	± 0.05	± 0.06	± 0.04	
Fe-3	Target	60.70	17.15	15.40	2.50	2.50	1.75	100.00
	Weighed	59.90	17.11	15.24	3.55	2.48	1.72	100.00
	EMPA <sup>a</sup>	59.90	21.02	12.59	1.88	0.92	1.64	97.96
		± 1.16	± 1.56	± 0.63	± 0.03	± 0.08	± 0.13	

<sup>a</sup> EMPA composition is normalised to the nominal ('weighed') mol% SiO<sub>2</sub> (see section 6.3.1, page 62, for a detailed description of this method).

### 7.2.3 Nuclear Magnetic Resonance Spectroscopy

All NMR experiments were conducted on a Varian <sup>Unity</sup>Inova 600 ( $B_0 = 14.1$  T) spectrometer using a 1.6 mm triple-resonance Varian-Chemmagetics MAS probe at a spinning rate of 30 kHz. The samples were ground using an agate mortar and pestle and packed into 1.6 mm ZrO<sub>2</sub> rotors.

<sup>133</sup>Cs MAS NMR spectra of all samples were collected using single-pulse experiments (0.8  $\mu$ s,  $\sim 20^\circ$  tip angle,  $\nu_{rf} = 71$  kHz); glass samples were collected with a 60 s recycle delay and between 1120 and 2848 co-added transients, while the crystalline YP<sub>Fe</sub> sample was collected with a 500 s recycle delay and 151 co-added transients. Pulse calibration and spectral referencing were completed with an aqueous solution of cesium chloride (0.1 M CsCl, 0 ppm).

<sup>23</sup>Na MAS NMR spectra of all samples were collected using a single-pulse experiment (0.19  $\mu$ s,  $\sim 15^\circ$  tip angle,  $\nu_{rf} = 111$  kHz) with an optimised recycle delay of 1 s and 4096 co-added transients. Pulse calibration and spectral referencing were completed with an aqueous solution of sodium chloride (0.1 M NaCl, 0 ppm).

<sup>11</sup>B MAS NMR spectra for all glass samples were collected using single-pulse experiments (0.16  $\mu$ s,  $15^\circ$  tip angle,  $\nu_{rf} = 250$  kHz) with a 1 s recycle delay and 512 co-added transients. Pulse calibration and spectral referencing were completed with an aqueous solution of boric acid (0.1 M B(OH)<sub>3</sub>, 19.6 ppm).

## 7.3 Results and Discussion

Following high-temperature treatment, the sample masses were found to be about 7% lower than expected (after accounting for decarbonation), which is attributed to the volatilisation of Cs<sub>2</sub>O (as discussed in Chapters 5 and 6) [18,68]. The samples are visually distinct, where Fe-1 is a pale lime colour (mainly Fe<sup>2+</sup>), while glasses Fe-2 and Fe-3 are brown (mainly Fe<sup>3+</sup>) [105]. The hand separated crystalline material (YP<sub>Fe</sub>) has a faint yellow colouration.

### 7.3.1 Compositional Analysis of the Bulk Material

The compositions of the synthesised glasses were verified by EMPA, shown in Table 7.1, where the values have been normalised to the nominal mol% SiO<sub>2</sub>. As in the elemental analysis of the Cr series glasses (see Table 6.1, page 62), the normalised EMPA values do not sum to 100%, which reflects the volatilisation of Cs<sub>2</sub>O and the occurrence of phase separation. However, a notable difference with the Fe series glasses is the retention of nearly all the paramagnetic additive, indicating the preference of Fe<sub>2</sub>O<sub>3</sub> to remain in the vitreous network. The solubilised MoO<sub>3</sub> in the glass phase is 0.72 mol% for Fe-1 and Fe-2, in agreement with the Cr series glasses, while Fe-3 shows a slightly higher fraction of retained MoO<sub>3</sub> (0.92 mol%). However, Fe-3 also shows a large discrepancy between the nominal and analysed value of B<sub>2</sub>O<sub>3</sub> (about 3 mol%). These discrepancies are most likely due to insufficient sampling, as the sample of Fe-3 used for EMPA only had suitable room for the collection of four measurement spots. This is also reflected in the (generally) larger standard deviations associated with each analysed component of Fe-3.

### 7.3.2 NMR of the Bulk Material

<sup>133</sup>Cs MAS NMR. The <sup>133</sup>Cs MAS NMR spectra of the three iron glass samples are shown in Figure 7.1, where CsNaMoO<sub>4</sub>•2H<sub>2</sub>O and Cs<sub>3</sub>Na(MoO<sub>4</sub>)<sub>2</sub> are the only readily identified crystalline components. The integrated intensities, detailed in Table 7.2, show Cs<sub>3</sub>Na(MoO<sub>4</sub>)<sub>2</sub> to be the dominant crystalline product for all glasses. The glass-to-crystal ratio of Fe-1 has been affected by the removal of the crystalline phase YP<sub>Fe</sub>, so this sample shows lower crystalline content. Nevertheless, the fraction of Cs in glassy environments remains consistent around 95%, in agreement with the five-component base glass (96.5%). This indicates that the addition of Fe<sub>2</sub>O<sub>3</sub> to levels exceeding its factory concentration (1.22 mol%) does not induce more extensive crystallisation of Cs-bearing compounds.

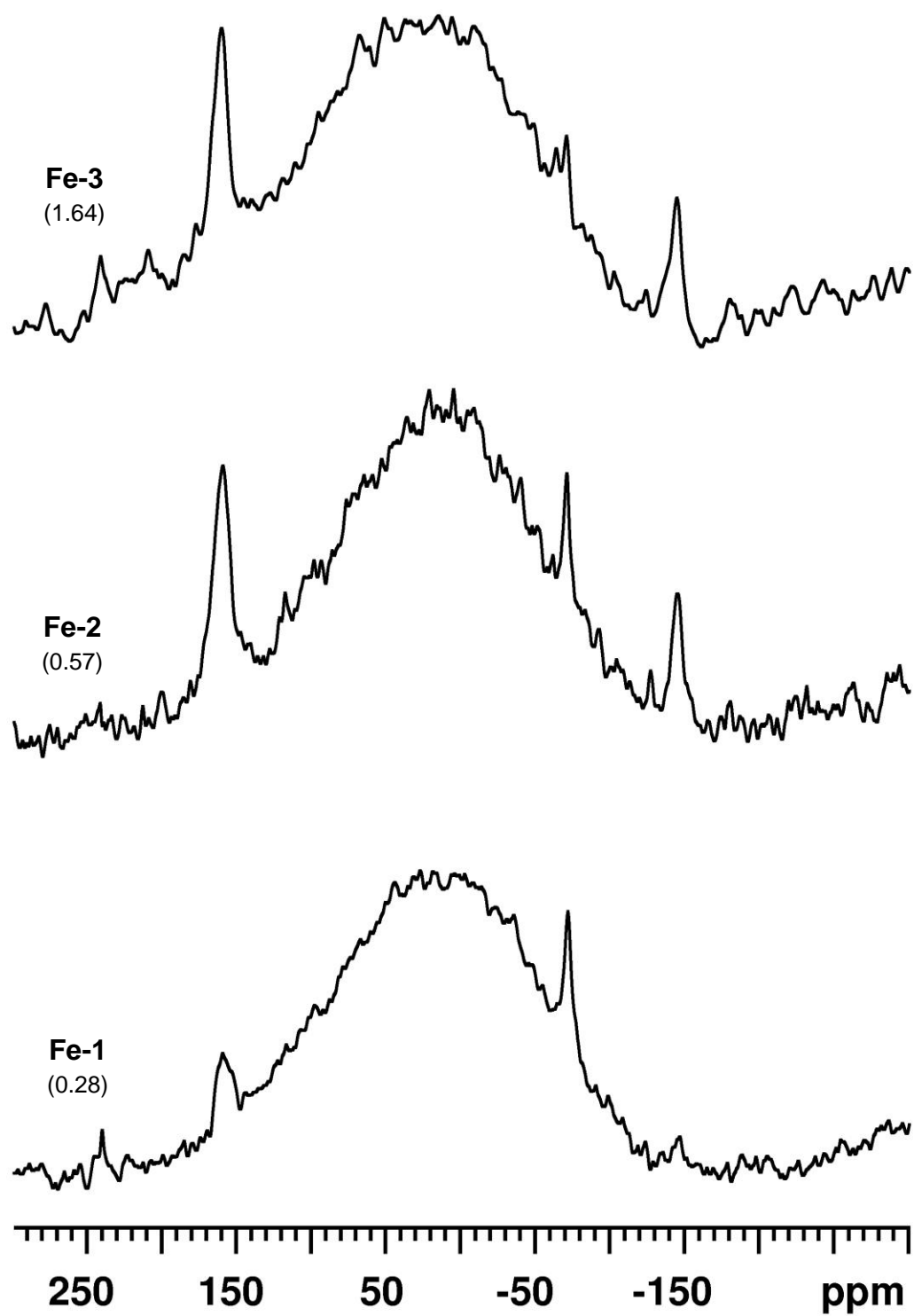


**Figure 7.1.** Experimental  $^{133}\text{Cs}$  MAS NMR spectra of iron series glasses. The analysed (EMPA) mol% of  $\text{Fe}_2\text{O}_3$  is noted beneath each sample name.

**Table 7.2.** Integrated intensities (%) for  $^{133}\text{Cs}$  MAS NMR of Fe series glasses

Glass Sample	Component		
	Glass	$\text{CsNaMoO}_4 \cdot 2\text{H}_2\text{O}$	$\text{Cs}_3\text{Na}(\text{MoO}_4)_2$
<b>Fe-1<sup>a</sup></b>	96.9	1.2	1.9
	$\pm 0.3$	$\pm 0.1$	$\pm 0.2$
<b>Fe-2</b>	94.0	0.8	5.2
	$\pm 0.4$	$\pm 0.2$	$\pm 0.2$
<b>Fe-3</b>	95.4	0.5	4.1
	$\pm 0.3$	$\pm 0.1$	$\pm 0.2$

<sup>a</sup> Integrated intensities represent what remains after a portion (~2 wt%) of the phase-separated crystalline material ( $\text{YP}_{\text{Fe}}$ ) was hand-separated.

$^{23}\text{Na}$  MAS NMR. The experimental  $^{23}\text{Na}$  MAS NMR spectra of the three iron glass samples are shown in Figure 7.2 along with spectral simulations that include contributions from sodium molybdate and cesium-sodium molybdate. For glass Fe-3 (1.64 mol%  $\text{Fe}_2\text{O}_3$ ), the broad site representing sodium in glassy environments does not appear as a simple Gaussian distribution, but shows a distinct tailing towards lower frequency; a full deconvolution of this spectrum is shown in Figure 7.3 to highlight the tailing required in modelling the glassy site. The characteristic change in shape is attributed to a distribution in quadrupolar couplings, which may be related to the proximity of glassy  $\text{Na}^+$  cations to paramagnetic iron. At lower concentrations of  $\text{Fe}_2\text{O}_3$  (e.g., Fe-1 and Fe-2), the effect is not as noticeable, but higher loadings increase the likelihood of  $\text{Na}^+$  and  $\text{Fe}^{3+}$  being nearby one another. In view of this, it is possible that the signal of glassy  $\text{Na}^+$  closest to  $\text{Fe}^{3+}$  becomes sufficiently broad to prevent its observation by  $^{23}\text{Na}$  NMR. The integrated intensities, listed in Table 7.3, show a continually decreasing contribution of glassy  $\text{Na}^+$  (however, note that about 2 wt% of Fe-1 was removed as the  $\text{YP}_{\text{Fe}}$  crystalline phase). This trend may be interpreted as greater crystallinity with higher  $\text{Fe}_2\text{O}_3$  content, however it more likely reflects that an appreciable portion of glassy  $\text{Na}^+$  is “invisible” due to significant paramagnetic broadening, where the separated *yellow phase* components are unaffected and appear with artificially increased relative intensities. This phenomenon was not detectable in  $^{133}\text{Cs}$  MAS NMR due to the much lower concentration of  $\text{Cs}_2\text{O}$  in these glasses relative to  $\text{Na}_2\text{O}$ .

$^{11}\text{B}$  MAS NMR. The  $^{11}\text{B}$  MAS NMR spectra of the three iron glasses are shown in Figure 7.4 (page 122). A plot using the absolute intensities shows how the increased paramagnetic broadening with higher  $\text{Fe}_2\text{O}_3$  content results in substantially reduced peak heights. The FWHM values for the iron glasses are plotted alongside all previously shown data points (Figure 7.5, page 123). The linear trend of  $^{13}\text{B}$  and  $^{41}\text{B}$  broadening with increasing  $2S \cdot \text{mol}\%$  is preserved



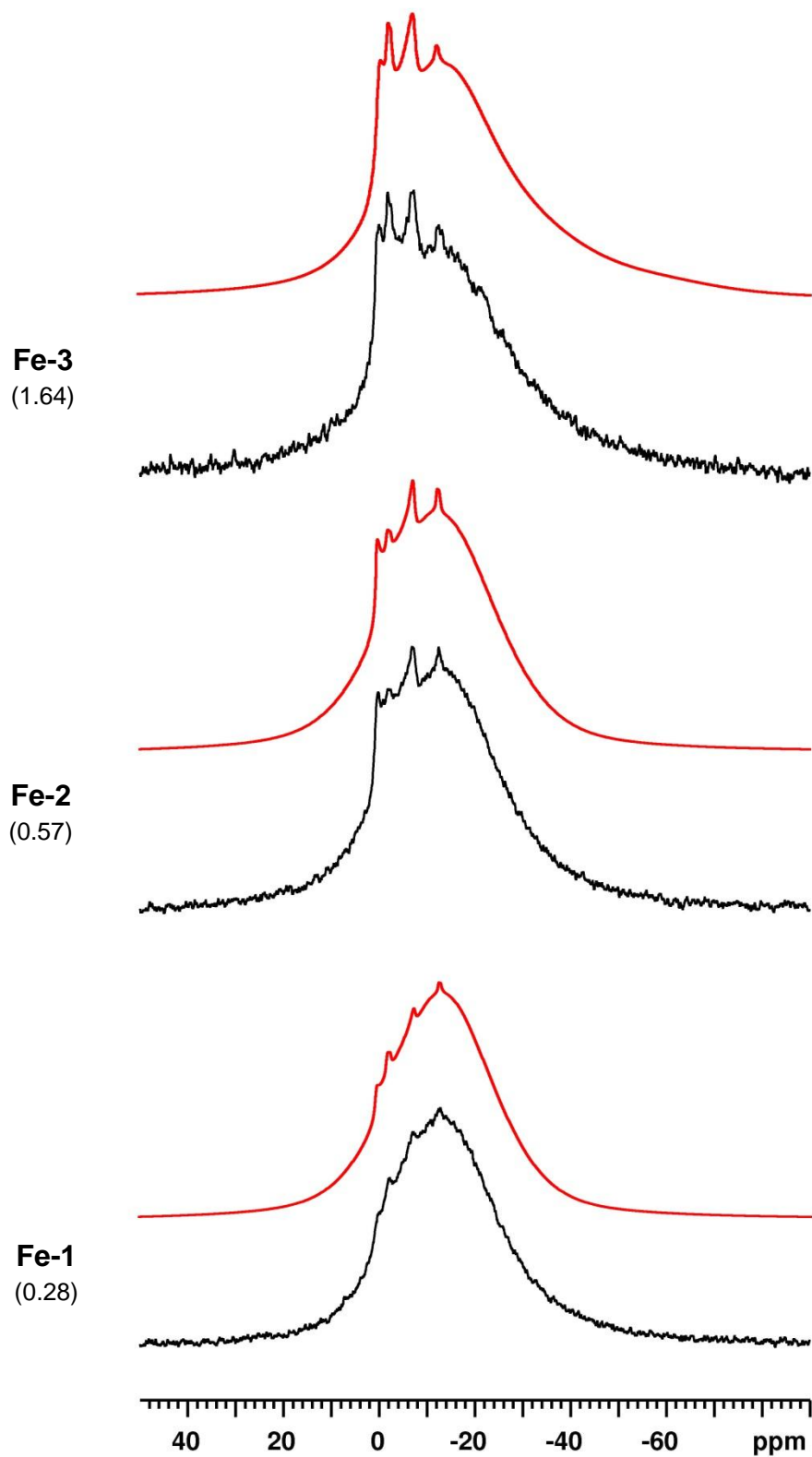


**Figure 7.2.** Experimental (black) and simulated (red)  $^{23}\text{Na}$  MAS NMR spectra of iron series glasses. The analysed (EMPA) mol% of  $\text{Fe}_2\text{O}_3$  is noted beneath each sample name.

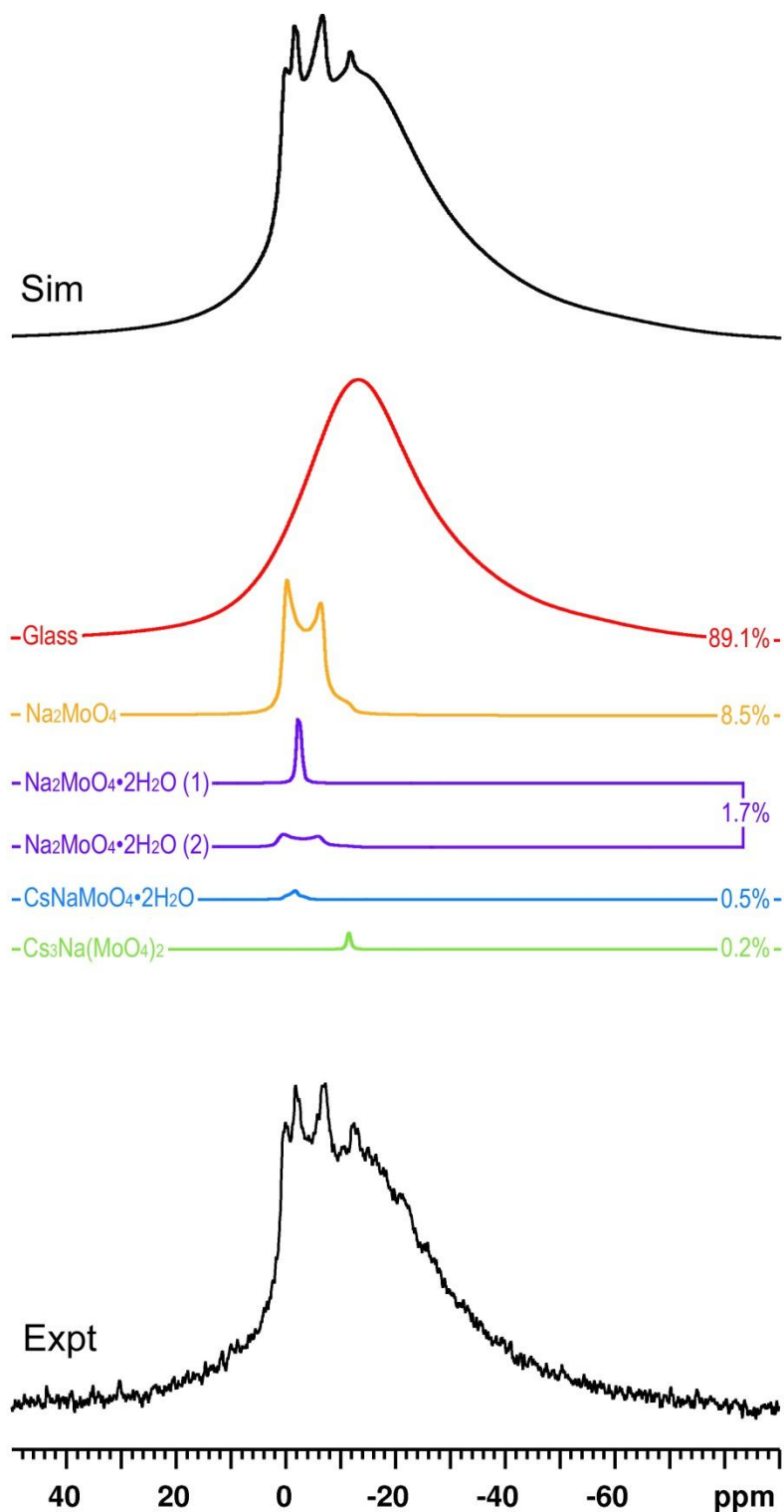


**Figure 7.3.** Experimental  $^{23}\text{Na}$  MAS NMR spectrum of glass Fe-3, with overall simulation and deconvolution of known sites, highlighting the tailing of the simulated site representing sodium in glassy environments (red).

**Table 7.3.** Integrated intensities (%) for  $^{23}\text{Na}$  MAS NMR of Fe series glasses

Glass Sample	Component				
	Glass	$\text{Na}_2\text{MoO}_4$	$\text{Na}_2\text{MoO}_4 \cdot 2\text{H}_2\text{O}$	$\text{CsNaMoO}_4 \cdot 2\text{H}_2\text{O}$	$\text{Cs}_3\text{Na}(\text{MoO}_4)_2$
<b>Fe-1<sup>a</sup></b>	96.6 $\pm 0.6$	2.3 $\pm 0.1$	0.6 $\pm 0.2$	0.3 $\pm 0.2$	0.2 $\pm 0.1$
<b>Fe-2</b>	93.0 $\pm 0.8$	5.7 $\pm 0.3$	0.4 $\pm 0.2$	0.6 $\pm 0.2$	0.3 $\pm 0.1$
<b>Fe-3</b>	89.1 $\pm 1.8$	8.5 $\pm 0.8$	1.7 $\pm 0.4$	0.5 $\pm 0.4$	0.2 $\pm 0.1$

<sup>a</sup> Integrated intensities represent what remains after a portion (~2 wt%) of the phase-separated crystalline material ( $\text{YP}_{\text{Fe}}$ ) was hand-separated.

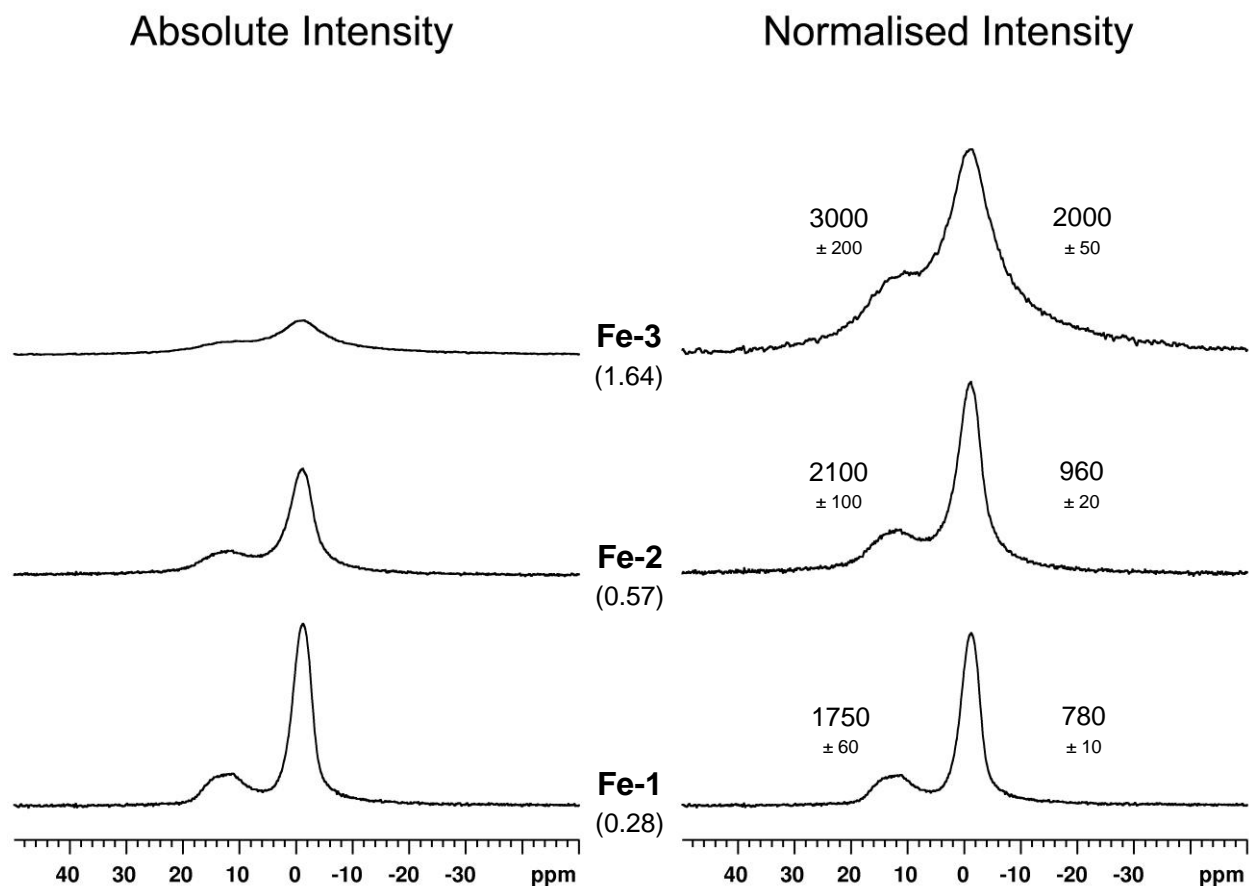


**Figure 7.4.** Experimental  $^{11}\text{B}$  MAS NMR spectrum of iron series glasses. The spectral view using absolute intensities (left) shows the decreased signal height resulting from increased broadening, while the normalised intensities (right) highlight the increased FWHM (in Hz) with mol%  $\text{Fe}_2\text{O}_3$ . The analysed (EMPA) mol%  $\text{Fe}_2\text{O}_3$  is noted beneath each sample name.

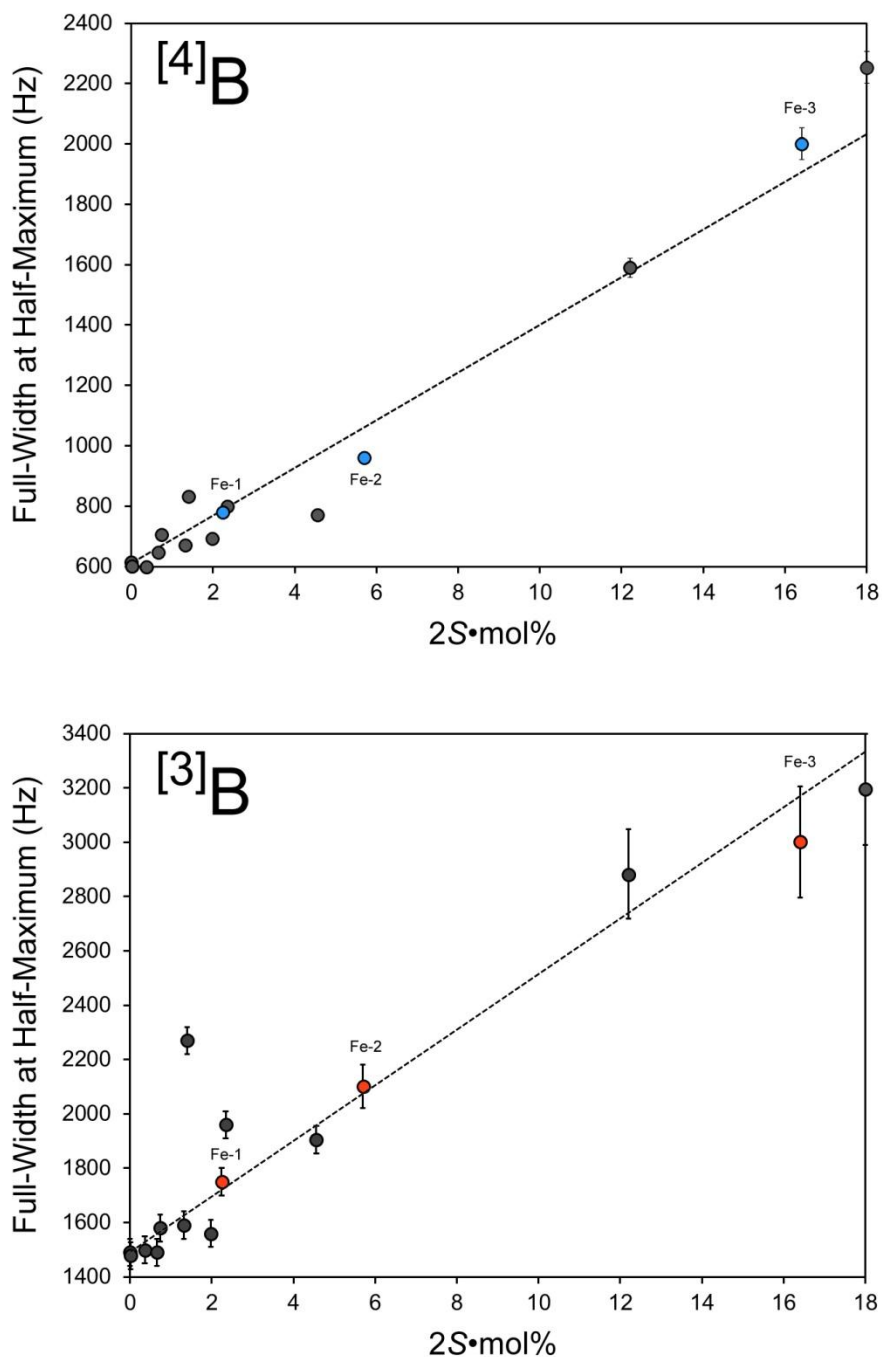


**Figure 7.5.** FWHM values for  $^{[3]}\text{B}$  (lower) and  $^{[4]}\text{B}$  (upper) as a function of paramagnetic content (using the  $2S\cdot\text{mol}\%$  parameter) for all glasses presented thus far. The fully-loaded paramagnetic sample (glass 9) appears at  $2S\cdot\text{mol}\%=18$ . The iron series glasses of this chapter have been highlighted. The  $2S\cdot\text{mol}\%$  value for Fe-1 was calculated using  $\text{Fe}^{2+}$  ( $S=2$ ), while Fe-2 and Fe-3 were calculated using  $\text{Fe}^{3+}$  ( $S=5/2$ ). The  $2S\cdot\text{mol}\%$  for glass 3 (Mn) (unlabelled) uses  $\text{Mn}^{2+}$ .

from the five-component base glass ( $2S \cdot \text{mol}\% = 0.0$ ) through Fe-3 ( $2S \cdot \text{mol}\% = 16.4$ ), indicating that the  $2S \cdot \text{mol}\%$  parameter is effective in correctly representing the paramagnetic effects of various metals. However, the oxidation state (or assortment of oxidation states) must be known to accurately place each data point. In the current series, the physical appearance of Fe-1 (see page 113) suggests the predominance of  $\text{Fe}^{2+}$ , and the respective FWHM values are plotted accordingly ( $\text{Fe}^{2+}$ ,  $d^6$ ,  $S = 2$ ). Conversely, glasses Fe-2 and Fe-3 are presumed to contain mostly  $\text{Fe}^{3+}$  ( $d^5$ ,  $S = 3/2$ ).

Using the Fe-3 data point (i.e., the iron glass sample with the highest FWHM values), the broadening factors of the  $^{13}\text{B}$  and  $^{14}\text{B}$  sites are 2.0 and 3.3, respectively. This higher degree of broadening on the  $^{14}\text{B}$  site may be ascribed to closer proximity of negatively charged  $\text{BO}_4^-$  units to iron cations ( $\text{Fe}^{2+}/\text{Fe}^{3+}$ ) than to neutral  $\text{BO}_3$ . Interestingly, no difference in the broadening factors was observed in the chromium series glasses (see section 6.3.2, page 78), however the divergent broadening factor slopes (Figure 7.6) become more noticeable at higher paramagnetic loadings (such as that in Fe-3 and glass 9). Furthermore, any amount of diamagnetic  $\text{Cr}^{6+}$  in the chromium glasses (a small fraction is likely present) would shift the data to lower  $2S \cdot \text{mol}\%$  values, meaning that the broadening trend is not suitably defined by looking at the chromium series glasses. Nevertheless, the steeper slope for the  $^{14}\text{B}$  data indicates a stronger broadening effect.

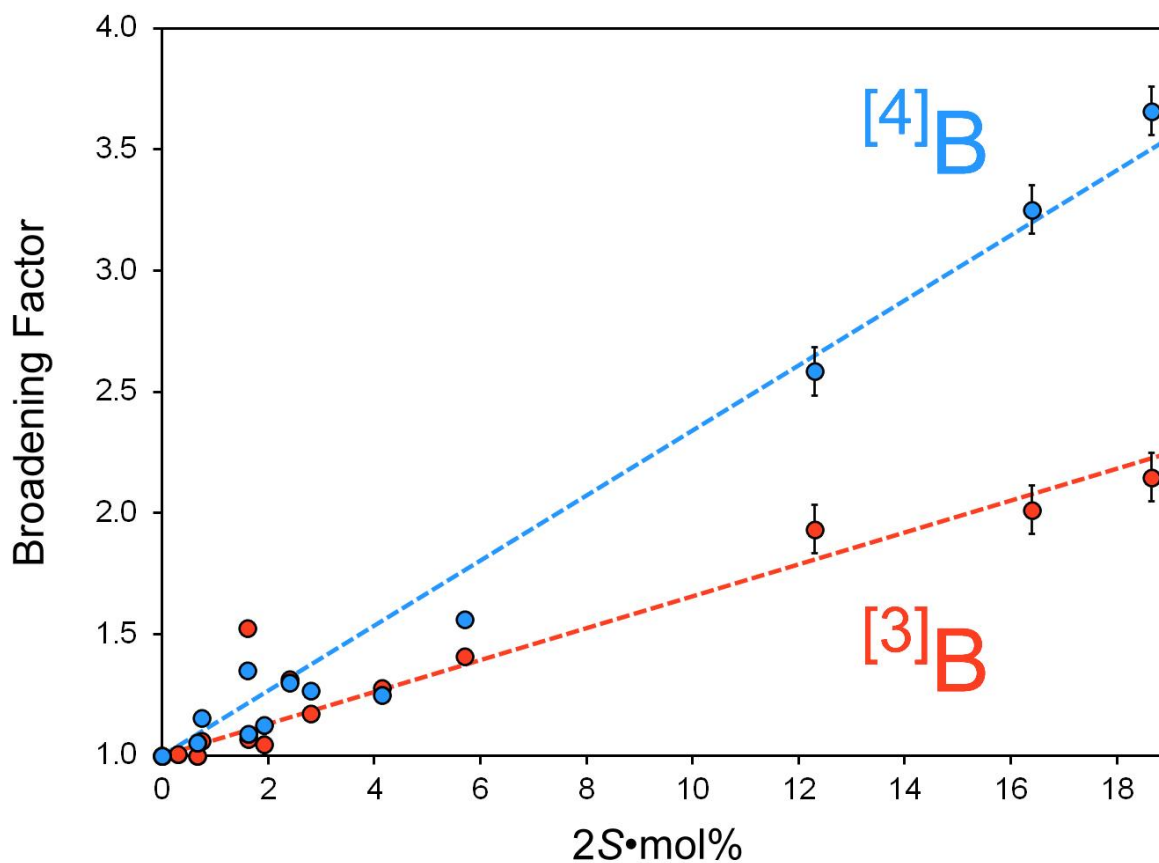


**Figure 7.6.** Relative broadening factors, defined as “ $\text{FWHM}_{(\text{Expt})} / \text{FWHM}_{(\text{Base Glass})}$ ”, for  $^{[3]}\text{B}$  (red) and  $^{[4]}\text{B}$  (blue). The greater slope of the  $^{[4]}\text{B}$  data indicate a stronger paramagnetic broadening effect caused by  $\text{BO}_4^-$  being closer to paramagnetic cations than neutral  $\text{BO}_3$ . The divergent slopes make this effect more pronounced at higher paramagnetic loadings ( $2S \cdot \text{mol}\%$ ). The fully-loaded paramagnetic sample (glass **9**) appears at  $2S \cdot \text{mol}\% = 18.7$ . The  $2S \cdot \text{mol}\%$  for glass **3** (Mn) (unlabelled) uses  $\text{Mn}^{2+}$ .

### 7.3.3 NMR of the Crystalline Phase

<sup>133</sup>Cs MAS NMR. The <sup>133</sup>Cs MAS NMR spectrum of the hand-separated YP<sub>Fe</sub> phase assemblage is shown in Figure 7.7. The spectrum consists of resonances from Cs<sub>2</sub>MoO<sub>4</sub> (55 & -16 ppm), CsNaMoO<sub>4</sub>•2H<sub>2</sub>O (-71 ppm), and Cs<sub>3</sub>Na(MoO<sub>4</sub>)<sub>2</sub> (161 & -145 ppm). Additionally, small signals are noted at positions adjacent to the peaks of CsNaMoO<sub>4</sub>•2H<sub>2</sub>O (at -87 ppm) and Cs<sub>3</sub>Na(MoO<sub>4</sub>)<sub>2</sub> (at 138 ppm near the Cs(1) site, and -128, -138, and -158 ppm near the Cs(2) site). The appearance of these signals is akin to those encountered in <sup>133</sup>Cs MAS NMR of the chromium-containing model *yellow phase* (see section 6.3.3, page 84), which were attributed to the atomic substitution of Mo for Cr. However, the substitution of iron (Fe<sup>2+</sup>, Fe<sup>3+</sup>, or Fe<sup>6+</sup>) would produce paramagnetic relaxation enhancement of these <sup>133</sup>Cs sites, the likes of which were not encountered when the spectra were collected with short recycle delays (i.e., 0.5 to 30 s). Figure 7.8 shows the full <sup>133</sup>Cs MAS NMR pattern of the YP<sub>Fe</sub>, with a spectral deconvolution depicting the integrated intensities of the fit, where the aforementioned unknown resonances contribute 3.4% of the total integrated intensity.

<sup>23</sup>Na MAS NMR. The experimental <sup>23</sup>Na MAS NMR spectrum of YP<sub>Fe</sub> is shown in Figure 7.9 (page 129) along with and deconvolution of six unique sodium environments. An unknown site was detected at  $\delta_{\text{iso}} = -11$  ppm, which has been confirmed unequivocally through <sup>23</sup>Na MQMAS NMR (Figure 7.10), where it has been resolved from patterns of Cs<sub>3</sub>Na(MoO<sub>4</sub>)<sub>2</sub> and Na<sub>2</sub>Mo<sub>2</sub>O<sub>7</sub>. The low content of this unknown site (0.4% in the one-dimensional data) precludes an accurate characterisation of its quadrupolar parameters, therefore only  $\delta_{\text{iso}}$  is reported. Since this site is only observed in YP<sub>Fe</sub>, it may be related to the presence of Fe<sub>2</sub>O<sub>3</sub>, however further experimentation (i.e., synthesis of more Fe-series glasses, *inversion recovery* relaxation experiments on YP<sub>Fe</sub>, etc.) would be required for verification.



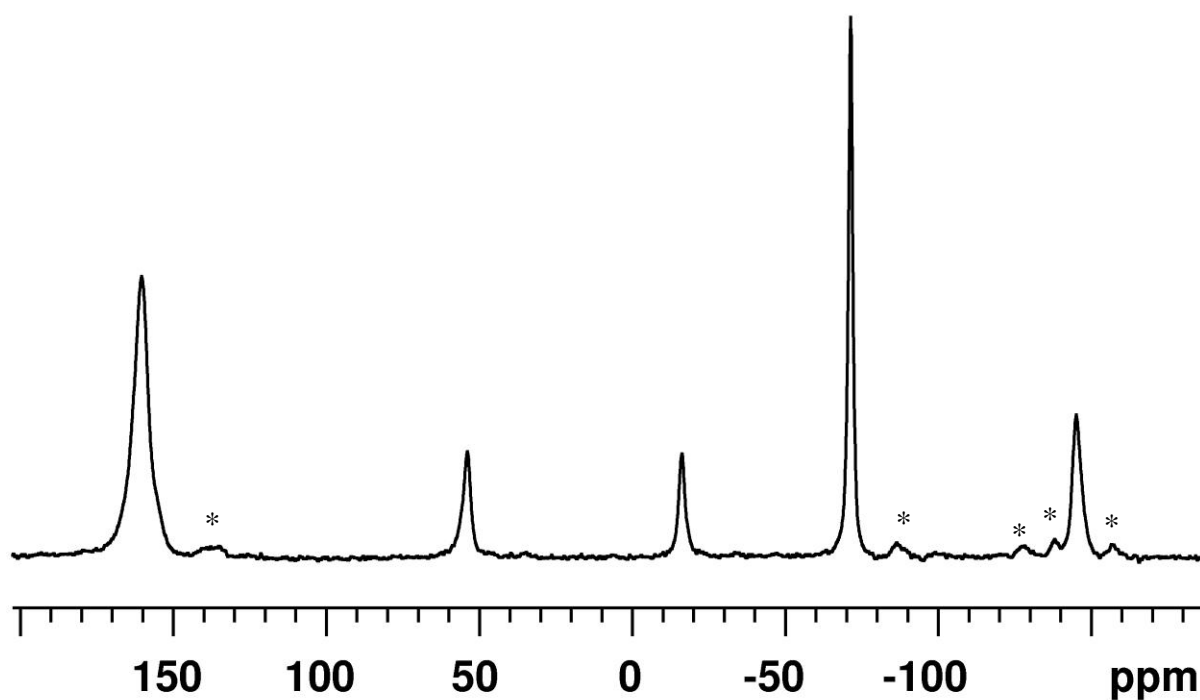


**Figure 7.7.**  $^{133}\text{Cs}$  MAS NMR spectrum of  $\text{YP}_{\text{Fe}}$ , consisting of  $\text{Cs}_2\text{MoO}_4$  (55 & -16 ppm),  $\text{CsNaMoO}_4 \cdot 2\text{H}_2\text{O}$  (-71 ppm), and  $\text{Cs}_3\text{Na}(\text{MoO}_4)_2$  (161 & -145 ppm). Small resonances (labelled by asterisks) are noted near  $\text{CsNaMoO}_4 \cdot 2\text{H}_2\text{O}$  and  $\text{Cs}_3\text{Na}(\text{MoO}_4)_2$  (see text).

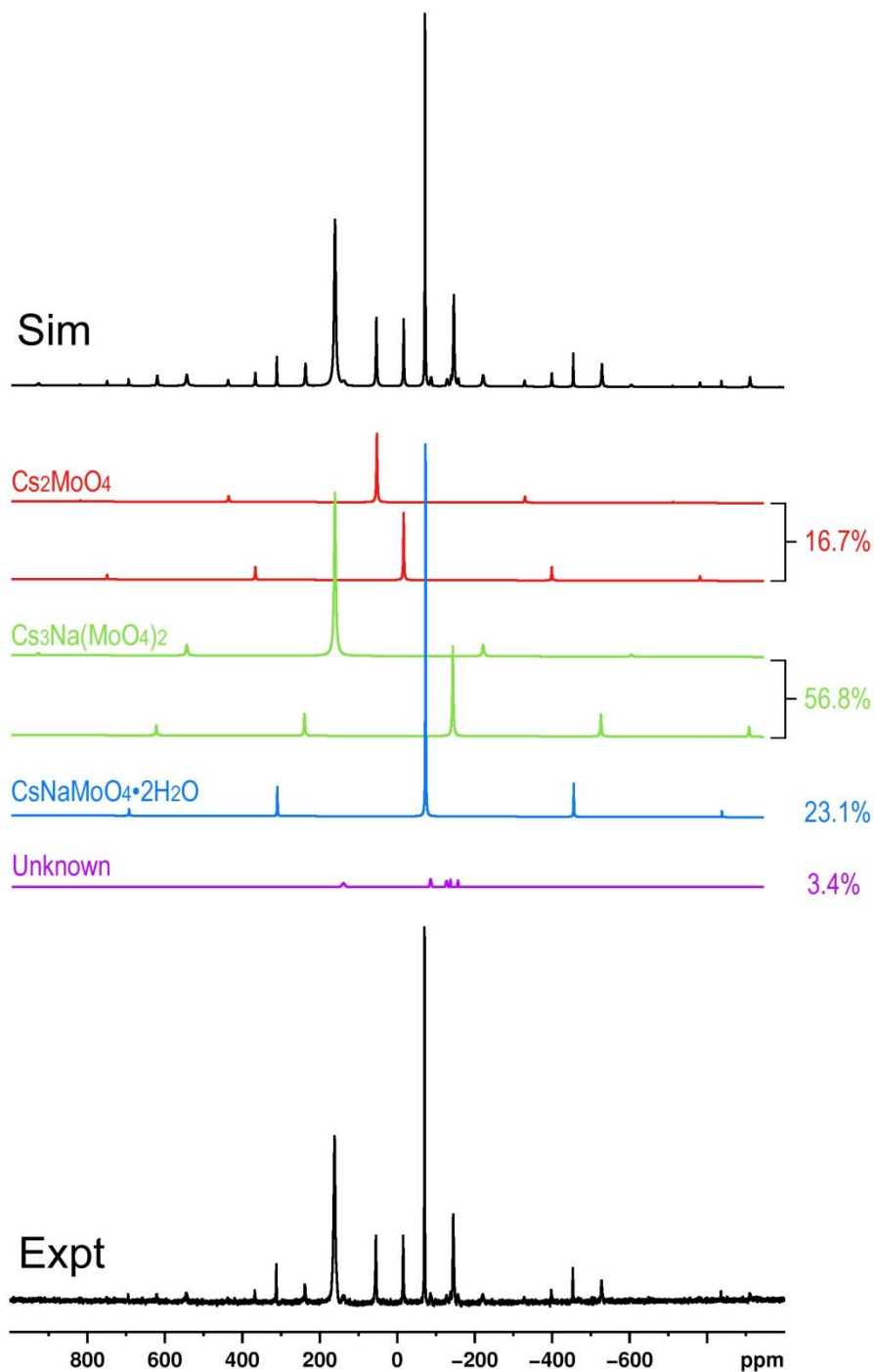


**Figure 7.8.** Full-view experimental  $^{133}\text{Cs}$  MAS NMR spectrum of  $\text{YP}_{\text{Fe}}$ , with overall simulation and deconvolution of known sites incorporating spinning-sideband intensity. The total of all unknown sites accounts for 3.4 % of the integrated intensity.

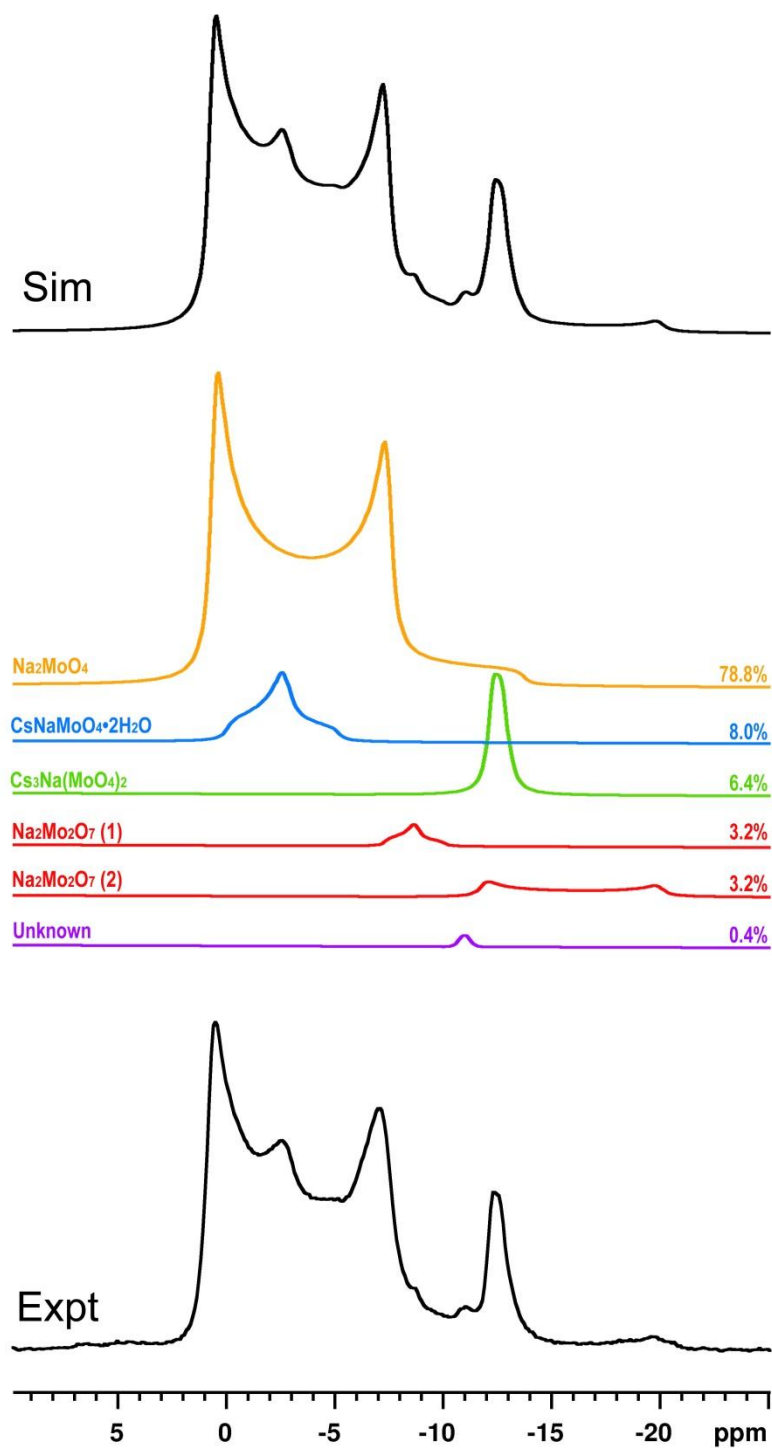


**Figure 7.9.** Experimental  $^{23}\text{Na}$  MAS NMR spectrum of  $\text{YP}_{\text{Fe}}$  with simulation and deconvolution based on six unique sodium environments. The intensity of the “Unknown” is site too low to be fit with accurate quadrupolar parameters.

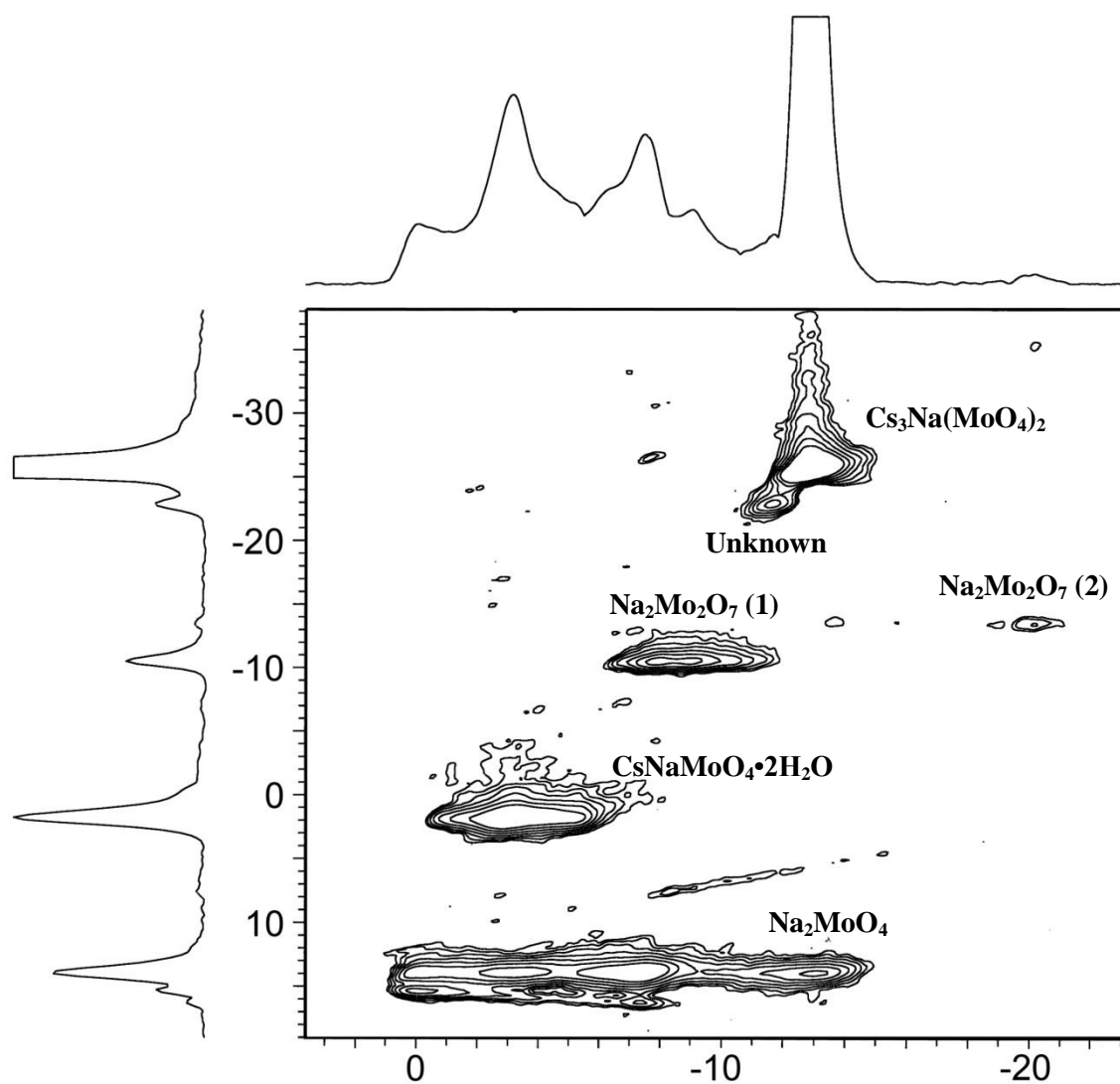


**Figure 7.10.**  $^{23}\text{Na}$  MQMAS NMR of  $\text{YP}_{\text{Fe}}$  at 14.1 T. The six environments (see Figure 7.9 for fit details) are resolved in two dimensions. The two-dimensional pattern of  $\text{Na}_2\text{Mo}_2\text{O}_7$  (2) is only partially detected here; see Figure 6.18 (page 101) for a better example of this site.

## 7.4 Summary

Sodium-borosilicate model nuclear waste glasses containing cesium and molybdenum were doped with variable concentrations of  $\text{Fe}_2\text{O}_3$  and investigated by multinuclear magnetic resonance spectroscopy.  $^{133}\text{Cs}$  MAS NMR experiments of the bulk material (glass and crystalline phases) revealed that both  $\text{CsNaMoO}_4 \cdot 2\text{H}_2\text{O}$  and  $\text{Cs}_3\text{Na}(\text{MoO}_4)_2$  could be readily detected, even with iron concentrations exceeding those of factory standards. Similarly,  $^{23}\text{Na}$  MAS NMR of the bulk material revealed several crystalline components, while the glass-phase  $\text{Na}^+$  peak showed continual broadening with increasing  $\text{Fe}_2\text{O}_3$  concentrations. The integrated intensities of the  $^{23}\text{Na}$  NMR spectra suggest that the paramagnetic interaction between  $\text{Na}^+$  and  $\text{Fe}^{2+}/\text{Fe}^{3+}$  can sufficiently broaden a portion of the glassy  $\text{Na}^+$  signal (at high  $\text{Fe}_2\text{O}_3$  concentrations) that it becomes undetectable, resulting in an artificially increased proportion of crystalline components. The  $^{11}\text{B}$  MAS NMR profiles of the Fe-series glasses underscored the strong effect of the paramagnetic interaction on  $^{31}\text{B}$  and  $^{41}\text{B}$  peak breadth. The combined  $^{11}\text{B}$  MAS NMR data of the Fe-series glasses and that from the foregoing work show a strong relationship between peak breadth and paramagnetic concentration (expressed as  $2S \cdot \text{mol}\%$ ) for  $^{41}\text{B}$  than  $^{31}\text{B}$ , reflecting the closer proximity of  $\text{BO}_4^-$  units to  $\text{Fe}^{2+}/\text{Fe}^{3+}$  cations.

$^{133}\text{Cs}$  MAS NMR of the hand-separated crystalline phase assemblage  $\text{YP}_{\text{Fe}}$  revealed sharp patterns of cesium- and cesium-sodium molybdates accompanied by low-intensity peaks that appear to be related to  $\text{CsNaMoO}_4 \cdot 2\text{H}_2\text{O}$  and  $\text{Cs}_3\text{Na}(\text{MoO}_4)_2$ , however no paramagnetic effects were detected.  $^{23}\text{Na}$  MAS NMR of  $\text{YP}_{\text{Fe}}$  revealed an unknown site that may be related to the addition of  $\text{Fe}_2\text{O}_3$ , but further experimentation is required.

Overall, the experiments exhibit how the added  $\text{Fe}_2\text{O}_3$  does not participate to any notable degree in the formation of *yellow phase*, and acts largely as a network modifier. From a spectroscopic perspective, the presence of paramagnetic  $\text{Fe}^{2+}/\text{Fe}^{3+}$  does not greatly affect  $^{133}\text{Cs}$

MAS NMR and still allows for deconvolution of  $^{23}\text{Na}$  MAS NMR spectra (albeit with the possibility of underestimated glass content), while the spectral quality of  $^{11}\text{B}$  MAS NMR spectra varies based on the  $\text{Fe}_2\text{O}_3$  concentration.

# Conclusions and Future Outlook

*Solid-state NMR experiments on sodium-borosilicate model HLW glasses containing cesium, molybdenum, and transition metal oxides have provided a wealth of information related to the identification and quantification of the crystalline components, insights into paramagnetic effects on the NMR spectra, and the sensitivity of these samples to atmospheric hydration. Current and forthcoming studies aim to explain and elaborate on these themes.*

### 8.1 Identification and Quantification of Crystalline Components

Study of phase-separated HLW glasses requires that the degree of crystallisation and identities of the products be determined. A theme of this work is the ability of solid-state NMR spectroscopy to clearly distinguish glassy and crystalline environments in phase-separated model HLW glasses. This capability, together with isotope selectivity, allows NMR to surpass conventional characterisation techniques (i.e., x-ray diffraction and Raman and infrared spectroscopies) for studying crystallisation products in these complex materials.

The sensitive chemical shift range and sharp lineshapes of crystalline environments make  $^{133}\text{Cs}$  MAS NMR experiments useful for evaluating different cesium compounds. For example, the glasses presented herein contained a variety of Cs-bearing products –  $\text{Cs}_2\text{MoO}_4$ ,  $\text{Cs}_2\text{CrO}_4$ ,  $\text{CsNaMoO}_4 \cdot 2\text{H}_2\text{O}$ , and  $\text{Cs}_3\text{Na}(\text{MoO}_4)_2$  – that could be readily identified by their distinct chemical shifts and quantified by integration of their MAS profiles. Similarly, the crystalline environments of Na-bearing products –  $\text{Na}_2\text{MoO}_4$ ,  $\text{Na}_2\text{MoO}_4 \cdot 2\text{H}_2\text{O}$ ,  $\text{Na}_2\text{Mo}_2\text{O}_7$ ,

$\text{CsNaMoO}_4 \cdot 2\text{H}_2\text{O}$ , and  $\text{Cs}_3\text{Na}(\text{MoO}_4)_2$  – were distinguished by their varying quadrupolar shapes and chemical shifts. Multiple-field and MQMAS  $^{23}\text{Na}$  NMR experiments provided additional resolution of these unique sodium environments and exhibit the complexity of *yellow phase*, while providing assurance that NMR is capable of recognising (and quantifying) the individual crystalline components with high accuracy.

Overall, the NMR experiments revealed  $\text{Na}_2\text{MoO}_4$  to be the major constituent of the model *yellow phase*, which is attributed to the higher concentration of  $\text{Na}_2\text{O}$  in these compositions compared to  $\text{Cs}_2\text{O}$  (about 15.5 mol% versus 2.5 mol%, respectively). Consequently, the  $^{133}\text{Cs}$  MAS NMR spectra become very important for the accurate determination of the relative levels of  $\text{CsNaMoO}_4 \cdot 2\text{H}_2\text{O}$  and  $\text{Cs}_3\text{Na}(\text{MoO}_4)_2$ , since their low representation (and necessary deconvolution) in  $^{23}\text{Na}$  MAS NMR presents larger relative errors.

$^{95}\text{Mo}$  MAS NMR experiments are useful because of the centrality of Mo to phase separation, but present greater difficulty regarding experimental aspects and (to some extent) spectral interpretation. The NMR chemical shift range of  $^{95}\text{Mo}$  allows for sufficient resolution of  $\text{Na}_2\text{MoO}_4 \cdot 2\text{H}_2\text{O}$ ,  $\text{Cs}_2\text{MoO}_4$ , and molybdenum in glassy environments at both 14.1 T and 21.1 T. However, the  $^{95}\text{Mo}$  resonances of  $\text{Na}_2\text{MoO}_4$  and  $\text{CsNaMoO}_4 \cdot 2\text{H}_2\text{O}$  cannot be resolved due to very similar chemical shift values (-33.5 and -32 ppm, respectively). Nevertheless, the  $^{23}\text{Na}$  NMR integrated intensities of these compounds provides an indication of their relative levels, and can be used to assist interpretation of the  $^{95}\text{Mo}$  NMR data.

Combined, the  $^{133}\text{Cs}$ ,  $^{23}\text{Na}$ , and  $^{95}\text{Mo}$  MAS NMR data can be utilised to obtain a reliable estimate of *yellow phase* composition. This has been used to compare the batch compositions with those determined by elemental analyses (EMPA and LA-ICP-MS) to track the compositional impacts of phase separation (and volatilisation, for  $\text{Cs}_2\text{O}$ ). Of particular value was the ability to hand-separate the crystalline component from some of these samples, allowing for



more informative spectra of *yellow phase* components. NMR experiments of the hand-separated crystalline components from the Cr- and Fe-based glasses allowed detection of low-intensity unknown sites that would have been otherwise unnoticed.

## 8.2 Paramagnetic Effects of Transition Metal Oxides

As expected, the addition of network-modifying paramagnetic transition metals introduces varying degrees of broadening to the NMR spectra of the model waste glasses, which is interpreted according to the role of each component in the glass network (i.e., former or modifier).

### 8.2.1 NMR of Network Modifiers

The peak breadths observed in  $^{133}\text{Cs}$  MAS NMR show no dependence on transition metal oxide loading (aside from disorder in Cr-substituted molybdates). The reason for this is that  $\text{Cs}_2\text{O}$  and the transition metal oxide additives are all network modifier cations that are present in low concentrations (around 0.2 to 2.5 mol%), so they would seldom be in close proximity. Furthermore, the chemical shift distribution of  $\text{Cs}^+$  in glassy environments creates a broad peak (even in the absence of paramagnetic components) such that a slight amount of paramagnetic broadening would be undetectable within the error of a FWHM measurement. Quantitative *spin-counting* NMR experiments, which track the relationship between moles of sample (e.g., of  $\text{Cs}_2\text{O}$ , by composition) and NMR signal, would allow one to verify if all of the expected  $^{133}\text{Cs}$  intensity is being observed or if a portion is being lost to paramagnetic broadening. With no noticeable relaxation effects detected for any crystalline components of the samples presented herein, the interpretation of  $^{133}\text{Cs}$  MAS NMR experiments of model HLW glasses becomes

complicated more by the formation of new crystalline compounds (e.g., the substitution of Cr, see section 8.3) than by the potential for paramagnetic effects.

The  $^{23}\text{Na}$  MAS NMR spectra of model HLW glasses containing transition metal oxides show little effect with increasing paramagnetic content, exhibiting slight FWHM increases at higher loadings.  $\text{Na}_2\text{O}$  acts as a network modifier, however it is present in higher concentrations than  $\text{Cs}_2\text{O}$  (around 15.5 mol%) and therefore is more likely to be close to a paramagnetic transition metal cation. Paramagnetic broadening is most noticeable for the Fe-series glasses, where an estimated 5-7% of the  $^{23}\text{Na}$  NMR signal for glassy  $\text{Na}^+$  becomes undetectable, resulting in artificially increased integrated intensities for the crystalline component. In most glass samples, the proportion of glassy  $\text{Na}^+$  was 95%, where systematic deviations to lower values for the Fe-series glasses indicate the deleterious effect of paramagnetic broadening. However, this effect is only significant at high paramagnetic loadings (25 mol% greater than 6), which is only surpassed by the factory concentration of  $\text{Fe}_2\text{O}_3$ . The other transition metal oxides presented with  $^{23}\text{Na}$  MAS NMR data (i.e.,  $\text{Cr}_2\text{O}_3$ , and  $\text{NiO}$ ) pose no significant complications to spectral interpretation of  $^{23}\text{Na}$  MAS NMR at their factory levels.

### 8.2.2 NMR of Network Formers

The charge-balancing relationship between network-modifier transition-metal cations and negatively charged network-former units suggests a stronger effect to be observed than those of  $\text{Cs}_2\text{O}$  or  $\text{Na}_2\text{O}$ . Indeed, both  $^{11}\text{B}$  and  $^{29}\text{Si}$  MAS NMR reveal spectroscopic behaviour in the paramagnetic samples that can be explained according to this principle.

Notable broadening in the  $^{11}\text{B}$  MAS NMR spectra of the paramagnetic HLW glasses is consistent with previous literature observations [94], and presents perhaps the most damaging impact of transition metal oxides to the study of these systems by NMR spectroscopy. FWHM

measurements of the  $^{13}\text{B}$  and  $^{14}\text{B}$  peaks indicate linear broadening with increased paramagnetic loading ( $2S\cdot\text{mol}\%$ ) with a corresponding loss in resolution of these two regions that impacts the ability to deconvolute the  $^{11}\text{B}$  MAS NMR spectrum (and therefore, the accuracy of the quantification). Overlap of the  $^{13}\text{B}$  and  $^{14}\text{B}$  patterns occurs around a value of  $2S\cdot\text{mol}\% = 2$ , which is surpassed by the factory concentrations of  $\text{Nd}_2\text{O}_3$  and  $\text{Fe}_2\text{O}_3$  alone. Normalisation of the  $^{13}\text{B}$  and  $^{14}\text{B}$  site broadening by the relative broadening factor ( $\text{FWHM}_{(\text{Expt})} / \text{FWHM}_{(\text{Base Glass})}$ ) indicates a stronger broadening effect for  $\text{BO}_4^-$ , which is consistent with the charge-balancing offered by paramagnetic transition metal cations.

$^{29}\text{Si}$  MAS NMR experiments also show strong spectroscopic effects related to the presence of paramagnetic transition metals. The long  $T_1$  relaxation of  $^{29}\text{Si}$  is extremely sensitive to the presence of even low concentrations of these additives; for example, a sharp  $T_1$  decrease from 168 to 16 s was observed with the addition of only 0.06 mol%  $\text{Cr}_2\text{O}_3$ . Experimentally, this decrease is advantageous for the ability to collect  $^{29}\text{Si}$  MAS NMR spectra in a shorter amount of time. A consequent increase in the FWHM is also observed, which produces even more ambiguity for deconvolution of the  $Q^4$  and  $Q^3$  sites at modest paramagnetic loadings.

### 8.3 Chromium as a Phase-Separation Product

As postulated, the similarities between chromium and molybdenum present interesting findings regarding the role of chromium in the formation and identity of *yellow phase*.  $^{133}\text{Cs}$  MAS NMR experiments reveal that  $\text{Cr}^{6+}$  substitutes into  $\text{Cs}_3\text{Na}(\text{MoO}_4)_2$  in place of  $\text{Mo}^{6+}$  according to a statistically predictable distribution as  $\text{Cs}_3\text{Na}(\text{Mo}_{1-x}\text{Cr}_x\text{O}_4)_2$ . Furthermore, evidence of the substitution of  $\text{Cr}^{6+}$  into  $\text{CsNaMoO}_4\cdot 2\text{H}_2\text{O}$  may be detected. While this is not unexpected given the interconversion of these two compounds through hydration/dehydration (see section 8.4), it is evident that the presence of  $\text{Cr}^{6+}$  in  $\text{CsNaMoO}_4\cdot 2\text{H}_2\text{O}$  is less favourable than in  $\text{Cs}_3\text{Na}(\text{MoO}_4)_2$ .

The ability of NMR to identify and quantify these structural abnormalities highlights the strength and significance of this characterisation method in the determination of *yellow phase* identity, which assists in understanding the physical properties and long-term implications of nuclear waste glass devitrification products.

The addition of  $\text{Cr}_2\text{O}_3$  to a cesium-sodium borosilicate glass shows the inclination of chromium to phase separation even in the absence of  $\text{MoO}_3$ . Observation of unknown resonances in both  $^{133}\text{Cs}$  and  $^{23}\text{Na}$  MAS NMR indicates the presence of cesium and sodium chromate compounds (including the possibility of Cs-Na chromates) with similar crystallisation tendencies to  $\text{MoO}_3$  (i.e., about 5% integrated intensity crystalline compounds). Further experimentation would be required to determine the identities of the unknown products and evaluate the preference of their formation against substitution of Cr into molybdate compounds.

#### 8.4 Hydration of Cesium-Sodium Molybdate

Concurrent studies on our group are exploring the interconversion of  $\text{Cs}_3\text{Na}(\text{MoO}_4)_2$  and  $\text{CsNaMoO}_4 \cdot 2\text{H}_2\text{O}$  through hydration, as detailed by equation (6-1) of section 6.3.3 (page 94). Within the presented work, the observation of  $\text{Cs}_2\text{MoO}_4$  and  $\text{Cs}_2\text{CrO}_4$  upon sample hydration indicated the existence of an alternative hydration mechanism (equation (6-2), page 94) and showed how the Cr-substituted  $\text{Cs}_3\text{Na}(\text{Mo}_{1-x}\text{Cr}_x\text{O}_4)_2$  compound is able to produce  $\text{CsNaMoO}_4 \cdot 2\text{H}_2\text{O}$  with minimal Cr substitution. Spectroscopic detection of these occurrences - via characteristic  $^{133}\text{Cs}$  MAS NMR chemical shifts and differing  $^{23}\text{Na}$  MAS NMR quadrupolar and chemical shift parameters - offers a means to identify and quantify the level and route of hydration. The impact on hydration of  $\text{Cs}_3\text{Na}(\text{MoO}_4)_2$  based on the presence of chromium could present new physical understandings of *yellow phase* performance during long-term geological storage of HLW glass.

## 8.5 Future Studies of Model HLW Glasses

### 8.5.1 Glass Series of Individual Paramagnetic Additives

In this work, the investigation of transition metal oxides in model HLW glasses was best handled by the preparation of a glass series that covered a range of concentrations of the particular paramagnetic additive. While two series of glasses were generated in this manner (i.e., Cr<sub>2</sub>O<sub>3</sub> and Fe<sub>2</sub>O<sub>3</sub>), only individual glasses of the other additives (i.e., MnO<sub>2</sub>, NiO, and Nd<sub>2</sub>O<sub>3</sub>) were prepared. Therefore, it may be instructive to explore these components in the same manner as the Cr and Fe glasses. In particular, the paramagnetic broadening exhibited by <sup>11</sup>B MAS NMR of the MnO<sub>2</sub> glass appeared well outside of the relationship established by the other samples. Examination of a glass series for this component would reveal how the broadening of paramagnetic Mn cations fits with regard to the remaining data.

### 8.5.2 Glass Series of Multiple Paramagnetic Additives

After a thorough understanding of individual model HLW glass additives has been achieved, it becomes viable to explore the possibility of cooperative effects that arise from their simultaneous addition. For example, the oxidation-state distribution of transition metal cations can be linked, such as the redox coupling between iron and chromium [106]:



Since the incorporation of chromium into *yellow phase* occurs as Cr<sup>6+</sup>, it would be of interest to evaluate the partitioning of Cr<sub>2</sub>O<sub>3</sub> based on the level of Fe<sub>2</sub>O<sub>3</sub> within a glass. If chromium does indeed affect the hydration of *yellow phase*, then the redox coupling between Fe and Cr may impact the physical performance of devitrification products. Experimentally, this requires the preparation of a glass series according to varying levels of the additives such as “(x)Fe<sub>2</sub>O<sub>3</sub>” and “(1-x)Cr<sub>2</sub>O<sub>3</sub>” while all others (i.e., SiO<sub>2</sub>, B<sub>2</sub>O<sub>3</sub>, Na<sub>2</sub>O, Cs<sub>2</sub>O, and MoO<sub>3</sub>) are held constant.

### 8.5.3 Compositional Complexity in Model HLW Glasses

Ultimately, the characterisation of model HLW glasses by NMR spectroscopy is important for understanding the implications of long-term storage of nuclear waste glasses. The presence of more components with different crystallisation tendencies changes which phase-separated compounds are obtained. For example, the presence of CaO stimulates the formation of calcium molybdate ( $\text{CaMoO}_4$ ) [15,111], and the addition of rare-earth oxides (e.g.,  $\text{ZrO}_2$  and  $\text{Nd}_2\text{O}_3$ ) offers the possibility of zirconium silicates, complex calcium rare-earth silicates [112-114], or the formation of cesium zirconate phases (e.g.,  $\text{Cs}_2\text{ZrO}_3$  [115] and  $\text{Cs}_4\text{ZrO}_4$  [116]). The addition of these components to the five- or six-component (i.e., Si-B-Na-Cs-Mo-Cr) system provides a means of building up the compositional complexity of model HLW glasses and working towards a more accurate depiction of phase separation in a factory glass.

## Appendix

# Binomial Distribution Models

If the addition of Cr atoms to  $\text{Cs}_3\text{Na}(\text{MoO}_4)_2$  is treated as a random substitution, the expected occupancies of each  $\text{Cs}(\text{Mo}/\text{Cr})$  unit (see Figure 6.12, page 89) are given according to the product of the combinations of Mo and Cr atoms. The relative fractions of Mo and Cr atoms (i.e., their probabilities  $p(\text{Mo})$  and  $p(\text{Cr})$ , respectively) will determine the fractions of each unique Cs unit. For a three-cation model (Cs surrounded by 3 Mo/Cr atoms), the distribution is given by the general formula:

$$p(3 - y\text{Mo}, y\text{Cr}) = {}^3C_y (p(\text{Mo}))^{3-y} (p(\text{Cr}))^y, \quad (\text{A-1})$$

where  $y = 0, 1, 2$ , or 3 Cr atoms

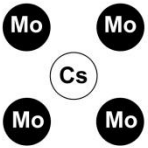
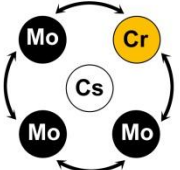
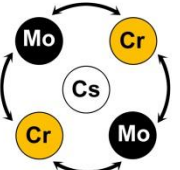
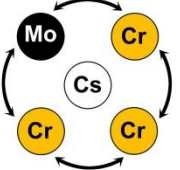
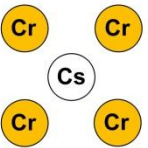
$$\text{and } {}^3C_y = 3!/(y!(3-y)!) \quad (\text{A-2})$$

If the crystalline phase is defined by  $\text{Cs}_3\text{Na}(\text{Mo}_{1-x}\text{Cr}_x\text{O}_4)_2$ , equation (A-1) can be written as:

$$p(3 - y\text{Mo}, y\text{Cr}) = {}^3C_y (1 - x)^{3-y} (x)^y \quad (\text{A-3})$$

It should be noted that this model assumes a completely random substitution, and that Cs sites (1) and (2) behave similarly and have equal second-sphere occupancy.

The four-cation model follows similar notation, however using '4-y' and 'y' as coefficients:

Site	Probability
<p>161 ppm -145 ppm</p> 	$p(4Mo, 0Cr) = \binom{4}{0} (1-x)^4 (x)^0$
<p>140 ppm -157 ppm</p> 	$p(3Mo, 1Cr) = \binom{4}{1} (1-x)^3 (x)^1$
<p>120 ppm -171 ppm</p> 	$p(2Mo, 2Cr) = \binom{4}{2} (1-x)^2 (x)^2$
<p>100 ppm -184 ppm</p> 	$p(1Mo, 3Cr) = \binom{4}{3} (1-x)^1 (x)^3$
<p>(80 ppm) (-197 ppm)</p> 	$p(0Mo, 4Cr) = \binom{4}{4} (1-x)^0 (x)^4$



# References

- [1] I. W. Donald, B. L. Metcalfe and R. N. J. Taylor, *J. Mater. Sci.*, 1997, **32**, 5851.
- [2] M. I. Ojovan, in *New Developments in Glassy Nuclear Wasteforms*, ed. M. I. Ojovan and W. E. Lee, Nova Science Publishers, New York, 2007.
- [3] T. LaTourette, in *Managing Spent Nuclear Fuel: Strategy Alternatives and Policy Implications*, ed. T. LaTourette, T. Light, D. Knopman and J. T. Bartis, Rand Corporation, Virginia, 2010.
- [4] International Atomic Energy Agency (Vienna), Design and operation of high level waste vitrification and storage facilities, Technical Reports Series No. 339 (IEAE, Vienna, 1992)
- [5] W. E. Lee, M. I. Ojovan, M. C. Stennett and N. C. Hyatt, *Adv. Appl. Ceram.*, 2006, **105**, 3.
- [6] S. Kroeker, in *Encyclopedia of Magnetic Resonance*, ed. R. K. Harris and R. E. Wasylshen, John Wiley & Sons, Chichester, 2011.
- [7] World Nuclear Association, London, UK. [www.world-nuclear.org](http://www.world-nuclear.org) (accessed April 12, 2012).
- [8] W. Lutze, in *Radioactive Wasteforms for the Future*, ed. W. Lutze and R. C. Ewing, North-Holland, Amsterdam, 1988.
- [9] R. J. Short, R. J. Hand, N. C. Hyatt and G. Möbus, *J. Nucl. Mater.*, 2005, **340**, 179.
- [10] D. Caurant, O. Majérus, E. Fadel, A. Quintas, C. Gervais, T. Charpentier and D. Neuville, *J. Nucl. Mater.*, 2010, **396**, 94.
- [11] P. Hrma, *J. Non-Cryst. Solids*, 2010, **356**, 3019.
- [12] S. Peugeot, J.-N. Cachia, C. Jégou, X. Deschanel, D. Roudil, V. Broudic, J.M. Delaye and J.-M. Bart, *J. Nucl. Mater.*, 2006, **354**, 1.
- [13] G. Calas, M. Le Grand, L. Galois and D. Ghaleb, *J. Nucl. Mater.*, 2003, **322**, 15.
- [14] K. Ferrand, A. Abdelouas and B. Grambow, *J. Nucl. Mater.*, 2006, **355**, 54.

- [15] D. Caurant, O. Majérus, E. Fadel and M. Lenoir, *J. Am. Ceram. Soc.*, 2007, **90**, 774.
- [16] B. J. Greer and S. Kroeker, *Phys. Chem. Chem. Phys.*, 2012, **14**, 7375.
- [17] (a) A. C. Wright, in *Experimental Techniques of Glass Science*, ed. C. J. Simmons and O. H. El-Bayoumi, The American Ceramic Society, USA, 1993.  
(b) C. G. Pantano, in *Experimental Techniques of Glass Science*, ed. C. J. Simmons and O. H. El-Bayoumi, The American Ceramic Society, USA, 1993.
- [18] D. Holland, B. G. Parkinson, M. M. Islam, A. Duddridge, J. M. Roderick, A. P. Howes and C. R. Scales, *Appl. Magn. Reson.*, 2007, **32**, 483.
- [19] C. Martineau, V. K. Michaelis, S. Schuller and S. Kroeker, *Chem. Mater.*, 2010, **22**, 4896.
- [20] S. Kroeker, C. S. Higman, V. K. Michaelis, N. B. Svenda and S. Schuller, *Mater. Res. Soc. Symp. Proc.*, 2010, **1265**, 1265-AA03-03.
- [21] M. Magnin, S. Schuller, C. Mercier, J. Trébose, D. Caurant, O. Majérus, F. Angéli and T. Charpentier, *J. Am. Ceram. Soc.*, 2011, **94**, 4274-4282.
- [22] J. E. Shelby, *Introduction to Glass Science and Technology*, The Royal Society of Chemistry, Oxford, 1997.
- [23] W. H. Zachariasen, *J. Am. Chem. Soc.*, 1932, **54**, 3842.
- [24] J. C. C. Chan, M. Bertmer and H. Eckert, *J. Am. Chem. Soc.*, 1999, **121**, 5238.
- [25] P. J. Bray, *Inorg. Chim. Acta*, 1999, **289**, 158.
- [26] J. E. Stanworth, *Physical Properties of Glass*, Oxford University Press, London, 1950.
- [27] M. H. Levitt, *Spin Dynamics*, John Wiley & Sons, West Sussex, 2001.
- [28] K. J. D. MacKenzie and M. E. Smith, *Multinuclear Solid-State NMR of Inorganic Materials*, Elsevier Science, Oxford, 2002.
- [29] R. K. Harris, *NMR Spectroscopy*, Pitman, London, 1984.
- [30] P. P. Man, in *Encyclopedia of Analytical Chemistry*, ed. R. A. Meyers, John Wiley & Sons, Chichester, 2000.

- [31] J. P. Jesson, in *NMR of Paramagnetic Molecules: Principles and Applications*, ed. G. N. La Mar, W. DeW. Horrocks, Jr. and R.H. Holm, Academic Press, New York, 1973.
- [32] D. L. Bryce, G. M. Bernard, M. Gee, M. D. Lumsden, K. Eichele and R. E. Wasylishen, *Can. J. Anal. Sci. Spect.*, 2001, **46**, 46.
- [33] S. Mooibroek, R. E. Wasylishen, R. Dickson, G. Facey and B. A. Pettitt, *J. Magn. Reson.*, 1986, **66**, 542.
- [34] V. P. Tarasov, G. A. Kirakosian, Yu. A. Buslaev and U. Eichoff, *Z. Phys. B*, 1990, **79**, 101.
- [35] R. B. Ejeckam and B. L. Sherriff, *Can. Mineral.*, 2005, **43**, 1131.
- [36] K. R. Whittle, G. R. Lumpkin and S. E. Ashbrook, *J. Solid State Chem.*, 2006, **179**, 512.
- [37] W. P. Power, R. E. Wasylishen, S. Mooibroek, B. A. Pettitt and W. Danchura, *J. Phys. Chem.*, 1990, **94**, 591.
- [38] V. K. Michaelis, P. M. Aguiar and S. Kroeker, *J. Non-Cryst. Solids*, 2007, **353**, 2582.
- [39] C. A. Click, R. K. Brow and T. M. Alam, *J. Non-Cryst. Solids*, 2002, **311**, 294.
- [40] H. Koller, G. Engelhardt, A. P. M. Kentgens and J. Sauer, *J. Phys. Chem.*, 1994, **98**, 1544.
- [41] T. J. Bastow, M. E. Hobday, M. E. Smith and H. J. Whitfield, *Solid State Nucl. Magn. Reson.*, 1994, **3**, 49.
- [42] J. D. Epping, W. Strojek and H. Eckert, *Phys. Chem. Chem. Phys.*, 2005, **7**, 2384.
- [43] S. E. Ashbrook and S. Wimperis, *J. Magn. Reson.*, 2000, **147**, 238.
- [44] S. E. Ashbrook, L. Le Pollès, R. Gautier, C. J. Pickard and R. I. Walton, *Phys. Chem. Chem. Phys.*, 2006, **8**, 3423.
- [45] V. M. Mastikhin, O. B. Lapina and R. I. Maximovskaya, *Chem. Phys. Lett.*, 1988, **148**, 413.
- [46] K. Eichele, R. E. Wasylishen and J. H. Nelson, *J. Phys. Chem. A*, 1997, **101**, 5463.
- [47] D. L. Bryce and R. E. Wasylishen, *Phys. Chem. Chem. Phys.*, 2002, **4**, 3591.

- [48] J.-B. d'Espinose de Lacaillerie, F. Barberon, K. V. Romanenko, O. B. Lapina, L. Polles, R. Gautier and Z. Gan, *J. Phys. Chem. B*, 2005, **109**, 14033.
- [49] M. A. M. Forgeron and R. E. Wasylishen, *J. Am. Chem. Soc.*, 2006, **128**, 7817.
- [50] N. Machida and H. Eckert, *Solid State Ionics*, 1998, **107**, 255.
- [51] S. H. Santagneli, C. C. de Araujo, W. Strojek, H. Eckert, G. Poirier, S. J. L. Ribeiro and Y. Messaddeq, *J. Phys. Chem. B*, 2007, **111**, 10109.
- [52] S. Kroeker, I. Farnan, S. Schuller and T. Advocat, *Mater. Res. Soc. Symp. Proc.*, 2009, **1124**, 153.
- [53] G. L. Turner, K. A. Smith, R. J. Kirkpatrick and E. Oldfield, *J. Magn. Reson.*, 1986, **67**, 544.
- [54] D. Muller, A. R. Grimmer, U. Timper, G. Heller and M. Shakibaieemoghadam, *Z. Anorg. Allgemeine Chem.*, 1993, **619**, 1262.
- [55] S. Kroeker and J. F. Stebbins, *Inorg. Chem.*, 2001, **40**, 6239.
- [56] P. Zhao, S. Kroeker and J. F. Stebbins, *J. Non-Cryst. Solids*, 2000, **276**, 122.
- [57] L.-S. Du and J. F. Stebbins, *Chem. Mater.*, 2003, **15**, 3913.
- [58] P. M. Aguiar and S. Kroeker, *J. Non-Cryst. Solids*, 2007, **353**, 1834.
- [59] P. F. Barron, R. L. Frost and J. O. Skjemstad, *J. Chem. Soc. Chem. Comm.*, 1983, 581.
- [60] J. F. Stebbins, W. R. Panero, J. R. Smyth and D. J. Frost, *Am. Mineral.*, 2009, **94**, 626.
- [61] J. Klinowski, S. W. Carr, S. E. Tarling and P. Barnes, *Nature*, 1987, **330**, 56.
- [62] C. Bessada, D. Massiot, J. Coutures, A. Douy, J.-P. Coutures and F. Taulelle, *J. Non-Cryst. Solids*, 1994, **168**, 76.
- [63] J. Alton, T. J. Plaisted and P. Hrma, *Chem. Eng. Sci.*, 2002, **57**, 2503.
- [64] P. Hrma, J. D. Vienna, B. K. Wilson, T. J. Plaisted and S. M. Heald, *J. Non-Cryst. Solids*, 2006, **352**, 2114.
- [65] D. G. Casler and P. Hrma, *Mater. Res. Soc. Symp. Proc.*, 1999, **556**, 255.

- [66] H. Miyoshi, D. Chen and T. Akai, *Phys. Chem. Glasses*, 2005, **46**, 157.
- [67] A. C. Silva, S. Mello-Castanho, F. Guitian, I. Montero, A. Esteban-Cubillo, I. Sobrados, J. Sanz and J. S. Moya, *J. Am. Ceram. Soc.*, 2008, **91**, 1300.
- [68] V. K. Michaelis and S. Kroeker, *Phys. Chem. Glasses: Eur. J. Glass Sci. Technol. B*, 2009, **50**, 249.
- [69] G. Calas, L. Cormier, L. Galois and P. Jollivet, *C. R. Chim.*, 2002, **5**, 831.
- [70] A. Terczyńska-Madej, K. Cholewa-Kowalska and M. Łączka, *Opt. Mater.*, 2010, **32**, 1456.
- [71] A. Terczyńska-Madej, K. Cholewa-Kowalska and M. Łączka, *Opt. Mater.*, 2011, **33**, 1984.
- [72] K. Marat, SpinWorks 3 (Version 3.1.5.0) (software), 2009, University of Manitoba. Retrieved from <ftp://davinci.chem.umanitoba.ca/pub/marat/SpinWorks>
- [73] D. Massiot, F. Fayon, M. Capron, I. King, S. Le Calvé, B. Alonso, J.-O. Durand, Z. Gan and G. Hoatson, *Magn. Reson. Chem.*, 2002, **40**, 70.
- [74] J. J. Jakobsen, H. Bildsøe, J. Skibsted, M. Brorson, I. Hung and Z. Gan, *Inorg. Chem.*, 2011, **50**, 7676.
- [75] J. Skibsted and H. J. Jakobsen, *Solid State Nucl. Magn. Reson.*, 1994, **3**, 29.
- [76] L.-S. Du and J. F. Stebbins, *J. Non-Cryst. Solids*, 2003, **315**, 239.
- [77] L.-S. Du and J. F. Stebbins, *J. Phys. Chem. B*, 2003, **107**, 10063.
- [78] V. A. Sokolov and M. D. Gasparyan, *Refract. Ind. Ceram.*, 2010, **51**, 183.
- [79] X. Wu, S. Huang, U. Howemmerich, W. M. Yen, B. G. Aitken and M. Newhouse, *Chem. Phys. Lett.*, 1995, **233**, 28.
- [80] H. Yuan, W. Jia, D. Cohen, W. M. Yen and B. G. Aitken, *Mater. Res. Soc. Symp. Proc.*, 1997, **455**, 483.
- [81] A. C. Silva and S. Mello-Castanho, *J. Am. Ceram. Soc.*, 2008, **91**, 1300.
- [82] P. B. Rose, D. I. Woodward, M. I. Ojovan, N. C. Hyatt and W. L. Lee, *J. Non-Cryst. Solids*, 2011, **357**, 2989.

- [83] J. J. Miller, *Z. Kristallogr. Krist.*, 1938, **99**, 32.
- [84] W. Gonschorek and T. Hahn, *Z. Kristallogr. Krist.*, 1973, **138**, 167.
- [85] J. Marrot and J.-M. Savariault, *Acta Crystallogr. C*, 1995, **51**, 2201.
- [86] R. Enjalbert, F. Guinneton and J. Galy, *Acta Crystallogr. C*, 1999, **55**, 273.
- [87] U. Kolitsch, *Acta Crystallogr. E*, 2003, **59**, i164.
- [88] U. Kolitsch, *Acta Crystallogr. C*, 2004, **60**, i17.
- [89] D. L. Bryce and R. E. Wasylshen, *Phys. Chem. Chem. Phys.*, 2001, **3**, 5154.
- [90] J. G. Spray and D. A. Rae, *Can. Mineral.*, 1995, **33**, 323.
- [91] G. B. Morgan and D. London, *Am. Mineral.*, 2005, **90**, 1131.
- [92] A. Abragam, *Principles of Nuclear Magnetism*, Clarendon Press, Oxford, 1961.
- [93] J. F. Stebbins, J. R. Smyth, W. R. Panero and D. J. Frost, *Am. Mineral.*, 2009, **94**, 905.
- [94] H. Deters, A. S. S. de Camargo, C. N. Santos, C. R. Ferrari, A. C. Hernandez, A. Ibanez, M. T. Rinke and H. Eckert, *J. Phys. Chem. C*, 2009, **113**, 16216.
- [95] D. D. Makitova, V. V. Tkachev and A. N. Chekhlov, *Russ. J. Coord. Chem.*, 2003, **29**, 163.
- [96] S. E. Ashbrook, K. R. Whittle, G. R. Lumpkin and I. Farnan, *J. Phys. Chem. B*, 2006, **110**, 10358.
- [97] E. J. Harvey, S. E. Ashbrook, G. R. Lumpkin and S. A. T. Redfern, *J. Mater. Chem.*, 2006, **16**, 4665.
- [98] I. Lindqvist, *Acta Chem. Scand.*, 1950, **4**, 1066.
- [99] M. Seleborg, *Acta Chem. Scand.*, 1967, **21**, 499.
- [100] K. D. Singh Mudher, M. Keskar, K. Krishnan and V. Venugopal, *J. Alloy Compd.*, 2005, **396**, 275.
- [101] C. Fernandez and J. P. Amoureux, *Chem. Phys. Lett.*, 1995, **242**, 449.

- [102] R. Iwamoto, C. Fernandez, J. P. Amoureux and J. Grimblot, *J. Phys. Chem. B*, 1998, **102**, 4342.
- [103] B. C. Sales and L. A. Boatner, *Science*, 1984, **226**, 45.
- [104] M. Magini, A.F. Sedda, G. Licheri, G. Paschina, G. Piccaluga, G. Pinna and G. Cocco, *J. Non-Cryst. Solids*, 1984, **65**, 145.
- [105] S. Musić, *J. Mater. Sci. Lett.*, 1989, **8**, 537.
- [106] D. S. Goldman and D. W. Brite, *J. Am. Ceram. Soc.*, 1986, **69**, 411.
- [107] S. Musić, M. Gotić and S. Popović, *J. Mater. Sci. Lett.*, 1989, **8**, 1389.
- [108] S. Musić, S. Popović and M. Gotić, *J. Radioanal. Nucl. Ch.*, 1989, **130**, 299.
- [109] T. T. Vandergraaf and D. R. M. Abry, *Nucl. Technol.*, 1982, **57**, 399.
- [110] S. Musić and M. Ristić, *J. Radioanal. Nucl. Ch.*, 1988, **120**, 289.
- [111] M. Magnin, S. Schuller, D. Caurant, O. Majérus, D. de Ligny and C. Mercier, *Ceram. Trans.*, 2009, **207**, 59.
- [112] A. Quintas, O. Majérus, D. Caurant, J.-L. Dussossoy and P. Vermaut, *J. Am. Ceram. Soc.*, 2007, **90**, 712.
- [113] D. Caurant, A. Quintas, O. Majérus, P. Loiseau, T. Charpentier, P. Vermaut and J.-L. Dussossoy, *Mater. Res. Soc. Symp. Proc.*, 2010, **1265**, 1265-AA06-11.
- [114] O. Majérus, D. Caurant, A. Quintas, J.-L. Dussossoy, I. Bardez and P. Loiseau, *J. Non-Cryst. Solids*, 2011, **357**, 2744.
- [115] T.-M. Chen and J. D. Corbett, *Chem. Mater.*, 1989, **1**, 40.
- [116] T.-M. Chen and J. D. Corbett, *Z. Anorg. Allg. Chem.*, 1987, **553**, 50.